Title
Synthetic Routes to Graphene for Applications in Barrier Materials and Energy Storage

Author
Dubin, Sergey

Publication Date
2014

UNIVERSITY OF CALIFORNIA

Los Angeles

Synthetic Routes to Graphene for Applications in Barrier Materials and Energy Storage

A dissertation submitted in partial satisfaction of the requirements for the degree

Doctor of Philosophy in Chemistry

by

Sergey Dubin

2014

ABSTRACT OF THE DISSERTATION

Synthetic Routes to Graphene for Applications in Barrier Materials and Energy Storage

by

Sergey Dubin

Doctor of Philosophy in Chemistry

University of California, Los Angeles, 2014

Professor Richard B. Kaner, Chair

New techniques for rapid graphite oxide reduction are illustrated. By exposing graphite oxide to a high intensity light, such as a camera flash, rapid deflagration and deoxygenation takes place. The resulting graphitic material is a conductor, with two orders of magnitude higher surface area than its insulating precursor. The technique has potential applications in micro patterning as well as distributed ignition. Flashed graphite oxide is also dispersable in a variety of organic solvents, making it compatible with polymer processing. Another synthetic route to graphene is through solvothermal reduction of graphite oxide. Refluxing dispersions of graphite oxide in N-Methyl-2-pyrrolidone yields charge stabilized colloidal dispersions of graphene. The mechanism of reduction is thermal in nature, while charge stabilization is accomplished through functionalization of graphene NMP moieties and surface energy matching of NMP to graphene sheets.

Conductometric graphene/Pd(0) hydrogen sensors with increased sensitivity compared to pure graphene is demonstrated. Pd(0) nanoparticles on graphene's surface lower the adsorption energy barrier for H_2 molecules and improve the surface chemisorption of H_2.

An inexpensive, solid-state method for producing graphene based electronic materials is presented. Utilizing an inexpensive LightScribe DVD drive to reduce graphene oxide to graphene, patterning any design on a variety of substrates is demonstrated. Highly reduced laser scribed graphene shows promise in applications such as supercapacitors, sensors and electrocatalysts. Metal nanoparticles can be grown directly on the graphene surfaces using metal salt precursors. Light initiated reactions enable formation of nanoparticles within seconds of laser exposure. Such a universal approach to nanoparticle formation is suitable for applications from supercapacitors to catalysis.

An investigation into barrier properties of graphene and graphene oxide films illustrate excellent barrier characteristics of graphene oxide to all gases at STP conditions with rates of permeability being directly related to the kinetic diameter of the gas. Due to the hydrophilic nature of graphene oxide, it is highly susceptible to permeation of water through its layered structure. Barrier properties of graphene to water illustrate at least 60 times lower rates of permeability per unit of thickness.

The dissertation of Sergey Dubin is approved.

Xiangfeng Duan

Yang Yang

Richard B. Kaner, Committee Chair

University of California, Los Angeles

2014

Dedicated to my loving wife Anna Nicole Skay

and our son Jacob Micah Dubin

Table of Contents

1 Introduction

2 Photothermal Deoxygenation of Graphite Oxide for Patterning and Distributed Ignition Applications

3 A One-Step, Solvothermal Reduction Method for Producing Reduced Graphene Oxide Dispersions in Organic Solvents

4 A Conductometric Sensor Based on Graphene with Palladium Nanoparticles

5 Patterning and Electronic Tuning of Laser Scribed Graphene for Flexible All-Carbon Devices

6 Investigation of Barrier Properties of Graphene and Graphene Oxide on PET for Electronic Encapsulation

7 One-Step Synthetic Approach to Graphene Metal/Metal Oxide Nanocomposites for Supercapacitor and Catalysis Applications

List of Figures

Chapter 2: *Photothermal Deoxygenation of Graphite Oxide for Patterning and Distributed Ignition Applications*

Chapter 3: *A One-Step, Solvothermal Reduction Method for Producing Reduced Graphene Oxide Dispersions in Organic Solvent*

Chapter 4: *Conductometric Sensor Based on Graphene with Palladium Nanoparticles*

Chapter 5: *Patterning and Electronic Tuning of Laser Scribed Graphene for Flexible All-Carbon Devices*

Chapter 6: *Investigation of Barrier Properties of Graphene and Graphene Oxide on PET for Electronic Encapsulation*

Chapter 7: *One-step Synthetic Approach to Graphene Metal/Metal Oxide Nanocomposites for Supercapacitors and Catalysis Applications*

List of Tables

Chapter 3: *A One-Step, Solvothermal Reduction Method for Producing Reduced Graphene Oxide Dispersions in Organic Solvent*

Chapter 4: *Conductometric Sensor Based on Graphene with Palladium Nanoparticles*

Chapter 6: *Investigation of Barrier Properties of Graphene and Graphene Oxide on PET for Electronic Encapsulation*

Acknowledgments

Pursuing a goal for many years often brought up many questions, such as where am I headed, how do I achieve it, and are we there yet? Looking back on the career path I have chosen, I know I made the right decision. The idea of graduate school ripened at some point in 2005 during my time as an associate chemist at Cytec Engineered Material in Anaheim, CA. Under the watchful eye of Lisa Viculis, a former Kaner group graduate herself. Working at Cytec, I was often reminded that most of my ideas and solutions in industrial research were fundamental; and questions usually led to more questions, which were begging for answers. Therefore, my first acknowledgement goes to Lisa Viculis, who helped guide me towards graduate studies to pursue academic research. I also would like to thank Jungyeon Hwang, who has supported my decision and helped me get back into the mindset of basic research while I was working with him at Insert Therapeutics, Pasadena, CA.

Professor Richard B. Kaner, my undergraduate and graduate research mentor and advisor, my hat goes off to you. Ric's moral and research support is overwhelming. He has a gift of being extremely helpful when he is needed the most; while at other times, allowing creativity in the lab take its natural unimpeded course, limited only by one's imagination. I wanted to thank Jon Levine for his lab desk, a set of rules to abide by in the lab, and those few, but highly eventful motorcycle rides we have taken together. My special gratitude goes to Scott Gilje, my predecessor and collaborator. Scott has shared his passion for the magical transformations during graphite oxide synthesis with me, which has spurred my research. He was also a major collaborator on a number of papers and projects, two of which are the second and third chapters in this dissertation. Much of the work couldn't have been done without Scott and for that I will be eternally grateful. My appreciation is extended to Chen Zhang who has done a tremendous work in characterization of graphene/Pd material, which led to the 4th chapter in dissertation. I also would like to thank Christina Baker, Henry Tran, Reza Mohammadi and Miao Xie for keeping the mood in the lab always cheerful. Robert Kojima and Yue (Jessica) Wang, for sharing my sense of humor and sarcasm and for spending long hours in dark dungeons of CNSI also known as TEM time. I would also like to thank Sabah Bux and Danny King and the deers of JPL, for the short lived but quite eventful collaborative work at JPL. Chapter 5 of this dissertation was done in collaboration with Veronica Strong and Maher F. El-Kady. It was a pleasure and privilege working along side them. I thank Andrew Lech, Chris Turner, Thomas Farrell, and Brian McVerry for their kind spirits and constructive criticism. My connection to Prof. Yang Yang laboratory and equipment in CNSI couldn't have been possible without help from Matthew J. Allen, Vincent Tung, Jonathan Wassei and Kitty Cha, and for that I'm grateful. I will fondly remember research endeavors with Michael T. Young, Jaime Torres, Lisa Wang, Kris Marsh, William Lemke, Julio D'arcy, Wanmei Sun, James Ma, and Teng Xue. To all my undergraduate research assistants: Shoji Hall, Ha Seong Kim, Kan Wang, Pavlo Kisilchuk, Mathew D. Kowal, Sergio A. V. Jannuzzi, Albert Wong, this work couldn't have been done without you and for that I'm forever in your debt. Above all, I would like to thank my true inspiration - my loving wife, Anna Skay, for her support, understanding and most of all, patience. We started our journey together at the UCLA South campus, where I now complete my graduate studies, with pride and honor... even if it took a little longer than anticipated.

VITA

1999	High School, Diploma, Santa Monica High School, Santa Monica, CA
2001	Transfer Studies, Santa Monica City College, Santa Monica, CA
2004	Bachelor of Science, Chemistry, UCLA, Los Angeles, CA
2004–2006	Associate Chemist, Cytec Engineered Materials, Anaheim, CA
2005	Six Sigma Green Belt Certification, Cytec Engineered Materials, Anaheim, CA
2006–2007	Associate Chemist, Insert Therapeutics, Pasadena, CA
2007–2007	Summer Intern, JPL Thermoelectric Group, Pasadena, CA
2007–2013	Teaching Assistant, Dept. of Chemistry and Biochemistry, UCLA, CA
2009	ACS Poster Award, American Chemical Society Meeting, San Francisco, CA
2007–2013	Research Assistant, Dept. of Chemistry and Biochemistry, UCLA, CA
2013	Masters of Science, Chemistry, UCLA, Los Angeles, CA
2014-current	Senior Research Associate, Dept. of Chemistry and Biochemistry, UCLA, CA

PUBLICATIONS

1. **S. Dubin**, M. D. Kowal, K. L. Marsh, R. B. Kaner, “Molecular transformations of the surface of graphene oxide and its consequences in supercapacitors”, **2014**, (in preparation)
2. **S. Dubin**, L. Wang, W. Lemke, M. D. Kowal, W. Sun, R. B. Kaner, “One-step synthetic approach to graphene metal/metal oxide nanocomposites for supercapacitors and catalysis applications”, **2014**, (in preparation)
3. L. Wang, **S. Dubin**, M. F. El-Kady, J. Hwang, K. L. Marsh, M. Mousavi, R. B. Kaner, “Graphene supercapacitor in a flash”, 2014, (in preparation)

4. T. Xue, B. Peng, M. Xue, X. Zhong, C. Chiu, S. Yang, Y. Qu, L. Ruan, S. Jiang, **S. Dubin**, R. B. Kaner, J. I. Zink, M. E. Meyerhoff, X. Duan, Y. Huang. “Integration of molecular and enzymatic catalysts on graphene for biomimetic generation of antithrombotic species.” *Nature Comm.,* **2014**, *5*, 3200
5. T. Xue, S. Jiang, Y. Qu, Q. Su, R. Cheng, **S. Dubin**, C. Chiu, R. B. Kaner, Y. Huang, X. Duan. “Graphene-Supported Hemin as a Highly Active Biomimetic Oxidation Catalyst.” *Angewandte Chemie,* **2012,** *51* (16), 3822 – 3825
6. M. F. El-Kady, V. Strong, **S. Dubin**, R. B. Kaner. “Laser Scribing of High-Performance and Flexible Graphene-Based Electrochemical Capacitors” *Science,* **2012**, *335*, 1326 – 1330
7. V. Strong, **S. Dubin**, M. F. El-Kady, A. Lech, Y. Wang, B. H. Weiller, R. B. Kaner. “Patterning and electronic tuning of laser scribed graphene for flexible all-carbon devices.” *ACS Nano*, **2012**, *6* (2), 1395 – 1403
8. M. Shafiei, P. G. Spizzirri, R. Arsat, J. Yu, J. du Plessis, **S. Dubin**, R. B. Kaner, K. Kalantar-zadeh, W. Wlodarski. “Platinum/graphene nanosheet/SiC contacts and their application for hydrogen gas sensing.” *J. Phys. Chem. C*, **2010**, *114 (*32), 13796 – 13801
9. **S. Dubin**, S. Gilje, K. Wang, V. C. Tung, K. Cha, A. S. Hall, J. Farrar, R. Varshneya, Y. Yang, R. B Kaner. “A one-step, solvothermal, reduction method for producing reduced graphene oxide dispersion in organic solvents.” *ACS Nano*, **2010**, *4* (7), 3845 – 3852
10. S. Gilje, **S. Dubin**, A. Badakhshan, J. Farrar, S. A. Danczyk, R. B. Kaner. “Photothermal Deoxygenation of Graphene Oxide for Patterning and Distributed Ignition Applications.” *Adv. Mat*, **2009**, *22* (3), 419 – 423

Chapter 1

Introduction to Graphene and Graphene Oxide

1.1 Thesis Overview

Graphene was first mentioned in the works of Phillip Wallace, who studied it as a limiting case for theoretical work on graphite[1]. However, it wasn't until 2004 when Geim and Novoselov first isolated a single layer of graphene that the real story of graphene began[2]. Graphene is a one atom thick layer of sp^2 hybridized carbon atoms, forming an infinite sheet. It has a high thermal conductivity (~5000 $W\ m^{-1}\ K^{-1}$), Young's modulus of ~1 TPa, breaking strength of 42 $N\ m^{-1}$, high conductivity at room temperature ($10^6\ S\ cm^{-1}$) it also exhibits field effect behavior, and high frequency operation.[3-7] Such characteristics, along with nanometer sized device possibility are placing graphene as the top candidate for the future of electronics and composite materials alike. Although the expectations for graphene are high, before graphene can be used in commercial applications it must be scaled up in a commercially feasible way.

Graphite oxide (GO) has first been isolated in 1859 by Brodie et al; since then, every 50 years a new synthetic approach to graphite oxide has been published[8-11]. Graphite oxide is a thermodynamically unstable, non-stoichiometric, water dispersable, product of oxidation of graphite. The molecular formula of graphite oxide varies with synthetic procedures, and purifications techniques used, but using the modified Hummers method the molecular formula of GO has been determined to be: $C_8O_{2.25}(OH)_{1.95}(OK)_{0.15}$[11] The general model of graphite oxide follows one proposed by Lerf and Klinowski, which suggests isolated domains of sp^2 carbon surrounded by sp^3 carbon bound to hydroxyl and epoxide group in the basal plane of graphite and carboxylic groups on the peripheral on the sheets.[12] Oxygen moieties on graphite oxide allow it to maintain stable water dispersion through charge stabilization. Since GO is thermodynamically unstable, temperature increase in graphite oxide past 200 °C will lead to deflagration, deoxygenation and partial reduction leading to reduced graphene oxide, with higher temperature producing graphene. It has been reported in the literature that when nanomaterials are exposed to a high intensity light, such as a camera flash, they undergo combustion (CNTs) or oxidation (Si nanowires)[13-14]. Both freeze-dried and cast films of GO react to camera flash by deflagration and deoxygenation, resulting in graphene like foam.[15] Furthermore, graphite oxide can be dispersed in ethanol fuel and when used in homogenous charge compression ignition (HCCI) can be used to provide accurate ignition timing. The details and results of these experiments are reported in Chapter 2.

One application where graphene high aspect ratio may be extremely advantageous is in polymer nano composites. Polymer composites that utilize inorganic nano materials as fillers have recently gained attention due to unique properties they provide. Increased fracture toughness, decreased fatigue, increased glass transition point, are just a few metrics that are enhanced and are of particular interest in numerous applications, such as aerospace, high performance automotive and sports industries.[16] Up to recently, the bulk of nanocomposite polymer research has been focused on clay silicates, such as montmorillonite.[17] However, the electrical and thermal conductivity of clay minerals are quite poor.[18] Which limits their use in such applications as lightning strike protection. The solution can be found in fillers that provide high conductivity through conjugated network, without sacrificing strength and structure of silicates. The research has turned to carbon-based nanofillers, such as carbon black, expanded graphite and carbon nanotubes (CNTs)[19-21] Among these, CNTs have proven to be by far, the most effective as conductive fillers owing to the excellent conductivity as well as ability to functionalize the walls of the CNTs with excellent integration into the polymer matrix.[22-23] However, high production cost of CNTs impeded their full integration in mass production of CNT polymer nanocomposites. Graphene, synthesized through reduction of graphite oxide offers an excellent alternative to CNTs. By using a high boiling point solvent like N-Methyl-2-pyrrolidone (NMP) to reduce GO sheet, while keeping graphene sheet from agglomeration through surface energy matching with a solvent, a stable dispersion of graphene sheets in polar organic solvent can be achieved.[24] Chapter 3 of this dissertation presents a detailed approach for synthethis of NMP reduced graphite oxide, using a solvothermal approach. Integration of graphene nanoplatelets into a variety of organic solvents that are compatible with commercial polymer and resin processing is also discussed.

Graphene has been used in the development of chemical, mass, and bio-sensors, with demonstrated sensitivity to gas species including: nitrogen dioxide, nitrogen monoxide, ammonia, hydrogen, carbon dioxide, carbon monoxide, nitrogen and oxygen.[25] However, routes that can enhance graphene reactivity are still needed to achieve higher sensing performance and the commercialization of such devices. Hydrogen sensitivity on graphene surface can be enhanced through introduction of curvature in the sheet of graphene, such as deposition of metal nanoparticles, which themselves enhance the reactivity[26]. Chapter 4 of this dissertation shows a graphene/Pd sensor that has surface enhanced Raman effect with an enhancement ratio of approximately 5, due to the presence of Pd nanoparticles. The sensing response indicates that the graphene/Pd sensor has a higher sensitivity compared to the pure graphene sensor.

Although scientific literature is filled with a variety of ways to produce device quality graphene, most start with graphite oxide as a commercially scalable alternative to chemical vapor deposition (CVD). Unfortunately, the oxygen containing functional group on the surface of graphite oxide serve as defects in its electronic structure and hinder it insulating. Therefore removal of the oxygen moieties and restoration of the conjugation network must be accomplished before reduced graphene oxide can be used in an electronic device. Our previous research has shown that graphite oxide is highly susceptible to high intensity light, such as one found in a camera flash. However, the process is highly energetic and difficult to control. Alternative solution is to use laser, such as one found inside a CD/DVD. Chapter 5 discusses our findings where a film of graphite oxide drop cast onto the surface of a LightScribe DVD disc is reduced to laser scribed graphene (LSG).[27] In addition to the complete reduction, we show that partial reduction is possible through control of laser's focus/defocus mechanism by providing the disc drive with a different computer image to raster on a CD. Furthermore, we show that the process can be repeated on flexible substrates, such as poly ethylene terephthalate (PET) and subsequent publication on the use of LSG in all carbon capacitors shows excellent results.[28]

Large aspect ratio materials like graphene can be used not only for polymer composite reinforcement, but also as a barrier material. Owing to a small C-C bond distance in a benzene ring, even a gas molecule of He (kinetic diameter of 2.6 Å) would be hard pressed to squeeze through an ideal graphene sheet. Additionally, graphene is extremely thin, only 3.34 Å and 97.7% transparent to visible light. Using several layers of graphene it would be possible to account for any defects in the graphene sheet by creating a tortious path for the gas to travel. In Chapter 6 we investigate films of both the graphene oxide and graphene to helium and water permeation using a custom-built permeability setup.

The final chapter of the dissertation investigates laser scribed graphene cascade reactions, where a precursor graphite oxide is mixed with a precursor to a metal or metal oxide nanoparticle, such as silver acetate. We show that in the process of reduction of GO and formation of LSG, the exothermic energy is used to thermally reduce silver, palladium and nickel acetates to Ag(0), Pd(0) and NiO. Preliminary experiments are also conducted on application the resulting nanocomposites. We evaluate LSG/Pd(0) as a Suzuki-Miyaura coupling reaction catalyst, and LSG/NiO in a supercapacitor application.

1.2 References

1. Wallace, P. R.; The Band Theory of Graphite *Phys. Rev.* **1947**, *71*, 622 – 634
2. Novoselov, K. S.; Geim, A. K.; Morozov, S. V.; Jiang, D.; Zhang, Y.; Dubonos, S. V.; Grigorieva, I. V.; Firsov, A. A. *Science*, **2004**, *306*, 666 – 669
3. Lee, C.; Wei, X. D.; Kysar, J. W.; Hone, J. *Science*, **2008**, *321*, 385 – 388
4. Balandin, A. A.; Ghosh, S.; Bao, W.; Calizo, I.; Teweldebrhan, D.; Miao, F.; Lau, C. N.; *Nano Lett.* **2008**, *8*, 902 – 907
5. Zhu, Y.; Murali, S.; Cai, W.; Li, X.; Suk, J. W.; Potts, J. R.; Ruoff, R. S. *Adv. Mater.* **2010**, 22, 3906 – 3924
6. Du, X.; I. Skachko; Barker, A.; Andrei, E. Y. *Nature Nanotech.* **2008**, *3*, 491 – 495
7. Huang, X.; Yin, Z. Y.; Wu, S. X.; Qi, X. Y.; He, Q. Y.; Zhang, Q. C.; Yan, Q. Y.; Boey, F.; Zhang, H. *Small*, **2011**, *7*, 1876 – 1902
8. Brodie; B. C. *Philos. Trans. R. Soc. London* **1859**, *149*, 249 – 259
9. Hummers, W. S.; Offeman, R. E. *J. Am. Chem. Soc.* **1958**, *80*, 1339 – 1339
10. Staudenmaier, L. *Berichte der Deutschen Chemischen Gesellschaft*, **1898**, *31*, 1481 – 1487
11. Kovtyukhova, N. I.; Ollivier, P. J.; Martin, B. R.; Mallouk, T. E.; Chizhik, S. A.; Buzaneva, E. V.; Gorchinskiy, A. D. *Chem. Mater.* **1999**, *11*, 771 – 778
12. Lerf, A.; He, H.; Forster, M.; Klinowski, J. *J. Phys. Chem. B* **1998**, *102*, 4477 – 4482
13. Chen, H. X.; Diebold, G. J.; *Science*, **1995**, *270*, 963 – 966
14. Wang, N.; Yao, B. D.; Chan, Y. F.; Zhang, X. Y., *Nano Lett.* **2003**, *3*, 475 – 477
15. Gilje, S.; Dubin, S.; Badakhshan, A.; Farrar, J.; Danczyk, S. A.; Kaner, R. B. *Adv. Mater.*

2010, *22* (3), 419 – 423

16. Hussain, F.; Hojjati, M.; Okamoto, M.; Gorga, R. E. *Journal of Composite Materials*, **2006**, *40* (17), 1511 – 1575
17. Gao, F. *Materials Today*, **2004**, *7* (11), 50 – 55
18. Bao, Y. Z.; Cong L. F.; Huang, Z. M.; Weng, Z. X. *J Mater. Sci.* **2008**, *43*, 390 – 394
19. Li, Q.; Park, O. K.; Lee, J. H. *Adv. Mater. Res.* **2009**, *79*, 2267 – 2270
20. Yu, A.; Ramesh, P.; Itkis, M. E.; Elena, B.; Haddon, R. C.; *J Phys. Chem. C*, **2007**, *111*, 7565 – 7569
21. Kim, S. K.; Kim, N. H.; J. H. Lee *Scripta Mater.* **2006**, *55*, 1119 – 1122
22. Jeevananda, T.; Jang, Y. K.; Lee, J. H.; Siddaramaiah; M. V.; Urs, D.; Ranganathaiah, C. *Polym. Int*, **2009**, *58*, 755 – 780
23. Hong, C. E.; Prashantha, K.; Advani, S. G.; Lee, J. H. *Compos. Sci. Technol.* **2007**, *67*, 1027 – 1034
24. Dubin, S.; Gilje, S.; Wang, K.; Tung, V. C.; Cha, K.; Hall, A. S.; Farrar, J.; Varshneya, R.; Yang, Y.; Kaner, R. B. *ACS Nano*, **2010**, *4* (7), 3845 – 3852
25. Yuan, W.; Shi, G.; *J. Mater. Chem. A*, **2013**, *1*, 10078 – 10091
26. Sadek, A.; Zhang, C.; Hu, Z.; Partridge, J.; McCulloch, D.; Wlodarski, W.; Kalantar-Zadeh, K. *J. Phys. Chem. C, **2010**, 114* (1)*, 238 – 242*
27. Strong, V.; Dubin, S.; El-Kady, M. F.; Lech, A.; Wang, Y.; Weiller, B. H.; Kaner, R. B. *ACS Nano*, **2012**, *6* (2), 1395 – 1403
28. El-Kady, M. F.; Strong, V.; Dubin, S.; Kaner, R. B. *Science*, **2012**, *335* (6074), 1326 – 1330

Chapter 2

Photothermal Deoxygenation of Graphene Oxide for Patterning and Distributed Ignition Applications

2.1 Introduction

A xenon discharge tube, such as is used to produce a photographic flash has been reported to cause the ignition of carbon nanotubes, silicon nanowires and welding of nanofibers of the conducting polymer polyaniline.[1-3] In these reactions, the high surface to volume ratio of the nanomaterials being irradiated, coupled with the inability of the small structures to efficiently dissipate the absorbed energy, leads to a rapid increase in temperature and subsequent ignition or welding of the materials. Although heating materials through the use of light energy is not a new phenomenon, achieving such a rapid and dramatic temperature change using only millisecond pulses of light demonstrates a tangible and technologically significant capability that is unique to nanoscale materials.[4]

Graphene oxide (GO) is a deeply colored, water dispersible, oxidized form of graphene obtained through the treatment of graphite powder with powerful oxidizing agents.[5] Although GO has been known for over 150 years, only recently have scientists had access to the tools necessary to properly analyze its atomically thin sheet structure. This has rekindled interest in graphite oxide and has led to a number of recent discoveries, including: the stacking of GO platelets to form paper-like materials of high modulus and strength.[6,7] Many studies have suggested that GO can be reduced to graphene-like carbon sheets by applying chemical reducing agents or by using thermal treatments.[8-10] This has led to speculation that GO could find use as a precursor in a bulk route to dispersible graphene sheets.[11-13] Already, several groups have succeeded in creating conducting polymer composites, transparent conducting films and simple electronic devices based on reduced GO.[14-26] In addition to the chemical reduction of GO, Aksay, et al. have reported the thermal deoxygenation of GO to create functionalized graphene sheets upon rapid heating to 1100 °C under an inert atmosphere. [27, 28] These organic solvent dispersible sheets have enabled the direct creation of polymer composites, without the need for surfactants.[29] Thermal deoxygenation of GO to form graphitic carbon dates back to the 1960's when Boehm and Scholz first reported on the ignition and deflagration of graphite oxides prepared by different methods.[30] Upon rapid heating to temperatures of ~200 °C, GO decomposes to the most thermodynamically stable oxide of carbon, $CO_{2.}$ Along with the exothermic release of CO_2, H_2O and CO also form as minor products.[31]

Due to the dramatic temperature increase (in excess of 1500 °C) that can be achieved using millisecond pulses of light, carbon nanotubes have been considered as additives to rocket fuels to attain distributed fuel ignition. If different parts of the fuel can be ignited simultaneously, better control and stability along with lowered weight should be achievable.[32-34] Attempts aimed at using CNTs for ignition applications, however, have failed, since the CNT combustion requires outside oxygen. In fact, the CNTs themselves – like C_{60} and carbon soot - play little role in the ignition process, instead it is the iron nanoparticle catalyst used to grow them, along with oxygen, that supports combustion.[35-37] Even with sufficient catalyst, uniformly dispersing CNTs into liquid fuels remains problematic. Here we report the discovery of the photothermally initiated deflagration of GO that can take place even in an oxygen deficient environment. Since GO readily disperses in alcohols and other polar organic solvents, preliminary results indicate that with some chemical modification GO could be dispersed in fuels as well. This along with the current interest in GO as a nanoscale platelet material gave us the impetus to investigate this photothermally driven process further.

2.2 Experimental

2.2.1 Synthesis

Graphene oxide was synthesized using a modified Hummer's method as reported previously in Ref. [14]. Dispersions of GO were freeze-dried using an FTS systems Dura-Stop μP Freeze-drying system. Dispersion concentrations of 30 mg/ml, 15 mg/ml, 7.5 mg/ml and 3.25 mg/ml were freeze-dried resulting in porous GO materials with densities of 30 mg/cm^3, 15 mg/cm^3 and 7.5 mg/cm^3 and 3.25 mg/cm^3, respectively. Figure 2.3 is an SEM image of the lowest density 3.25 mg/cm^3 sample showing the network of thin platelets. Film samples of GO were obtained by filtration of a GO dispersion through a 0.22 μm Anapore™ filter for free-standing films, and a 0.2 μm Nylon Millipore™ filter for thin films that remained bound to the filter membrane for stability.

2.2.2 Characterization

X-ray diffraction (XRD) was carried out using a PANalytical XPert Pro diffractometer with Cu Kα radiation (λ = 1.5418 Å). Before taking X-ray scans the GO was dried for 48 h under vacuum at room temperature followed by 24 h under vacuum over P_2O_5 which acts as a drying agent. Powder X-ray diffraction can be used to verify that the oxidation reaction has reached completion since the introduction of oxygen moieties expands the interplanar galleries in graphite from 3.34 Å to ~6.9 Å. Our graphite oxide exhibits a characteristic peak at 12.75 degrees 2θ corresponding to the 002 interplanar spacing of 6.94 Å, while the most intense peak from the starting graphite at 26.4 degrees 2θ, corresponding to a d-spacing of 3.34 Å, is completely absent. The d-spacing of slightly >6.9 Å for the synthesized GO indicates that despite drying under vacuum for 24 h, some water has been absorbed by the GO.

The GO and reduced GO samples were inserted into the analysis chamber of a ThermoVG ESCALAB 250, X-ray photoelectron spectrometer. Spectra were obtained by irradiating the sample with a 320 μm diameter spot of monochromated aluminum Kα X-rays at 1486.6 electron Volts (eV) under ultrahigh vacuum conditions. The analysis consisted of acquiring 10-20 scans and signal averaging. The survey scans were acquired with a pass energy of 80 eV, and the high resolution scans were acquired with a pass energy of 20 eV. Low pressure gas adsorption isotherms were measured volumetrically on an Autosorb-1 analyzer (Quantachrome Instruments). Conductivity data were obtained using a Jandel RM3-AR resistivity tester using an applied current of 4.532 μA in combination with a 4-point probe head. Optical microscope images were taken using a Zeiss AxioTech 100 reflected light microscope with Zeiss AxioCam MRc camera.

A liquid nitrogen bath (77 K) was used for N_2 and H_2 isotherm measurements. The N_2, H_2, and He gases used were UHP grade. For measurement of the apparent surface areas (SLang), the Langmuir method was applied using the adsorption branches of the N_2 isotherms assuming a N_2 cross-sectional area of 16.2 $Å^2$/molecule. The micropore volumes (Vp) were determined using the Dubinin-Raduskavich (DR) transformed N_2 isotherms across the linear region of the low-pressure data.

2.3 Results and Discussions

A random porous network of GO platelets is created by freeze-drying GO dispersions. The porous structure results from the extraction of water without causing collapse of the solid matrix of GO platelets due to capillary action, as would happen with conventional evaporation. Creating dry, low-density networks of nanoscale GO platelets serves two purposes: first, the surface to volume ratio of the platelets is increased providing maximum surface area for energy absorption; second, thermally conductive pathways through which absorbed energy can diffuse are reduced. The GO dispersions were comprised of platelets ranging in size from 100 nm – 5 μm in diameter with the majority of platelets around 500 nm in diameter as analyzed by atomic force microscopy. The GO foam networks enable greater energy absorption and confinement leading to dramatic temperature increases on exposure to a camera flash. Using freeze-drying, porous GO foams can be made to densities down to 5 mg/cm^3 before the structure collapses under its own weight. Most of the GO foams used in this study had a density of 15 mg/cm^3. Figure 2.1a is a photograph of a light-brown GO foam sample prepared by freeze drying a 15 mg/ml dispersion to achieve a density of 15 mg/cm^3. Figure 2.1b shows an SEM micrograph of the same sample magnified 1000x. In the SEM image, the GO platelets appear as crumpled sheets ranging in diameter from 500 nm to 20 μm, that assemble to form a porous 3-dimensional network. The mechanical integrity of the GO foams increase with increasing density. Foams with a density of < 5 mg/cm^3 typically collapsed easily and were difficult to handle. Foams with a density ranging from 10 mg/cm^3 to 20 mg/cm^3 were robust but required careful handling, while denser foams were quite sturdy much like a commercial silica aerogel. After flashing, the foams lose their structural robustness, fall apart and are easily blown around by gusts of air.

Upon exposure to a photographic flash, the GO foam emits a popping sound most likely attributable to a photoacoustic effect similar to the flashing of CNTs.[38] A color change from light brown to dark black can be seen immediately after exposure to the flash indicating conversion to deoxygenated graphitic carbon. A photograph of the flashed GO foam is shown in Figure 2.1c**.** The light brown spots around the periphery of the sample correspond to the unreacted regions at the edges of the sample as a result of cooling and expansion of the foam as the reaction front propagates. Figure 2.1d, shows an expanded structure much like that of exfoliated graphite and comparable to recent reports on thermally reduced GO.[27, 28] The inset picture of Figure 2.1d shows the flashed GO foam at 100,000x magnification. At this magnification, the expanded nature of the flash deoxygenated graphitic platelets can be observed. Using the scale bar as a gauge, the thickness of the thinnest expanded sheets can be seen to range from 10-20 nm.

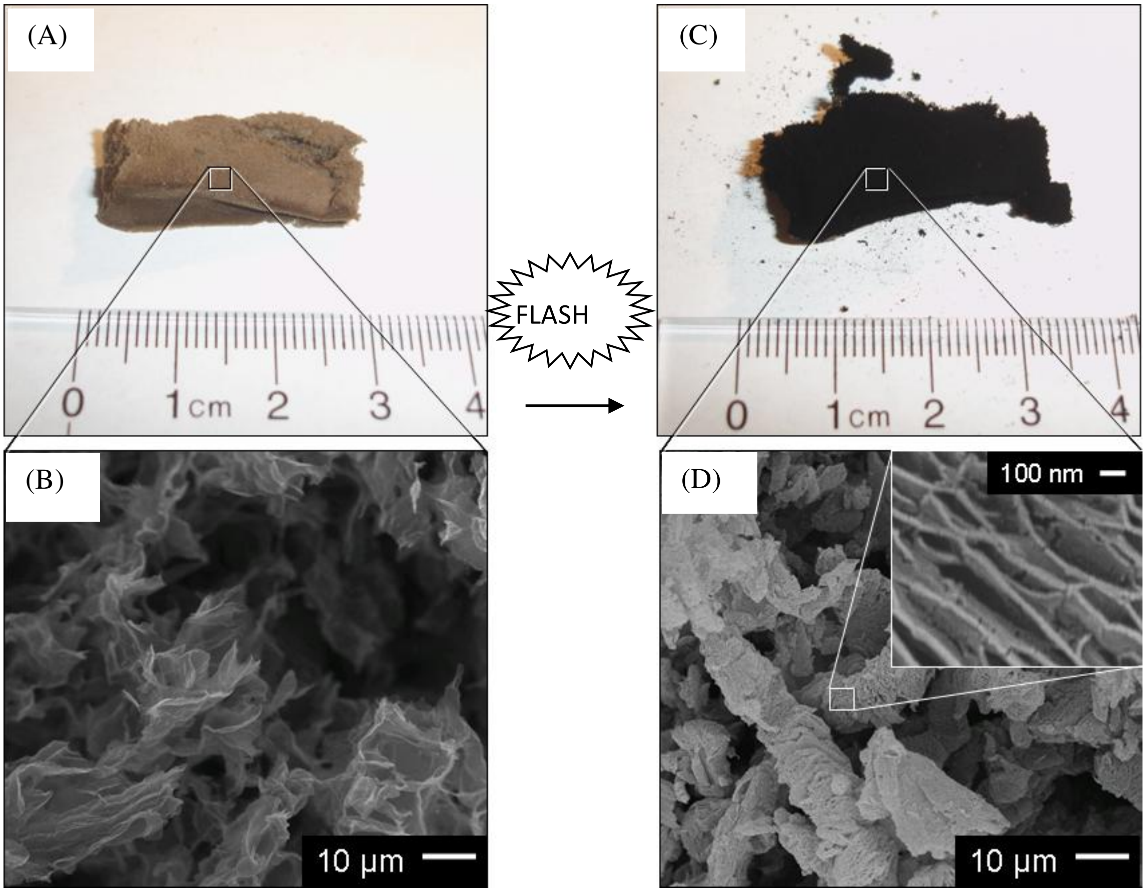

Figure 2.1 (a) An image of a GO foam sample before exposure to a photographic flash. (b) A scanning electron micrograph (SEM) shows the porous nature of the GO foam. (c) After flashing, the GO foam ignites releasing CO_2 and H_2O and leaving behind an exfoliated, deoxygenated graphitic carbon. (d) An SEM image of the material shows exfoliated layers. (inset) Under high magnification, the layers measure 10-20 nm in thickness.

2.3.1 Graphene Oxide Foam Deflagration

Upon exposure of the GO foam samples to a flash of light, the ease of ignition and reaction propagation was found to be heavily dependant on the density of the GO foam. Denser GO foams (>30 mg/cm^3) were typically more difficult to ignite requiring several flashes at close range (<1 mm) in order to initiate a reaction. Once ignited, however, a reaction front propagates through the GO foam structure releasing CO_2 and H_2O as a result of the deflagration. Medium density GO foams (25 - 10 mg/cm^3) readily ignited and were dense enough to allow for the propagation of the deflagration reaction. Figure 2.2a is a photograph of a 15 mg/cm^3 GO foam sample undergoing a progressive deflagration reaction to deoxygenated carbon. The light brown area on the right side of the sample is unreacted GO. By analyzing a series of photographs taken at 0.1 second intervals after ignition of the GO foam, the reaction front velocity through the material was determined to be ~10 cm/sec.

GO foams could be flashed under an inert atmosphere, such as argon, or through the glass walls of an evacuated flask. In both cases the GO foams ignited and the reaction propagated through the bulk of the foam, demonstrating that the deflagration of GO does not require outside oxygen to propagate. Figure 2.2b shows SEM images of GO foams flashed in an open atmosphere and under argon (Figure 2.2c). Unlike the samples flashed under argon, SEM images of the open air flashed samples look as though they contain amorphous carbon at the edges instead of the fine expanded structure found in the argon flashed samples. We attribute this amorphous carbon to secondary burning of the newly formed graphitic carbon in atmospheric oxygen after the removal of H_2O and CO_2 from the primary deflagration reaction. Lower density GO foams (<5 mg/cm^3), ignited easily but did not produce enough heat via deflagration to sustain a reaction front, and thus were not self-propagating. An SEM image of a low density foam (3.25 mg/cm^3), is shown in Figure 2.3.

2.3.2 Flash Characterization

The films were flashed using a Pro Master FA1000 being fired in “test” mode. The pulse duration of the camera flash was on the order of milliseconds. The integrated pulse energy and duration of the flash was measured using a Molectron Opti-mum4001, 4-channel joulemeter in combination with a model J25 detector. UV-vis spectra were acquired on a Shimadzu UV-3101PC, software used is Shimadzu UVProbe version 2.21. The absorbance wavelength spectrum was scanned from 190 nm through 800 nm. The UV-vis spectrum of GO reveals a broad peak in absorbance with a maximum centered around 230 nm trailing off at higher wavelengths. Since most commercially available camera flashes utilize a UV filter to more accurately simulate the color temperature of sunlight, we found that removal of the polycarbonate UV filter allowed us to flash the GO foam samples from further away or through thick glass. When flashing GO samples through glass, the glass tends to act as a thermal barrier sheilding the samples from the heat developed by the Xe discharge tube. Since only the light from the flash is allowed through, we believe the photo-ignition of GO to occur strictly as a result of absorbed light energy being converted into heat by the GO, with no real contribution from the heat of the Xe flash tube. The flash energy typically increased as the charging capacitor in the photographic flash unit was allowed to charge for longer periods of time.

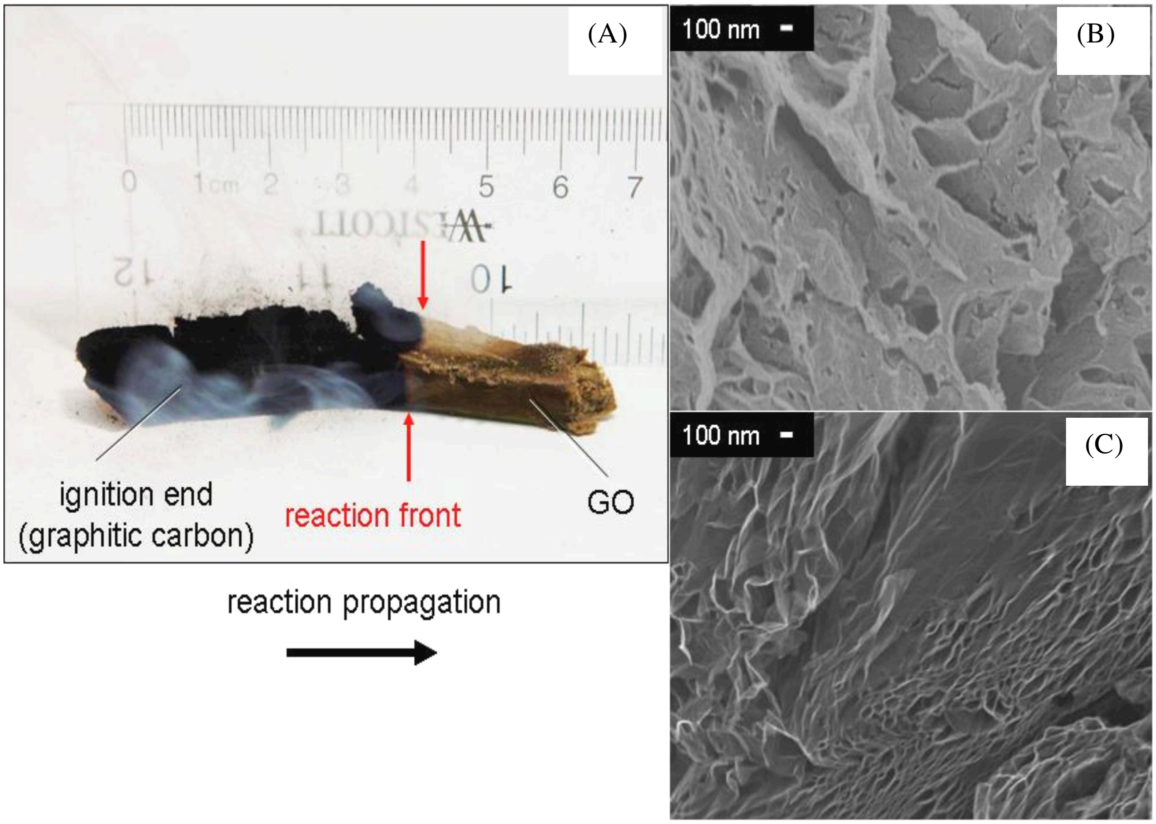

Figure 2.2 (a) A picture of a 15 mg/ml GO foam sample after photoignition shows the propagation of the reaction front from left to right. (b) GO foams flashed in air pyrolyze using oxygen from the air to yield amorphous carbon at the edges as shown in the SEM image. (c) GO foams flashed under argon have no access to atmospheric oxygen resulting in pure exfoliated sample.

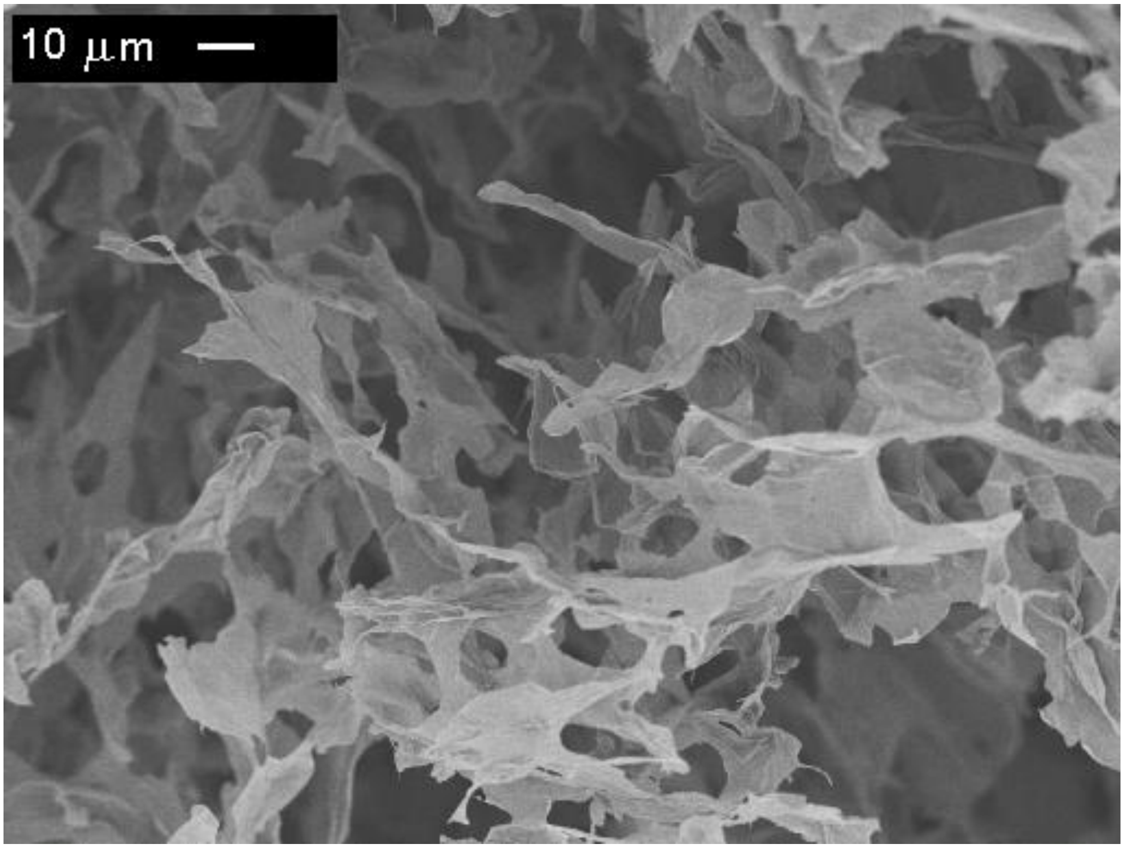

Figure 2.3 An SEM image of a low density (3.25 mg/cm^3) GO foam sample shows the loose network of thin GO platelets making up the structure.

By firing the flash immediately after the "test flash" button illuminated, greater repeatability could be achieved. Five measurements were taken at each distance with a standard deviation of less than 4%. Typical flash durations ranged from 1-2 milliseconds. Figure 2.4 shows a plot of the total integrated fluence (J/cm^2) released by the flash as a function of distance from the flash. The two lines in Figure 2.4 correspond to the flash energy with and without the UV filter in place. The maximum ignition distance for a 15 mg/ml GO foam with and without the UV filter in place was measured and is indicated in Figure 2.4. We found that although the total energy increased only slightly at each distance by removing the UV filter, ignition of the GO foam could be achieved at further distances – and therefore lower total energy – than when the UV filter was in place. The GO foams typically ignited at a distance of ~1 mm with the UV filter in place corresponding to a fluence of 250-300 mJ/cm^2. After removing the UV filter, the same GO foam could be ignited at a distance of 13-15 mm corresponding to < 200 mJ/cm^2. We speculate that since GO absorbs more heavily in the UV, more energy was being absorbed and therefore converted into heat after removal of the UV filter allowing ignition at lower total energy levels. Allowing the camera flash to charge for an extended period resulted in a higher energy flash with typical fluence values of ~400 mJ/cm^2.

2.3.3 Characterization of the Resulting Graphitic Carbon

X-ray powder diffraction of a compressed pellet of the reduced graphite oxide shows a broad, low-intensity peak centered at 26.4° 2θ indicating that after deflagration the product is, in fact, graphitic in nature.[30]

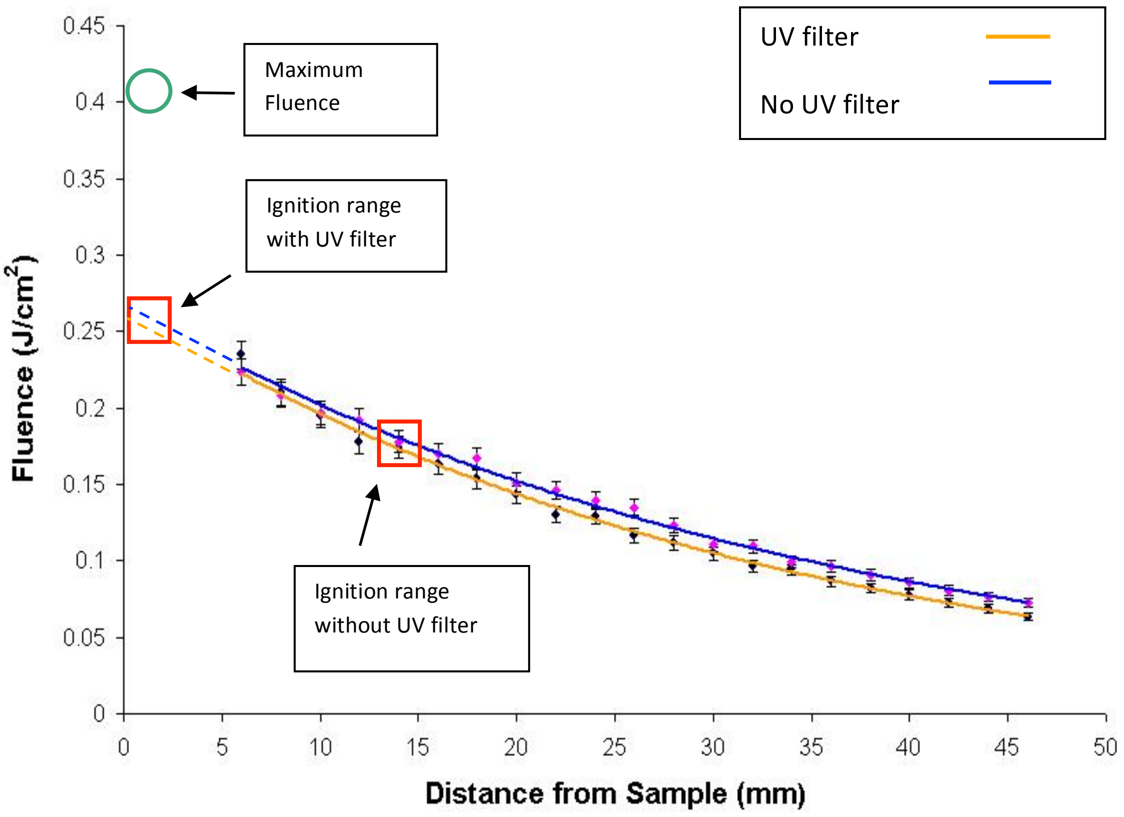

Figure 2.4 Using a pulse energy meter the total integrated energy of the camera flash was plotted as a function of distance from the flash with and without the UV filter built into the flash. The energy was normalized per unit area to give the fluence (J/cm^2) of the flash at a given distance. Even though the total energy of the flash increased only marginally without the UV filter as opposed to the flash with the filter, the energy required to ignite the GO foam was considerable less without the UV filter. Since GO absorbs more heavily in the UV (ε_{max} = 231 nm) it is not surprising that by removing the UV filter from the flash, ignition of GO at lower energies can be achieved.

The broadness of the diffraction peak is most likely due to both the small crystalline domain sizes of the graphitic planes and the turbostratic nature of the expanded sheets. The deoxygenated carbon material that remains after photothermally induced deoxygenation was analyzed for its carbon and oxygen content using X-ray photoelectron spectroscopy (XPS). The carbon content increases from 68.7% in the GO starting material, to 92.1%, while the oxygen content decreases from 29.3% to 7.7%. The remaining oxygen is most likely contained in residual functionalities (-COOH, -OH, etc.) due to incomplete deoxygenation. Figure 2.5a and 2.5b show XPS spectra of GO before and after flashing, respectively. Upon flashing, the GO foam undergoes an average mass loss of 70%, attributable to the formation of gaseous CO_2.

As an interesting side note, repeated flashing of the expanded deoxygenated carbon material results in continued photoacoustic popping sounds and a measurable reduction in mass for each flash exposure. We speculate that the added energy from repeated flashing causes the mostly reduced graphite oxide material to continue oxidizing to CO_2. The deoxygenated carbon obtained from flashing GO was found to be dispersible in several aprotic polar organic solvents including: tetrahydrofuran (THF), dimethylformamide (DMF), n-methylpyrrolidone (NMP), and dimethylsulfoxide (DMSO) as is shown in Figure 2.5c. Resistivity measurements taken on the deoxygenated carbon resulted in a resistivity decrease from 9.98×10^4 Ω·cm before flashing to 2.23 Ω·cm after photoinduced deoxygenation. The change in resistivity of over four orders of magnitude is consistent with other forms of reduced GO obtained by thermal means.[27, 28]

Due to the expanded nature of the flashed GO foams; they were analyzed for surface area by measuring N_2 gas uptake using the Braunaur Emmett-Teller (BET) analysis method. Before flashing, a GO foam with a density 15 mg/cm^3 was measured to have a surface area of 6 m^2/g.

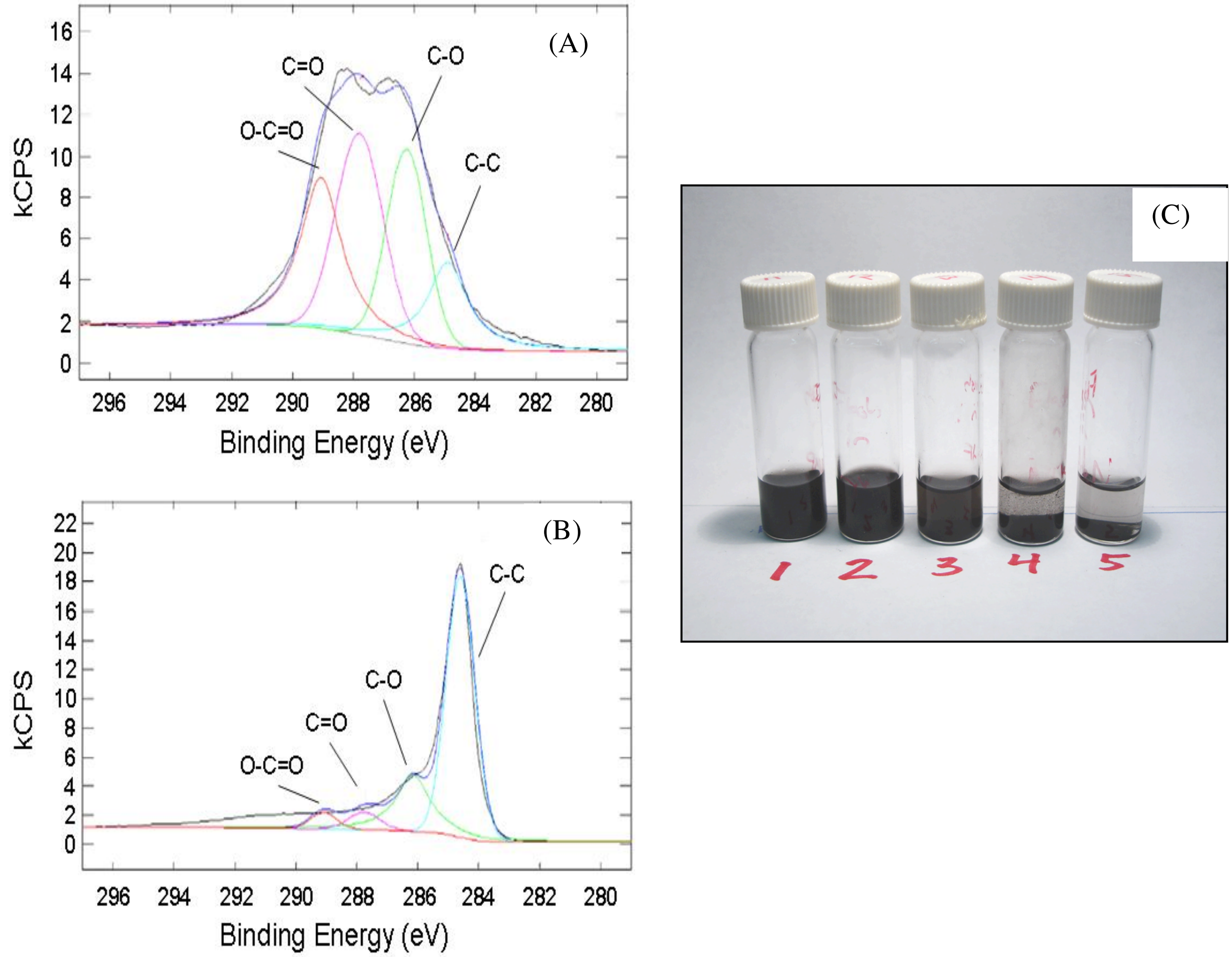

Figure 2.5 (a) X-ray photoelectron spectroscopy (XPS) peak deconvolution of GO yields a C:O ratio of 2.3:1. (b) After flashing the C:O ratio increases to 11.9:1 indicating substantial deoxygenation. The residual functionalities left behind enable the deoxygenated carbon sheets to be dispersed into a variety of polar aprotic organic solvents including: (1) n-methylpyrolidone (NMP), (2) dimethylformamide (DMF), (3) tetrahydrofuran (THF), (4) nitromethane, and (5) acetonitrile as shown in the photograph.

After flashing, the measured surface area yielded a range from 400 to 980 m^2/g. We believe the large range in values can be attributed to difficulties in determining the sample weight and adsorbed water content. Exposure of the flashed, deoxygenated carbon to hydrogen was performed, resulting in an uptake of 0.5 wt % at 77 K.

2.3.4 Flash Patterning

In addition to GO foam materials, it is possible to make GO films which can be photothermally patterned. To accomplish this, thin GO films (< 1 μm in thickness) were created by filtering a dilute GO dispersion through a 0.2 μm Nylon Millipore™ filter. Figure 2.6a shows optical microscope images of a copper transmission electron microscope (TEM) grid placed on top of a GO film while still attached to the Nylon filter. Using the TEM grid as a mask, the GO film was exposed to a flash at close range inducing deoxygenation to graphitic carbon. Figure 2.6b is an optical microscope image of the GO film after flashing. Looking at the image, defined regions of black (exposed) and brown (masked) can clearly be seen mimicking the TEM grid mask. SEM images of the masked film (Figure 2.6c) show how the exposed regions on the GO film expand outward upon ignition by the flash. The release of CO_2 and H_2O during deflagration is likely the cause of the platelets pushing out from the surface of the film.

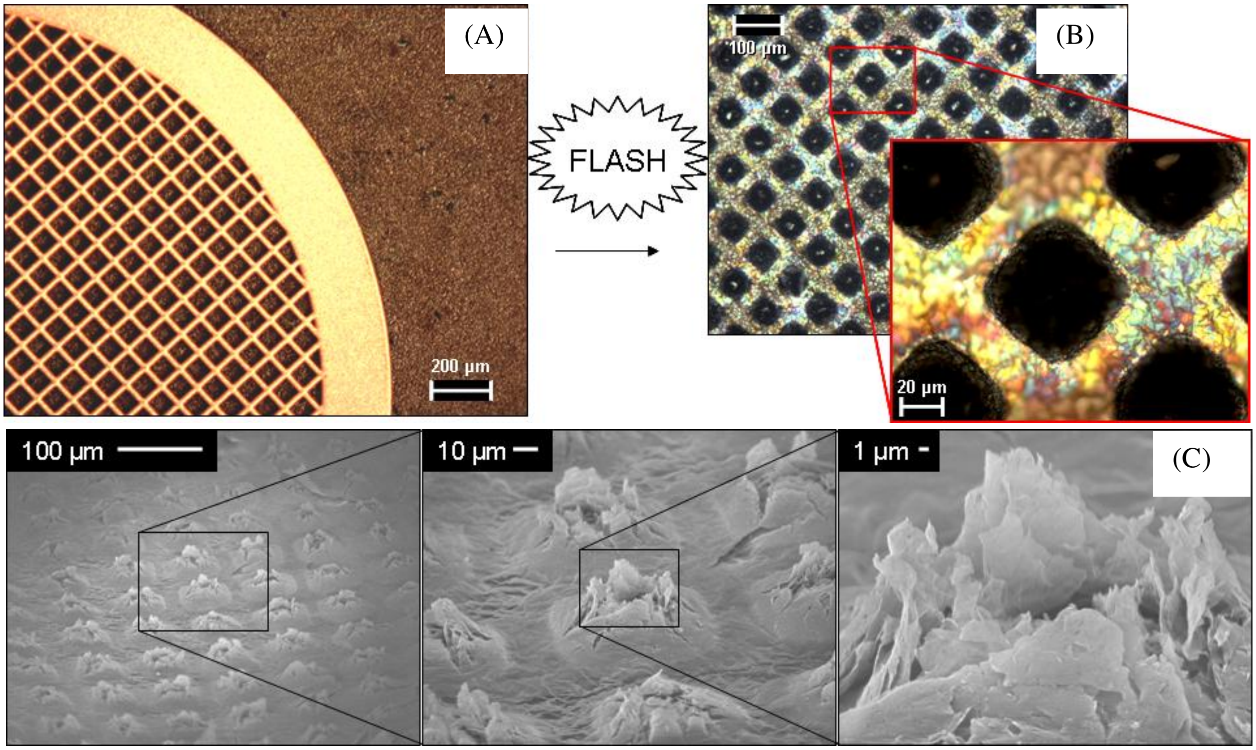

Figure 2.6 (a) An optical microscope image shows a GO film with a Cu transmission electron microscopy (TEM) grid on top before flashing. (b) After flashing and removing the TEM mask, the pattern of the TEM grid has been transferred to the GO film as seen in the optical microscope images. (c) The deoxygenation and subsequent release of CO_2 and H_2O blow the platelets of deoxygenated carbon out from the surface as depicted in series of SEM images at progressively higher magnifications.

2.3.5 Distributed Ignition

Another promising application for photothermally initiated reactions is as an ignition promoter for fuels. By dispersing GO platelets in a liquid fuel, it could be possible to initiate ignition of the fuel using a flash of light as opposed to a traditional spark plug. Illumination of a fuel/oxidizer mixture would enhance combustion by allowing ignition to occur at numerous locations simultaneously. One of the major drawbacks of current electrical spark ignition is that it is a single-point ignition source. Ideally, multiple ignition nucleation sites will allow for more controllable, and therefore more efficient and reliable ignition and combustion. This is of critical importance for applications such as liquid fueled rockets, where current ignition methods are known to be plagued by several problems. Issues such as combustion instability and start-up transients not only can cause severe damage, but also degradation in engine efficiency and an increase in emissions of pollutants. It is thought that nearly 30% of the combustion instabilities in rocket engines, leading to engine damage and possible loss of cargo and human life, can be traced back to the nature of the propellant's initial energy release process, as described by Harrje and Reardon.[39]

The short-comings of the existing systems combined with intuitive engineering advantages of low-energy, lightweight distributed ignition, has motivated previous attempts to use single wall carbon nanotubes (SWNTs) as photo-ignition enabling additives to fuels.[32-34] In these experiments, the SWNTs were found to only ignite in the presence of ambient oxygen and did not disperse well in the test fuels. Flashing of SWNTs is also heavily dependent on the Fe catalyst concentration. In contrast, GO carries its own oxygen supply and is highly dispersible in fuels such as alcohol; therefore, GO may be a promising additive as an ignition promoter for fuels.

In preliminary experiments, we have been able to successfully ignite ethanol fuels using GO as a photothermal initiator. Figure 2.3a shows a photo of a GO foam sample placed on a paper soaked with ethanol. Upon flashing (Figure 2.7b), the ethanol vapor readily combusts as a result of the GO ignition. After the ethanol fuel is consumed, we can see the deoxygenated carbon product glowing bright red as a result of the combustion reaction and the volume of the sample increases due to exfoliation (Figure 2.7c). Pyrometer readings of this ignition process indicate that by flashing GO achieves temperatures of 400-500 °C within a few ms. In our experiments, were able to disperse GO platelets into ethanol and methanol with mild sonication. The GO platelets did not disperse well in more aliphatic fuels such as kerosene. We speculate that dispersibility of GO in organics could be facilitated with the use of surfactants without loss of the photothermal function of GO platelets as an ignition promoter.

2.3.6 Homogeneous Charge Compression Ignition Engine.

Over the past decade, extraordinary efforts have been undertaken to both improve the fuel efficiency of traditional gasoline engines and search for clean, renewable alternative fuels to gasoline. One idea that has surfaced from this thrust is the notion of a homogeneous charge compression ignition (HCCI) engine that combines the high efficiency of a diesel engine with the low emissions of a spark ignition engine.

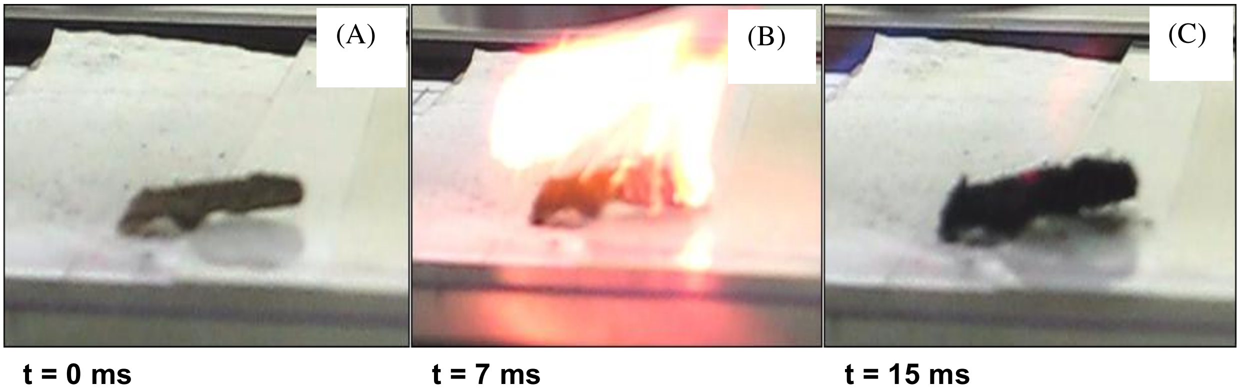

Figure 2.7 A series of photographs showing a GO foam sample before, during and after flash ignition with the time interval labeled in milliseconds (ms). By placing a GO foam sample onto a paper soaked with ethanol and flashing, the GO foam is capable of igniting the ethanol vapor as depicted in the center photograph. After ignition, the deoxygenated GO sample can be seen glowing red from the energy released during the reaction.

In a typical HCCI engine, fuel and air are mixed homogeneously like a spark ignition engine, but ignition occurs by means of auto-ignition under high compression similar to a diesel engine.[40] The high compression ratio of HCCI engines provides an efficiency increase of up to 15% over traditional spark ignition engines.[41,42] Currently, one of the major challenges facing HCCI engines has been controlling the unpredictable compression-induced ignition process. By using an ignition promoter such as GO, it could be possible to achieve distributed ignition in HCCI engines, thus providing accurate ignition timing, resulting in the homogeneous detonation of fuel and air.

2.4 Conclusions

Highly absorbing nanoparticulate materials are able to achieve a dramatic temperature increase upon exposure to short pulses of moderate intensity light. These temperature increases occur as a consequence of the high surface to volume ratio and low number of thermally conducting pathways by which to dissipate absorbed light energy. One of the distinguishing characteristics that sets photothermal ignition of GO apart from the flashing of other nanomaterials, is that instead of merely igniting or melting a material, an exothermic decomposition reaction occurs. The benefit of such a process is that the energy required for ignition is not provided solely by the source of the flash as it would be with other nanomaterials. This enables the use of lower power light sources and/or larger particles in order to achieve ignition, since the combustion of the particles themselves adds energy to the system. In the future, GO or other oxygen bearing, self-decomposing particles may make it possible to tune the photoignition behavior of a fuel to provide more controllable distributed ignition. In patterning applications, the solubility differences between GO and deoxygenated graphitic carbon could be used to quickly separate exposed and masked regions of a thin GO film. Using an organic solvent, the broken-up flashed areas of a GO film could be washed away leaving the masked GO portions intact. Subsequent thermal or chemical reduction of the patterned GO films to conducting, reduced GO would make it possible to create highly conducting patterns.

2.5 References

1. Ajayan, P. M.; Ramanath, G.; Terrones, M.; Ebbesen, T. W.; *Science,* **2002**, *297*, 192 – 193
2. Huang, J.; Kaner, R. B.; *Nature Nanotech.* **2004**, *3*, 783 – 786
3. Wang, N.; Yao, B. D.; Chan, Y. F.; Zhang, X. Y. *Nano Letters,* **2003**, *3*, 475 – 477
4. Ying, J. *Nanostructured Materials.* New York: Academic Press, **2001**
5. Brodie, B. *Ann Chim. Phys.* **1855**, *45*, 351
6. Dikin, D.; Stankovich, S.; Zimney, E. J.; Piner, R. D.; Dommett, H. B.; Evmenenko, G.; Nguyen, S. T.; Ruoff, R. S. *Nature,* **2007**, *448* (26), 457 – 460
7. Park, S.; Lee, K. S.; Bozoklu, G.; Cai, W.; Nguyen, S.; R. S. Ruoff; *ACS Nano,* **2008**, *2* (3), 572 – 578
8. Stankovich, S.; Dikin, D. A.; Piner, R. D.; Kohlhaas, K. A.; Kleinhammes, A.; Jia, Y.; Wu, Y.; Nguyen, S. T.; Ruoff, R. S. *Carbon,* **2007**, *45* (7), 1558 – 1565
9. Stankovich, S.; Piner, R. D.; Chen, X.; Wu, N.; Nguyen, S. T.; Ruoff, R. S.; *J. Mater. Chem.* **2006**, *16*, 155 – 158
10. Hofmann, U.; Frenzel, A. *Kolloid Z,* **1934**, *68*, 149 – 151
11. Tung, V. C.; Allen, M. J.; Yang, Y.; Kaner, R. B. *Nature Nanotech.* **2008**, *4*, 25 – 29
12. Li, D.; Muller, M. B.; Gilje, S.; Kaner, R. B.; Wallace, G. G. *Nature Nanotech.* **2007**, *3*, 101-105
13. Park, S.; An, J.; Piner, R. D.; Jung, I.; Yang, D.; Velamakanni, A.; Nguyen, S. T.; Ruoff R. S. *Chem. Mater.* **2008**, *20* (21), 6592 – 6594

14. Gilje, S.; Han, S.; Wang, M. S.; Wang, K. L.; Kaner, R. B. *Nano Lett*. **2007**, *7*, 3394 – 3398

15. Gomez-Navarro, C.; Weitz, R. T.; Bittner, A. M.; Scolari, M.; Mews, A.; Burghrd, M.; Kern, K. *Nano Lett*. **2007**, *7*, 3499 – 3503

16. Stankovich, S.; Dikin, D. A.; Dommett, G. H. B.; Kohlhaas, K. M.; Zimney, E. J.; Stach, E. A.; Piner, R. D.; Nguyen, S. T.; Ruoff, R. S. *Nature,* **2006**, *442* (7100), 282 – 286

17. Watcharotone, S.; Dikin, D. A.; Stankovich, S.; Piner, R.; Jung, I.; Dommett, G. H. B.; Evmenenko, G.; Wu, S. E.; Chen, S. F.; Liu, C. P.; Nguyen, S. T.; Ruoff, R. S. *Nano Lett*. **2007**, *7* (7), 1888 – 1892

18. Chen, H.; Muller, M. B.; Gilmore, K. J.; Wallace, G. G.; Li, D. *Adv. Mater*. **2008**, *999* (9), 1 – 5

19. Arsat, R.; Breedon, M.; Shafiei, M.; Spizziri, P. G.; Gilje, S.; Kaner, R. B.; Kalantar-zadeh, K.; Wlodarski, W. *Chem. Phys. Lett*. **2008**, *467* (4-6), 344 – 347

20. Stoller, M. D.; Park, S.; Zhu, Y.; An, J.; Ruoff, R. S. *Nano Lett*. **2008**, *8* (10), 3498- 3502

21. Cote, L. J.; Kim, F.; Huang J.; *J. Am. Chem. Soc*. **2009**, *101*, 1043 – 1049.

22. Goki, E.; Lin, Y. Y.; Miller, S.; Chen, C. W.; Su, W. F.; Chhowalla, M. *Appl. Phys. Lett.,* **2008**, *92*, 233305

23. Wang, X.; Zhi, L.; Tsao, N.; Tomovic, Z.; Li, J.; Muller, K. *Angew. Chem. Int. Ed*. **2008**, *47*, 2990 – 2992

24. Wu, J.; Bercerril, H. A.; Bao, Z.; Liu, Z.; Chen, Y.; Peumans, P.; *Appl. Phys. Lett*. **2008**, *92*, 263302

25. Goki, E.; Fanchini, G.; Chhowalla, M. *Nature Nanotech*. **2008**, *3*, 270 – 274

26. Li, X. L.; Zhang, G.; Bai, X.; Sun, X.; Wang, X.; Wang, E.; Dai, H. *Nature Nanotech.* **2008**, *3*, 538 – 542.

27. Schneipp, H. C.; Li, J. L.; McAllister, M. J.; Sai, H.; Herrera-Alonso, M.; Adamson, D. H.; Prud'homme, R. K.; Car, R.; Saville, D. A.; Aksay, I. A. *J. Phys. Chem. B.* **2006**, *110*, 8535 – 8539.

28. Li, J. L.; Kudi, K. N.; McAllister, M. J.; Prud'homme, R. K.; Aksay, I. A.; Car, R. *Phys. Rev. Lett.* **2006**, *96*, 176101.

29. Ramanathan, T.; Abdala, A. A.; Stankovich, S.; Dikin, D. A.; Herrera-Alonso, M.; Piner, R. D.; Adamson, D. H.; Schniepp, H. C.; Chen, X.; Ruoff, R. S.; Nguyen, S. T.; Aksay, I. A.; Prud'homme, R. K.; Brinson, L. C.; *Nature Nanotech.* **2008**, *3* (6), 327 – 331.

30. Boehm, H. P.; Scholz, W. *Zeitschrift fur anorganische und allegemeine Chemie,* **1965**, *335*, 74 – 79.

31. Zuckerman, J. J.; Hagen, A. P. *Oligomerization and Polymerization Formation of Intercalation Compounds*, *Volume 17, Inorganic Reactions and Methods*. New York, VCH Publishers Inc.**1990**.

32. Chehroudi, B.; Danczyk, S. A. Global Powertrain Congress World Powertrain Exposition. Novi Michigan. September **2006**.

33. Sciamanna, S.; Munson, C.; Dieckmann, G. US Patent Appl #11/613,10

34. Beiver, C. *New Scientist Magazine* **2005**, 2526, 30

35. Braidy, N.; Botton, G. A.; Adronov, A. *Nano Lett.* **2002**, *2*, 1277 – 1280

36. Smits, J.; Wincheski, B.; Namkung, M.; Crooks, R.; Louise, R. *Mater. Sci. Eng. A* **2003**, *358*, 384 – 389.

37. Chiang, I. W.; Brinson, B. E.; Huang, A. Y.; Willis, P. A.; Bronikowski, M. J.; Margrave, J. L.; Smalley, E. R.; Hauge, R. H. *J. Phys. Chem. B*. **2001**, *105* (35), 8297 – 8301.

38. Chen, H.; Diebold, G. *Science* **1995**, *270*, 963 – 966

39. Harrje, D. T.; Reardon, F. H.; Liquid propellant rocket combustion instability, NASA SP-194, *Scientific and Technical Information Office*, Washington, D.C. **1972.**

40. Chehroudi, B.; Homogeneous charge compression ignition (HCCI) engine, *Powertrain International* **2002**, *5*(1), 6 – 10.

41. Magnus, S.; Dec, J. E.; Cernansky, N. P. *Society of Automotive Engineers*. **2005**, *1*, 0113.

42. Fukwon, Z.; Asmus, T. W.; Assanis, D. N.; Dec, J. E.; Eng, J. A.; Najt, P. M. *Society of Automotive Engineers* **2**

Chapter 3

A One-Step, Solvothermal Reduction Method for Producing Reduced Graphene Oxide Dispersions in Organic Solvents

3.1 Introduction

Graphene oxide (GO) is an atomically thin, water-dispersible platelet material, resulting from the treatment of graphite with powerful oxidizing agents.[1,2] During oxidation, the graphene sheets—of which the bulk graphite is composed—become functionalized with hydroxyl and epoxide groups on their basal plane, while the edges are decorated with carbonyl and carboxyl groups.[3-5] Several authors have reported the ability to reduce GO to graphene-like carbon sheets through the application of either thermal treatment[6-8] or chemical reducing agents,[9-17] which in turn led to speculation that GO could find use as a precursor in a bulk route to graphene sheets.[10,14,18] Several groups have succeeded in creating conducting polymer composites, transparent conducting films, and simple electronic devices based on reduced GO.[17,19-31] In addition to the chemical reduction, Aksay *et al*. have reported the thermal deoxygenation of GO, by rapidly heating samples up to 1100 °C in an inert atmosphere as a route to partially "functionalized" graphene sheets.[7,32] These organic solvent-dispersible sheets have enabled the direct creation of polymer composites without the need for surfactants.[33] Recently, Chen *et al*. have investigated the possibility of using isocyanate-modified graphite oxide as an acceptor material in bulk heterojunction organic photovoltaic cell devices. [34] The device efficiency reported was 1.1% for samples annealed at 160 °C, which is an order of magnitude improvement from non-annealed devices. The authors explain this phenomenon as a loss of oxygen-containing functional groups from isocyanate-treated graphite oxide and subsequent recovery of aromatic regions. Unfortunately, the annealing temperature cannot exceed 160 °C, due to device constraints, and most of the oxygen-containing functionalities are not removed before 200 °C, potentially limiting the device efficiency.[35]

Although several authors have reported organic dispersions of graphene-like materials, most of these methods utilize strong reducing agents such as hydrazine to achieve high conductivity.[36,37] The use of hydrazine could be problematic for the use of GO-derived graphitic materials for a number of reasons: (1) Being a powerful reducing agent, hydrazine is corrosive and highly flammable, thus posing a potential health hazard to personnel and an environmental hazard for facilities that might produce hydrazine-reduced GO.[38] These hazards could significantly increase the cost of producing reduced graphite oxide (RGO)-based materials on an industrial scale. (2) Trace amounts of hydrazine could be detrimental to some applications such as organic solar cells, where reducing agents such as hydrazine could reduce solar cell donor compounds like poly(3-hexylthiophene), thus increasing the complexity of photovoltaic cell manufacturing.[38] (3) Eliminating hydrazine from the production process would ease the integration of graphene dispersions into current manufacturing processes such as spray-on coatings. Here we report a simple one-step solvothermal approach to synthesizing organically dispersible graphitic platelets from GO that is hydrazine-free.

Our solvothermal reduction method utilizes the high boiling point of *N*-methyl-2-pyrrolidinone (NMP) in combination with the oxygen-scavenging properties of NMP at high temperatures to deoxygenate GO.[39,40] This combination of thermal and chemical deoxygenation yields C/O ratios for the resulting solvothermally reduced graphene oxide (SRGO) that are very similar to those for the hydrazine-reduced GO. In addition to simply deoxygenating GO to produce a more conducting graphitic material, NMP also serves as a dispersing agent for the resulting SRGO sheets by forming strong NMP–GO sheet interactions, thus allowing the sheets to be dispersed in any NMP miscible solvents.

Applications that can take advantage of the suggested synthesis include bulk heterojunction (BHJ) solar cells, where SRGO sheets can be mixed with P3HT and act as an acceptor component of the BHJ photovoltaic cell. Papers obtained through filtration or casting of layered SRGO platelets could potentially be used in place of copper as electromagnetic interference (EMI) shielding materials for signal carrying cables. This is of particular importance in aerospace applications where the lower density of carbon-based materials could lead to significant weight savings over current copper braids. By switching to a carbon-based shielding material, a weight saving of several hundred pounds could be achieved for satellite payloads and several thousand pounds for commercial aircraft.[41] Given the current cost of launching payloads into orbit (~$10 000 USD/lb), this could greatly impact the cost of future space launches.

3.2 Experimental

3.2.1 Synthesis

In order to generate a stable colloid, a 0.05 wt % GO dispersion in water was sonicated at 50 °C for 60 min using a VWR Ultrasonic Cleaner (B2500A-DTH, 210W) and diluted 1:1 with anhydrous 1-methyl-2-pyrrolidinone (NMP, ACS reagent grade 328634, Sigma-Aldrich). The light brown dispersion obtained was then degassed for 60 min under vacuum to remove any residual atmospheric oxygen present in the mixture. The solution was then purged with argon and placed in a sand bath preheated to 240 °C. The temperature of 240 °C allowed us to reach the reflux faster through rapid elimination of water. The mixture was then allowed to reflux at ~ 205 °C, as monitored by a mercury thermometer, for 24 h under flowing argon, after which it was filtered through an Anodisc alumina membrane filter (47 mm diameter, 0.2 μm pore size, Whatman, UK) and washed with pure NMP. The final product was centrifuged at 4500 rpm using a Beckman-Coulter Allegra X-15R centrifuge, saving the supernatant. The supernatant was filtered once again, rinsed with acetone, and allowed to dry on the filter paper under ambient conditions, which will be referred to as the SRGO air-dried paper. Furthermore, several samples of SRGO paper were enclosed in a tube furnace under a flow of helium gas and annealed at temperatures of 250, 500, and 1000 °C. To make organic dispersions, SRGO paper was sonicated at a 1 mg/mL ratio in the following organic solvents for 3 h at 50 °C: dimethylsulfoxide (DMSO), ethyl acetate, acetonitrile, ethanol, tetrahydrofuran (THF), dimethylformamide (DMF), chloroform, acetone, toluene, and dichlorobenzene.

3.2.2 Characterization

Atomic force microscopy (AFM) measurements were performed in tapping mode on a Multimode atomic force microscope (Nanoscope IIIa, Veeco Instruments) using a silicon tip. Samples were prepared using a 1 mg/mL solution of SRGO in DMF, which was drop-cast onto a freshly cleaned Si substrate and dried in the vacuum oven. Near-edge X-ray absorption spectroscopy (NEXAFS) was taken at Beamline 8-2 Stanford Synchrotron Radiation Lighsource in Menlo Park, CA. X-ray absorbance was measured using total electron yield (TEY) measurement under ultrahigh vacuum conditions. All spectra were plotted by dividing incident intensity (I_o) over TEY output. The spectra were normalized by subtracting a baseline average just before the carbon K-edge and dividing by the integrated intensity of the carbon K-edge peak.

Scanning electron microscope (SEM) analysis was carried out on both the SRGO papers and single sheets. For the cross-sectional analysis of the paper samples, the samples were mounted on the SEM sample holder parallel to the electron beam. Imaging of single sheets of SRGO and dispersions of SRGO were performed by depositing 1 mg/mL SRGO acetone onto a freshly cleaned Si substrate and allowing the acetone to evaporate. X-ray diffraction (XRD) characterization was performed using SRGO air-dried paper on zero background silicon substrate in a Crystal Logic diffractometer with Ni-filtered Cu Kα radiation (λ = 1.5418 Å). Thermal gravimetric analysis (TGA) of all samples was carried out under an argon gas and a heating rate of 2 °C/min. Photoelectron spectroscopy (XPS) was performed by inserting samples into the analysis chamber of a Thermo VG ESCALAB 250 spectrometer. Spectra were obtained by irradiating each sample with a 320 μm diameter spot of monochromated aluminum Kα X-rays at 1486.6 eV under ultrahigh vacuum conditions. The analysis consisted of acquiring 3–12 scans and signal averaging. The survey scans were acquired with a pass energy of 80 eV, and high-resolution scans were acquired with a pass energy of 20 eV. Electrical measurements were performed using a four-point probe measurement station (Jandel RM3-AR Test Meter with Multiheight Probe attachment), and the average of three data points per sample was recorded.

3.3 Results and Discussions

3.3.1 Stability of Organic Dispersions

Filtering the SRGO dispersion yields a paper-like material that can be dispersed into organic solvents (Figure 3.1). Stable colloidal dispersions can be achieved with dimethylsulfoxide (DMSO), ethyl acetate, acetonitrile, ethanol, tetrahydrofuran (THF), dimethylformamide (DMF), chloroform, and acetone with minimal precipitation at 1 mg/mL after 6 weeks. SRGO does not disperse in toluene or dichlorobenzene, but instead, flocculation was observed shortly after sonicating for 3 h. The forces keeping the sheets dispersed in organic solvents likely arise from the miscibility between NMP molecules, which form hydrogen bonds to residual oxygen functionalities on SRGO sheets, and organic solvents. A previous report[42] indicates that NMP forms hydrogen bonds with the conducting polymer polyaniline; hence, we suggest that a similar interaction takes place here. To test this hypothesis, we added a few drops of hydrochloric acid solution to several organic solutions, among them NMP, DMF, and DMSO. This resulted in agglomeration and precipitation of SRGO sheets. These experiments strongly suggest that hydrogen bonding between SRGO sheets and NMP is responsible for the stability of the colloidal suspensions.

While hydrogen bonds can account for the stability of SRGO sheets in NMP, DMF, and DMSO, it still does not offer a reason why synthesis carried out in DMF, DMSO, glycerol, and hexamethylphosphoramide (HMPA) results in agglomerated sheets instead of colloidal dispersions. However, note that all of these chemicals are high boiling point solvents and refluxing at high temperatures is necessary to remove any water molecules bound through hydrogen bonds to graphene oxide. In addition, all of the solvents provide means for hydrogen bonding to various degrees, in order to prevent an agglomeration of the sheets in the absence of water. We suspect the answer may be the fact that NMP, unlike other solvents listed above, has a surface energy that closely matches that of graphene sheets allowing exfoliated sheets to stay in dispersion.[43] NMP has also been suggested to cause cleavage of carbon−oxygen bonds in coals when used under refluxing conditions.[39] In these reactions, a hydroperoxide is thought to be an intermediate in the reaction of NMP and oxygen-yielding *N*-methylsuccinimide.[40] In our experiments, pure NMP changes color from clear to brown when refluxed under atmospheric oxygen. We attribute the color change of NMP in the presence of oxygen to oligomer formation, which has been reported previously.[40] Filtration of SRGO from the reaction mixture yields a dark brown solution, indicating that oxygen is present in the mixture and oligomer formation has occurred. It is unclear at this point what role the oligomer formation plays in the reduction of GO or its ability to form colloidal dispersions of SRGO. Our experiments show that it is imperative to use anhydrous and degassed NMP for the reaction with graphene oxide in order to prevent the self-oligomerization of NMP.

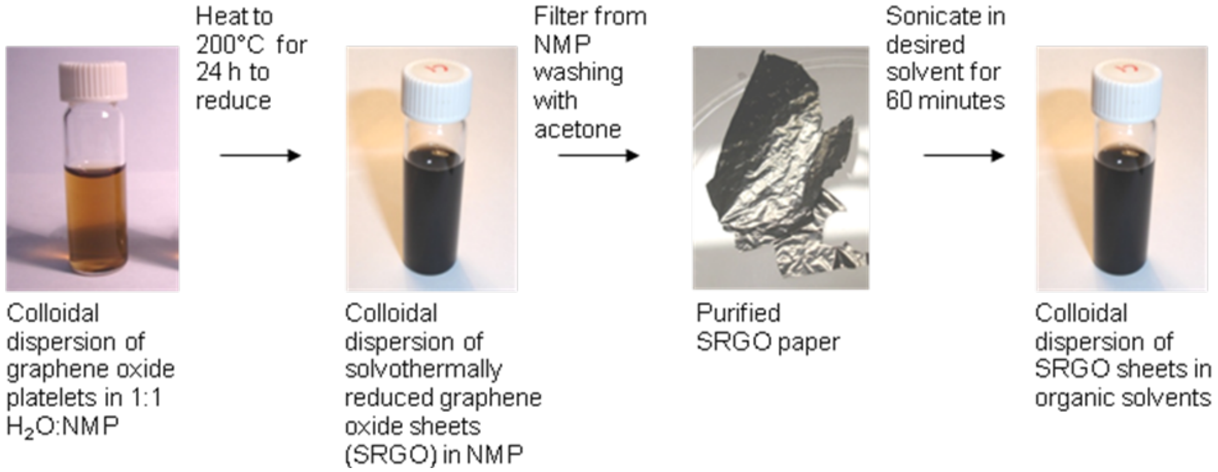

Figure 3.1. A schematic diagram shows the preparation and purification of solvothermally reduced graphene oxide (SRGO) to create homogeneous colloidal dispersions of SRGO sheets.

3.3.2 Evaluations of Films by Electron Microscopy

Atomic force microscopy (AFM) was used to analyze SRGO sheets cast onto a Si substrate from a dispersion of SRGO platelets in DMF. Figure 3.2a shows an AFM image of SRGO sheets deposited from a 1 mg/ml DMF dispersion onto a Si substrate. Figure 3.2b shows a 0.93 nm step height from the surface of the substrate to the sheet. The theoretical step height for a single graphene sheet is 0.34 nm; however, this is only observed when sheets are removed from HOPG or other highly crystalline graphite, by means such as peeling with cellophane tape.[44] RGO obtained from hydrazine has been measured to have a step height in the range of 0.6 to 1.0 nm. We believe the sheets measured using AFM in Figure 3.2a to be single SRGO sheets; however, AFM measurements alone do not provide conclusive evidence that single RGO sheets are obtained using the solvothermal process. We speculate that the increased step height of hydrazine RGO (HRGO) may be attributed to residual functionality on the surface of the sheet, causing some corrugation in the surface of the sheet.[7] Figure 3.2c presents a SEM image of a 1 mg/ml acetone SRGO dispersion deposited onto a Si substrate. The image illustrates that the SRGO sheets are distributed across the Si substrate. The inset in Figure 3.2c shows a closer view of a single sheet as deposited onto the Si substrate. Figure 3.3a is an SEM image of the cross-sectional area of a piece of air-dried SRGO paper obtained by filtration of an SRGO dispersion in NMP that shows the layer structure of these materials. The inset image in Figure 3.3a is a photograph of an SRGO paper exhibiting a shiny, black appearance with a metallic luster. SRGO papers were thermally annealed at 1000 °C under an argon atmosphere to drive off any unreacted contaminants. After annealing, we see that the layered structure is preserved (Figure 3.3b). This demonstrates that the SRGO platelets are thermally stable in the absence of oxygen.

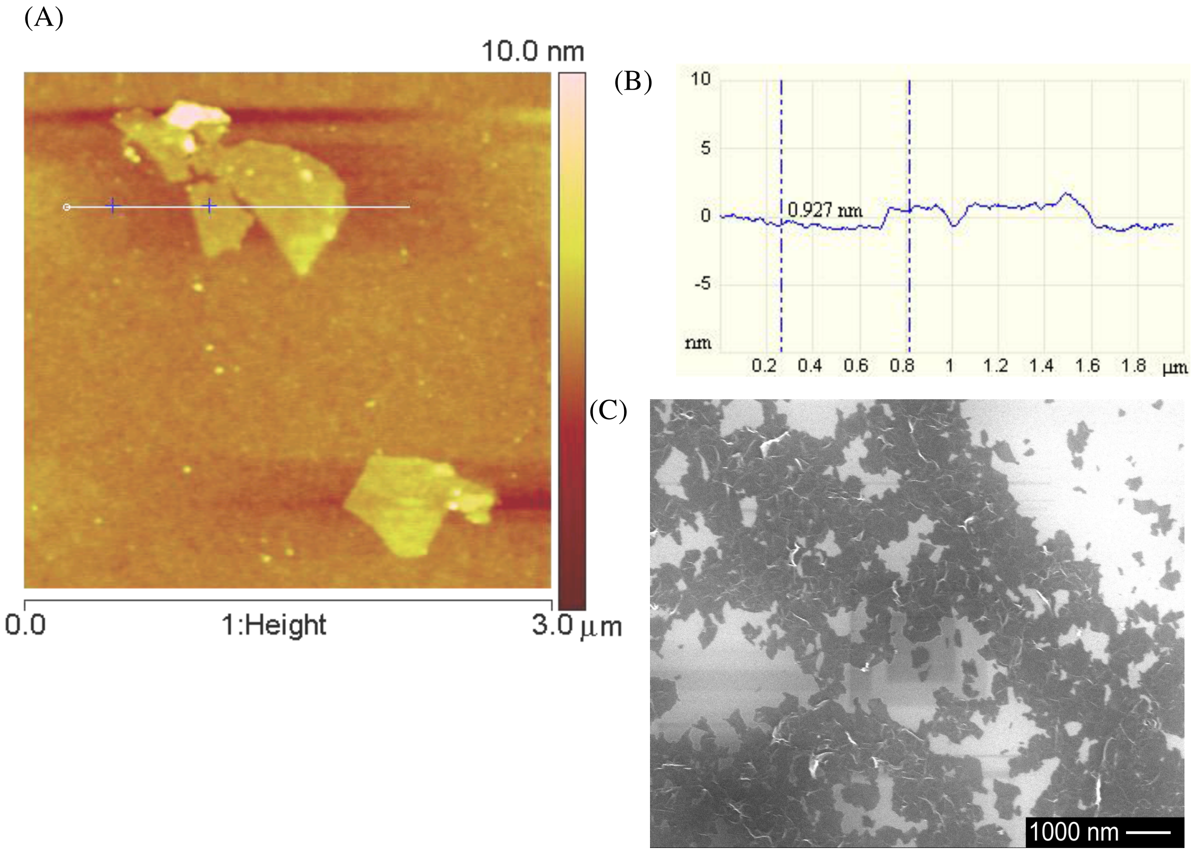

Figure 3.2 (a) AFM image of SRGO sheets; (b) corresponding AFM height profile from (a) indicates a 0.93 nm sheet thickness. (c) SEM images of SRGO sheets indicate well-dispersed sheets after deposition on Si substrate; inset shows a highly magnified single sheet of SRGO.

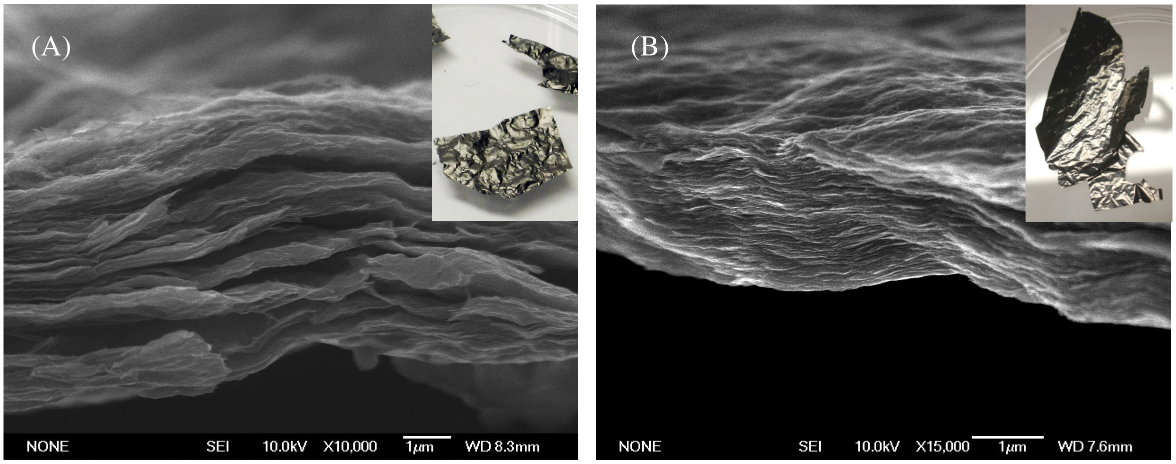

Figure 3.3. (a) SEM image of a cross-sectional area of the air-dried SRGO film. Inset shows SRGO paper filtered on Anodisc alumina membrane, producing a shiny, black film with metallic-like luster. (b) SEM image of SRGO paper sample annealed at 1000 °C for 12 h under argon indicates that the SRGO paper retains layered structure after annealing. Inset shows SRGO annealed paper gaining a silver/gray appearance after annealing.

3.3.3 X-Ray and Gravimetric Analysis

An X-ray diffraction (XRD) pattern of the GO paper (Figure 3.4a, middle) exhibits a single peak at 11.26° 2θ corresponding to an interlayer *d* spacing of 7.85 Å. This can be attributed to the expansion of the 3.4 Å spacing between typical graphene sheets to accommodate the water molecules trapped between oxygen-containing functional groups on graphene oxide sheets.[45-48] In contrast to the XRD pattern of GO paper samples, the XRD pattern of SRGO (Figure 3.4a, bottom) does not have a peak at 11.26° 2θ yet shows a broad peak at 26.24° 2θ (3.39 Å) well within experimental measurement error for a graphitic peak at 3.35 Å (Figure 3.4a, top). The width of the SRGO peak in the XRD pattern can be attributed to two factors: first, the small sheet size (1 μm and below) and, second, a relatively short domain order or turbostratic arrangement of SRGO stacked sheets, each of which broadens the XRD peak. In Figure 3.4b, a thermogravimetric analysis (TGA) plot shows a loss of about 15 wt % before 100 °C, which can be attributed to loss of water molecules from within the stacked graphene oxide sheets. A TGA curve of the SRGO paper, in contrast, shows a smaller mass loss (6%) up to 200 °C, signifying that a smaller amount of water or acetone molecules was trapped within the SRGO structure. Furthermore, the TGA of the SRGO paper shows a mass loss of 20% from 200 to 525 °C, followed by a flattening of the curve at higher temperatures. These preliminary findings suggest the mass loss between 200 and 550 °C may be associated with strongly bound NMP and/or NMP-derived functional group molecules.

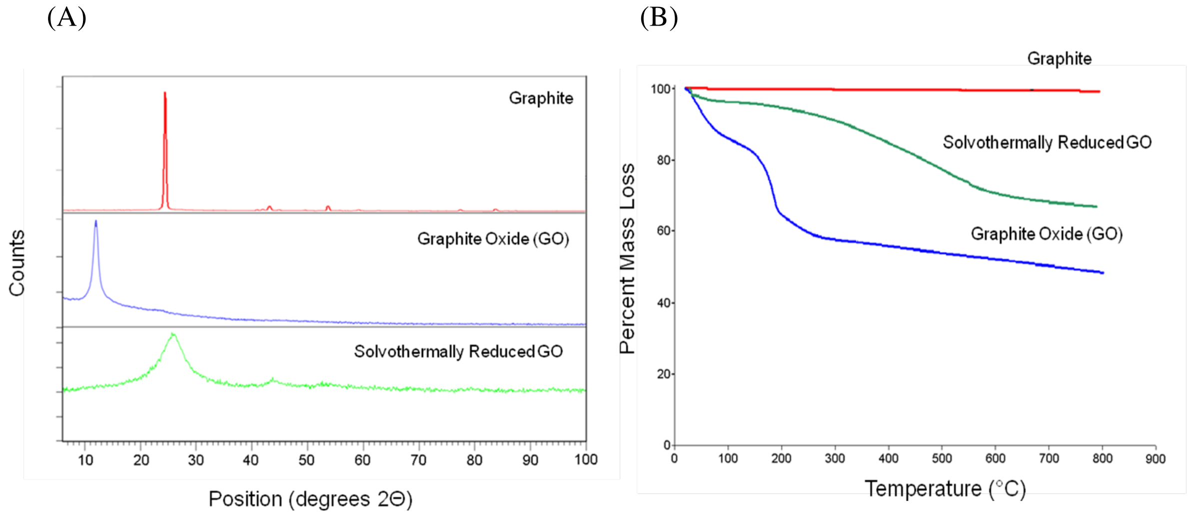

Figure 3.4 (a) XRD of graphite (top), graphite oxide (middle), reduced graphite oxide (bottom). (b) Thermal gravimetric analysis (TGA) plot shows a normalized remaining mass of graphite oxide, graphite, and reduced graphite oxide heated under argon.

3.3.4 Conductivity Measurements

The four-point probe electrical conductivity of air-dried SRGO paper was measured to be 3.74×10^2 S/m as indicated in Table 3.1. On the basis of the TGA data, it is apparent that the SRGO paper still retains a significant portion of NMP, which limits the electrical conductivity. To remove any residual NMP (boiling point = ~203 °C) trapped within the paper samples, three SRGO paper samples were annealed at ~250, 500, and 1000 °C for 12 h in a tube furnace under a flow of helium gas. The samples developed a gray hue and even became lustrous silver as the annealing temperature approached 1000 °C, yet still retained their layered structure, as can be seen in Figure 3.3b. As we have previously suggested, NMP bonds strongly to carbon networks, necessitating the higher temperatures to remove residual NMP. Previous reports indicate that annealing to 500 °C has been shown to remove up to 95% of the residual NMP. However, by annealing the sample to only 250 °C, we sought to eliminate NMP, without subjecting the sample to significant thermal reduction. As shown in Table 3.1, the result is an order of a magnitude rise in conductivity from 3.74×10^2 to 1.38×10^3 S/m. This phenomenon can be explained by the interaction of NMP molecules with the surface of the sheets, thus preventing good contact between adjacent sheets. Through the elimination of residual NMP, the contacts between sheets are improved and conductivity increases. Further annealing to 500 °C demonstrates that conductivity will continue to increase, but at a slower rate, reaching 5.33×10^3 S/m. Annealing the sample to 1000 °C further increases the conductivity to 5.73×10^4 S/m, which indicates that a considerable amount of graphitization has taken place.

Table 3.1. Electrical Conductivities of solvothermally reduced graphite oxide (RGO) paper samples prepared by various methods and their comparison to hydrazine RGO samples.

Description	Drying conditions	Conductivity (S/m)
Solvothermal RGO	Air dried	3.74×10^2
	Annealed at 250 °C	1.38×10^3
	Annealed at 500 °C	5.33×10^3
	Annealed at 1000 °C	5.73×10^4
Hydrazine RGO*	Air dried	8.28×10^3
	Annealed at 1000 °C	6.67×10^4
GO boiled in H_2O for 24 hours	Air dried	1.00×10^1
GO	Air dried	Insulator

* Reproduced from Li et al. [10]

3.3.5 XPS Characterization

To further investigate the nature of SRGO, we employed X-ray photoelectron spectroscopy (XPS) to analyze the elemental composition of both reduced and unreduced graphene oxide paper. XPS analysis has been used in the past to determine atomic composition and carbon to oxygen (C/O) ratios of GO and RGO. Reduction of GO to RGO is usually indicated by an increase in the C/O ratio and, in the case of hydrazine reduction, uptake of some nitrogen.[18] Figure 3.5 is a comparison of XPS spectra of GO to the SRGO paper, exhibiting a decreased peak intensity for all oxygen-containing functional groups yet an increase in peak intensity for the C–C bond.[46,49] Additionally, SRGO exhibited a peak at 285.8 eV, corresponding to a carbon–nitrogen bond. It is possible that SRGO sheets have attained a certain amount of carbon–nitrogen bonds through functionalization during the refluxing in NMP. Although the SRGO used for XPS analysis had been washed extensively using acetone, some residual NMP could be present at the sheet surface, resulting in the presence of a C–N XPS peak. The exact mechanism of this C–N bond formation is still being investigated, but prior reports indicate that this is not a new phenomenon and has been observed previously.

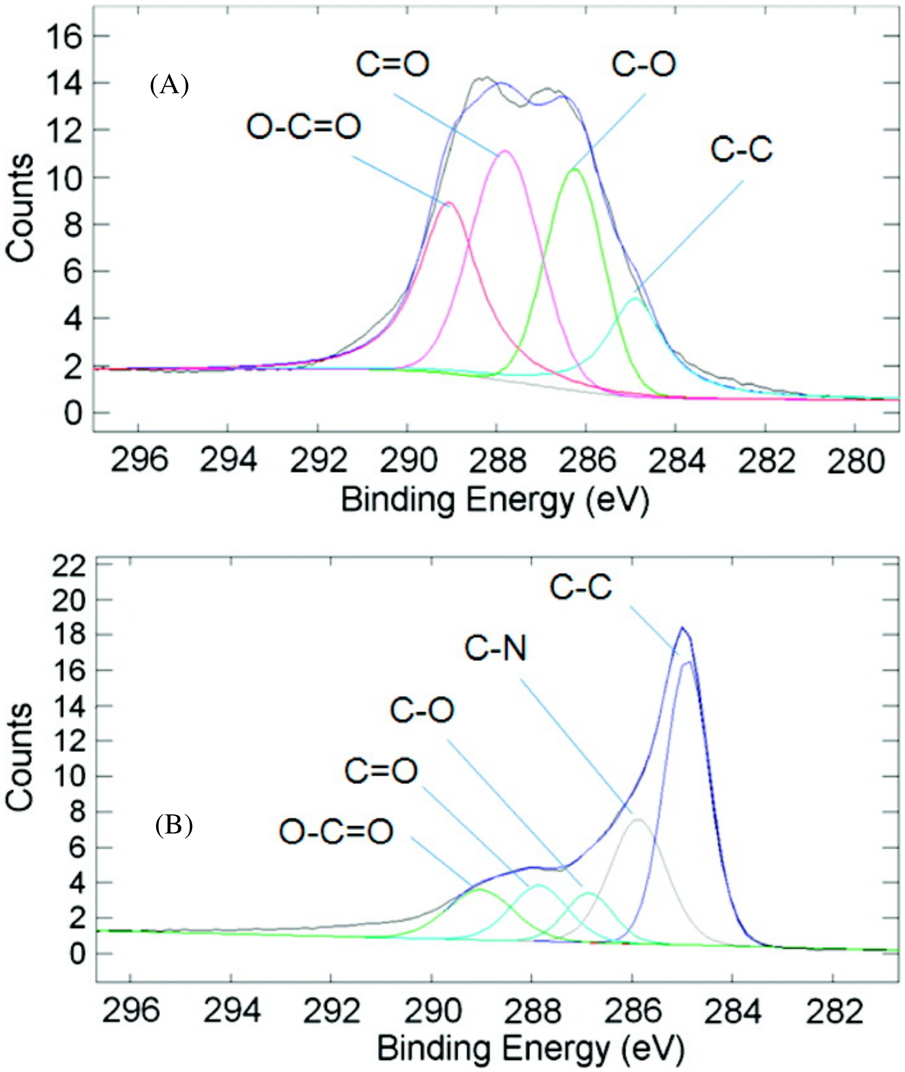

Figure 3.5 (a) XPS C1s of GO paper and the corresponding deconvoluted peaks of GO are shown. (b) XPS C1s of air-dried SRGO and the corresponding deconvoluted peaks

The results of the XPS analysis are listed in Table 3.2. The samples tested were obtained by filtering dispersions of SRGO directly from NMP after the solvothermal reaction to obtain a paper. The SRGO paper was then redispersed in acetone using sonication and filtered a second time to remove impurities. In addition to the solvothermally reduced GO, we also tested GO that had been reduced using the hydrazine reduction method previously reported by Li *et al*.[10] Looking at Table 3.2, we see that the GO C/O ratio increases from 2.34 to 5.15 after thermal reduction in NMP. Further annealing of SRGO papers at 1000 °C enhances the C/O ratio to 6.03. Papers made from GO platelets that had been reduced using hydrazine exhibited a C/O ratio of 3.64. When the hydrazine RGO papers were annealed at 1000 °C, the C/O ratio reached up to 6.36. We attribute the higher C/O ratio of the SRGO *versus* the hydrazine RGO to the bound functional groups at the surface of the SRGO platelets. When NMP is heated in the absence of GO, the rings typically break open, forming oligomers. In the presence of GO, however, we believe the opened NMP rings functionalize the GO basal planes, thus increasing the carbon content—and C/O ratio—as measured by XPS. When SRGO and hydrazine RGO are annealed, both reduction methods exhibited similar C/O ratios, with hydrazine RGO having a slightly higher ratio over SRGO. If the basal planes in SRGO are in fact being functionalized by NMP, annealing at 1000 °C could serve to drive off this functionality. The results of the XPS data along with the electrical conductivity data indicate that, although the C/O ratio of SRGO is higher, the increase is most likely due to functional groups decorating the surface of the GO sheets and not an improved deoxygenation.

Table 3.2. List of the Atomic Composition of Solvothermal Reduced Graphite Oxide (RGO) and Hydrazine RGO As Measured by X-ray Photoelectron Spectroscopy (XPS)

Description	Drying conditions	C (atomic %)	O (atomic%)	N (atomic %)	C/O Ratio
Solvothermal RGO	Air dried	80.4	15.6	4.0	5.15
Solvothermal RGO	Annealed at 1000 °C	83.2	13.8	3.0	6.03
Hydrazine RGO*	Air dried	76.0	21.0	3.0	3.62
Hydrazine RGO*	Annealed at 1000 °C	84.5	13.3	2.2	6.36
GO boiled in H_2O for 24 hrs	Air dried	75.4	21.1	0.5	3.12
GO	Air dried	69.3	29.3	1.1	2.34

* Reproduced from Li *et al*.[10]

3.3.6 NEXAFS Analysis

Near-edge X-ray absorption fine structure (NEXAFS) spectroscopy of GO, SRGO, and hydrazine RGO (HRGO) that had been annealed at 1000 °C was performed. Figure 3.6 shows an overlay plot of the carbon K-edge NEXAFS spectra for the series of RGOs that were treated using different means. At the very bottom of Figure 3.6 is the carbon K-edge NEXAFS spectrum for pristine GO. The high peak at 284.5 eV corresponds to the π* → 1s transition associated with sp^2 carbon content. For the series of spectra in Figure 3.6, all of the samples tested were measured at a 20° grazing angle, incident to the incoming X-ray beam. Doing so aligns the highly polarized π orbitals to the polarization of the X-ray beam, increasing the measured intensity. Peaks at 287.4 and 288.2 eV correspond to −C−O and −C═O, respectively. In the case of GO, the −C−O peak is taken to represent the C−OH content. Finally, the broad peak located at ~292.7 eV corresponds to the π* → 1s associated with sp^3 content. Annealing carbonaceous materials has been known for some time to increase the graphitic content. By annealing the RGOs that had already been reduced by low-temperature thermal or chemical means, we hoped to track changes in the GO crystallinity. From Figure 3.6, the sp^2 peak appears to be much higher in intensity for the annealed samples *versus* the non-annealed RGOs. In both cases, the annealed samples show fewer oxygen defects due to C−O, as well. Comparing the hydrazine reduction to the solvothermal reduction, it seems that hydrazine yields more sp^2 carbon with less C−O. The reduction in oxygen defects could be due to the preferential attack of hydrazine to ether linkages and epoxide groups present on the graphene oxide surface.

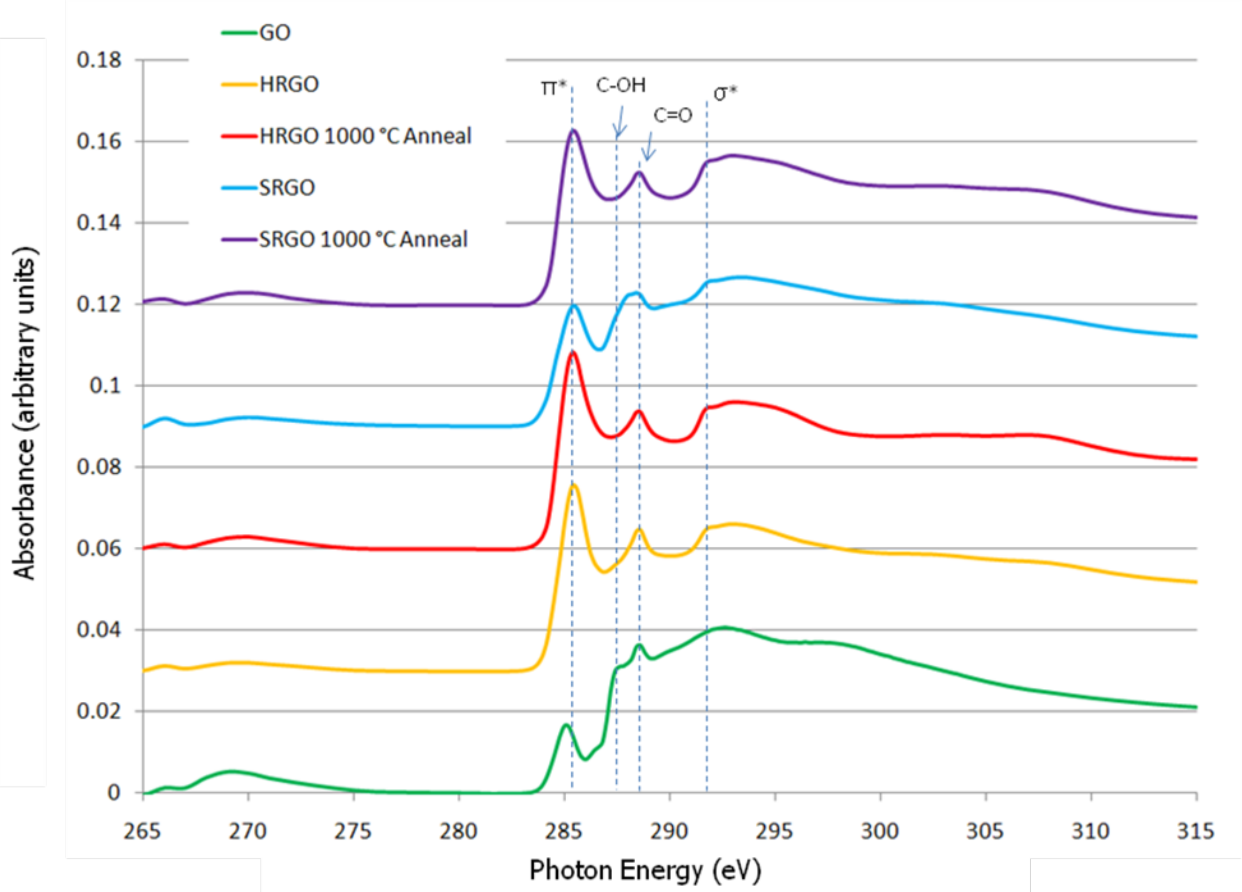

Figure 3.6 Overlay plot of the normalized near-edge X-ray absorbance fine structure (NEXAFS) spectra taken at the carbon K-edge for RGOs obtained through various treatments. Each spectrum was taken at 20° incident grazing angle with respect to the X-ray beam. The peak at ~ 284.5 eV corresponds to the sp^3 carbon π* transition. Smaller peaks at 287.4 and 288.2 eV correspond to oxygen defects. From the overlay, SRGO contains slightly more C–OH with a smaller sp^2 content than HRGO. Annealing SRGO and HRGO at 1000 °C increases the intensity of the π* transition, indicating higher sp^2 content. After annealing, some –C═O content does remain.

3.4 Conclusions

We have demonstrated a new method for thermally deoxygenating GO to create reduced graphene oxide dispersions without the use of hydrazine as a reducing agent. We believe that the deoxygenation of GO platelets takes place as the result of both thermal deoxygenation at 200 °C along with a concomitant reaction of GO with NMP molecules.[50] As a result of the surface functionalization, the solvothermally reduced GO platelets remain in a stable dispersion after the reaction. This provides a simple, low-temperature method for reducing GO platelet. Filtration of the SRGO platelets from the reactant NMP mixture removes excess NMP along with oligomer contaminants that form during the reaction. The resulting SRGO material can be redispersed into in a variety of polar organic solvents for potential applications in solar cells or polymer nanocomposites, where traces of hydrazine may prove detrimental for mass production. Filtration of organic SRGO dispersions yields paper materials with an initial conductivity of 3.74×10^2 S/m. With modest heating to 250 °C to remove entrapped solvent, the conductivity of the SRGO paper increases to 1.38×10^3 S/m while preserving the low-temperature benefits of our solvothermal method. Although this conductivity value is not quite as high as the 8.28×10^3 S/m measured for hydrazine-reduced GO, it may be still suitable for a variety of applications such as EMI shielding of signal cables. In this role, SRGO papers could offer suitable shielding but at lower weight than current copper braids; this is especially important in reducing weight in satellites and aircraft. With additional chemical processing, such as oxidative intercalation, it is expected that the conductivity of these SRGO-based papers could be increased even further.

3.5 References

1. Kovtyukhova, N. I.; Ollivier, P. J.; Martin, B. R.; Mallouk, T. E.; Chizhik, S. A.; Buzaneva, E. V.; Gorchinskiy, A. D. *Chem. Mater.* **1999**, *11* (3), 771 – 778
2. Brodie, B.C. *Phil. Trans. R. Soc. Lond.* **1859**, *149*, 249 – 259
3. Lerf, A.; He, H.; Forster, M.; Klinowski, J. *J. Phys. Chem. B* **1998**, *102* (23), 4477 – 4482
4. Cai, W.; Piner, R. D.; Stadermann, F. J.; Park, S.; Shaibat, M. A.; Ishii, Y.; Yang, D.; Velamakanni, A.; An, S. J.; Stoller, M.; An, J.; Chen, D.; Ruoff, R. S. *Science* **2008**, *321*, 1815 – 1817
5. He, H.; Riedl, T.; Lerf, A.; Klinowski, J. *J. Phys. Chem.* **1996**, *100*, 19954
6. McAllister, M. J.; Li, J. L.; Adamson, D. H.; Schniepp, H. C.; Abdala, A. A.; Liu, J.; Herrera-Alonso, M.; Milius, D. L.; Car, R.; Prud'homme, R. K.; Aksay, I. A. *Chem. Mater.* **2007**, *19*, 4396 – 4404
7. Schniepp, H. C.; Li, J. L.; McAllister, M. J.; Sai, H.; Herrera-Alonso, M.; Adamson, D. H.; Prud'homme, R. K.; Car, R.; Saville, D. A.; Aksay, I. A. *J. Phys. Chem. B* **2006**, *110*, 8535 – 8539
8. Zhu, Y.; Stoller, M. D.; Cai, W.; Velamakanni, A.; Piner, R. D.; Chen, D.; Ruoff, R. S. *ACS Nano,* **2010**, *4*, 1227 – 1233
9. Muszynski, R.; Seger, B.; Kamat, P. V. *J. Phys. Chem. C,* **2008**, *112*, 5263 – 5266
10. Li, D.; Muller, M. B.; Gilje, S.; Kaner, R. B.; Wallace, G. G. *Nature Nanotech.* **2008**, *3*, 101 – 105
11. Williams, G.; Serger, B.; Kamat, P. V. TiO_2-Graphene Nanocomposites. *ACS Nano* **2008**, *2*, 1487 – 1491

12. Xu, Y.; Bai, H.; Lu, G.; Li, C.; Shi, G. J. *J. Am. Chem. Soc.* **2008**, *130*, 5856 – 5857

13. Si, Y.; Samulski, E. T. Synthesis of Water Soluble Graphene *Nano Lett.* **2008**, *8*, 1679 – 1682

14. Tung, V. C.; Allen, M. J.; Yang, Y.; Kaner, R. B. *Nature Nanotech.* **2008**, *4* (1), 25 – 29

15. Stankovich, S.; Dikin, D. A.; Piner, R.; Kohlhaas, K. M.; Kleinhammes, A.; Jia, Y.; Wu, Y.; Nguyen, S. T.; Ruoff, R. S. *Carbon* **2007**, *45*, 1558 – 1565

16. Wang, G.; Yang, J.; Park, J.; Wang, B.; Liu, H.; Yao, J. J. *Phys. Chem. C* **2008**, *112*, 8192 – 8195

17. Villar-Rodil, S.; Paredes, J. I.; Martínez-Alonso, A.; Tascón, M. D. *J. Mater. Chem.* **2009**, *19*, 3591 – 3593

18. Park, S.; An, J.; Piner, R. D.; Jung, I.; Yang, D.; Velamakanni, A.; Nguyen, S. T.; Ruoff, R. S. *Chem. Mater.* **2008**, *20* (21), 6592 – 6594

19. Gilje, S.; Han, S.; Wang, M. S.; Wang, K. L.; Kaner, R. B. A *Nano Lett.* **2007**, *7*, 3394 – 3398

20. Gomez-Navarro, C.; Weitz, R. T.; Bittner, A. M.; Scolari, M.; Mews, A.; Burghrd, M.; Kern, K. *Nano Lett.* **2007**, *7*, 3499 – 3503

21. Stankovich, S.; Dikin, D. A.; Dommett, G. H. B.; Kohlhaas, K. M.; Zimney, E. J.; Stach, E. A.; Piner, R. D.; Nguyen, S. T.; Ruoff, R. S. *Nature* **2006**, *442* (7100), 282 – 286

22. Watcharotone, S.; Dikin, D. A.; Stankovich, S.; Piner, R.; Jung, I.; Dommett, G. H. B.; Evmenenko, G.; Wu, S. E.; Chen, S. F.; Liu, C. P.; Nguyen, S. T.; Ruoff, R. S. *Nano Lett.* **2007**, *7* (7), 1888 – 1892

23. Chen, H.; Muller, M. B.; Gilmore, K. J.; Wallace, G. G.; Li, D. *Adv. Mater.* **2008**, *20*, 3557 – 3561

24. Arsat, R.; Breedon, M.; Shafiei, M.; Spizziri, P. G.; Gilje, S.; Kaner, R. B.; Kalantar-zadeh, K.; Wlodarski, W. *Chem. Phys. Lett.* **2008**, *467* (4-6), 344 – 347

25. Stoller, M. D.; Park, S.; Zhu, Y.; An, J.; Ruoff, R. S. *Nano Lett.* **2008**, *8* (10), 3498 -3502

26. Cote, L. J.; Kim, F.; Huang, J. *J. Am. Chem. Soc.* **2009**, *131* (3), 1043 – 1049

27. Eda, G.; Lin, Y. Y.; Miller, S.; Chen, C. W.; Su, W. F.; Chhowalla, M *Appl. Phys. Lett.* **2008**, *92*, 233305

28. Wang, X.; Zhi, L.; Tsao, N.; Tomovic, Z.; Li, J.; Muller, K. *Angew. Chem. Int. Ed.* **2008**, *47*, 16, 2990 – 2992

29. Wu, J.; Becerril, H. A.; Bao, Z.; Liu, Z.; Chen, Y.; Peumans, P. *Appl. Phys. Lett.* **2008**, *92*, 263302

30. Eda, G.; Fanchini, G.; Chhowalla, M.; *Nature Nanotech.* **2008**, *3*, 270-274

31. Li, X. L.; Zhang, G.; Bai, X.; Sun, X.; Wang, X.; Wang, E.; Dai, H. *Nature Nanotech.* **2008**, *3*, 538-542

32. Li, J. L.; Kudin, K. N.; McAllister, M. J.; Prud'homme, R. K.; Aksay, I. A.; Car, R. *Phys. Rev. Lett.* **2006**, *96*, 176101

33. Ramanathan, T.; Abdala, A. A.; Stankovich, S.; Dikin, D. A.; Herrera-Alonso, M.; Piner, R. D.; Adamson, D. H.; Schniepp, H. C.; Chen, X.; Ruoff, R. S.; Nguyen, S. T.; Aksay, I. A.; Prud'homme, R. K.; Brinson, L. C. *Nature Nanotech.* **2008**, *3* (6), 327 – 331

34. Stankovich, S.; Piner, R. D.; Nguyen, S. T.; Ruoff, R. S. *Carbon* **2006**, ***44***, 3342

35. Liu, Z. -H.; Wang, Z. -M.; Yang X.; Ooi, K. *Langmuir* **2002**, ***18*****,** 4926 – 4932.

36. Park, S.; An, J.; Jung, I.; Piner, R. D.; An, S. J.; Li, X.; Velamakanni, A.; Ruoff, R. S. *Nano Lett.* **2009**, *9*, 4, 1593 – 1597

37. Liang, Y.; Wu, D.; Feng, X.; Mullen, K. *Adv. Mater.* **2009**, *21*, 1679 – 1683

38. Schmidt, W. *Hydrazine and Its Derivatives: Preparation, Properties, Applications*; Wiley-Interscience: New York, **2001**; Vol. 1, Chapter 4

39. Cai, M. F.; Smart, R. B.; *Energy & Fuels,* **1993**, *7*, 52 – 56

40. White, C. M.; Rohar, P. C.; Veloski, G. A.; Anderson, R. R. *Energy and Fuels,* **1997, *11*,** 1105 – 1106

41. Industry calculation reported by Nanocomp INC. Taken from an interview with Nanocomp Inc. CEO, Peter Antoinette: http://nextbigfuture.com/2009/04/interview-with-peter-antoinette.html

42. Ponzio, E. A.; Echevarria, R.; Morales, G. M.; Barbero, C. *Polym. Int.,* **2001**, *50*, 11, **1180**

43. Hernandez, Y.; Nicolosi, V.; Lotya, M.; Blighe, F. M.; Sun, Z.; De, S.; McGovern, I. T.; Holland, B.; Byrne, M.; Gun'Ko, Y. K.; Boland, J. J.; Niraj, P.; Duesberg, G.; Krishnamurthy, S.; Goodhue, R.; Hutchison, J.; Scardaci, V.; Ferrari, A. C.; Coleman, J. N. *Nature Nanotech*. **2008,** *3*, 9, 563 – 568

44. Novoselov, K. S.; Geim, A. K.; Morozov, S. V.; Jiang, D.; Zhang, Y.; Dubonos, S. V.; Grigorieva, I. V.; Firsov, A. A. *Science,* **2004**, *306*, 666 – 669

45. Dikin, D. A.; Stankovich, S.; Zimney, E. J.; Piner, R.; Dommett, G. H. B.; Evmenenko, G.; Nguyen, S. T.; Ruoff, R. S. *Nature,* **2007**, *448*, 457 – 460

46. Park, S.; Lee, K.-S.; Bozoklu, G.; Cai, W.; Nguyen, S. T.; Ruoff, R. S. *ACS Nano,* **2008**, *2*, 572 – 578

47. Buchsteiner, A.; Lerf, A.; Pieper, J. Water Dynamics in Graphite Oxide Investigated with Neutron Scattering *J. Phys. Chem. B*. **2006**, *110*, 22328

48. Lerf, A.; Buchsteiner, A.; Pieper, J.; Schottl, S.; Dekany, I.; Szabo, T.; Boehm, H. P. Hydration behavior and dynamics of water molecules in graphite oxide *J. Phys. Chem. Solids,* **2006**, *67*, 1106 – 1110

49. Yang, D.; Velamakanni, A.; Bozoklu, G.; Park, S.; Piner, R. D.; Stankovich, S.; Jung, I.; Field, D. A.; Ventrice, J. C. A.; Ruoff, R. S. *Carbon,* **2009**, *47*, 145 – 152

Chapter 4

A Conductometric Sensor Based on Graphene with Pd Nanoparticles

4.1 Introduction

Graphene is the name given to a monolayer of sp^2-bonded carbon atoms that tightly pack into a two-dimensional lattice[1-3], and is a basic building block for other graphitic materials such as carbon nanotubes and fullerenes.[4] Because of its single-atom-thick structure, graphene possesses a zero electronic bandgap and exhibits exceptional charge carrier mobility at room temperature.[2] Since graphene demonstrates excellent ballistic transport properties, it can be utilized as the conducting channels in FET devices.[2] As a result, one of the current research interests in graphene is the potential to replace silicon-based integrated circuit (IC) technology which is rapidly approaching its theoretical limits, with graphene based ICs.[3] In addition, graphene has also been used in the development of chemical, mass, and bio-sensors[4-9], with demonstrated sensitivity to gas species including: nitrogen dioxide[4-6, 10], nitrogen monoxide[6], ammonia[4,6], hydrogen[4,8], carbon dioxide[6], carbon monoxide[6, 8, 11], nitrogen[7] and oxygen[6, 7].

However, methodologies that can enhance graphene's reactivity are still needed to achieve higher sensing performance and the commercialization of such devices.

According to a study of hydrogen chemisorption on sp^2-bonded carbon surfaces that was conducted by Ruffieux, et al.[12], the chemical binding of hydrogen to an sp^2-bonded carbon network requires a local re-hybridization from sp^2 to sp^3 that has a large adsorption energy barrier. Such an energy barrier can be lowered by the formation of surface defects and curvatures[12]. The surface defects can be induced by attaching metal catalysts which also enhance the reactivity of the material[13]. Such a mechanism has been demonstrated by an improvement in nitrogen doped carbon nanotube sensors using Pt/Ni metal composites.[13]

In this work, Pd nanoparticles are deposited on graphene sheets to enhance their sensing performance towards hydrogen. Sheets of graphene were obtained through hydrazine reduction of graphene oxide and subsequently deposited onto interdigitated transducers (IDTs); Pd nanocomposites were prepared by drop-casting ethanol/Pd(0) nanoparticles from solution and drying under vacuum. The material is characterized by transmission electron microscopy (TEM), scanning electron microscopy (SEM), X-ray diffraction (XRD) and Raman spectroscopy. The developed sensors are tested towards different concentrations of hydrogen gas. The sensing performance of the graphene/Pd devices are compared with graphene devices.

4.2 Experimental

4.2.1 Material Synthesis

Graphite oxide (GO) was prepared from graphite powder via a modified Hummer's method as reported previously.[3] Reduction of GO was performed in anhydrous hydrazine, according to a previously published procedure.[4] The quartz substrates were transferred into the drybox and spin-coated with prepared graphene dispersions at 1500 rpm for 30 seconds. After the deposition, the films were dried under vacuum for 24 hours to remove residual hydrazine.

For the preparation of Pd(0) nanoparticles, 6 mg of palladium chloride ($PdCl_2$) was dissolved in 20 ml of 95% ethanol and stirred for 24 hours to achieve a yellow-colored solution. A Beckman-Coulter Allegra® X-15R was used at 4500 rpm for 30 min for centrifugation of the solution, saving the supernatant. Using a 20 ml scintillation vial, 3 ml of the supernatant $PdCl_2$ solution was diluted to 6 ml with Milli-Q water and cooled in an ice bath. The solution was then heated in an oil bath at 90 °C for 1 hour, followed by reaction quenching immediately thereafter by cooling the vial in an ice bath. Finally, the dispersion was diluted to 1/5 by a water-ethanol mixture (95% ethanol:water = 1:1 in volume) and kept at -2 °C until needed. Graphene/Pd(0) nanocomposites were prepared by drop-casting Pd(0) solution onto the graphene covered substrates and drying the composites under vacuum.

4.2.2 Materials Characterization

TEM images were taken using a Philips CM120 under 120 kV accelerating voltage. The Pd(0) nanoparticle samples were imaged on carbon film coated Cu TEM grids. Graphene and graphene/Pd(0) composites were imaged using silicon dioxide/monoxide film covered Cu TEM grids in the glove-box followed by evacuation over 24 hours to remove residual hydrazine. As shown in Figure 4.1, most of the Pd nanoparticle bundles are observed at the locations with wrinkles or defects.

XRD characterization was performed using a 100-fold scale-up of the synthesis procedure. The Pd(0) nanoparticle dispersion was dried to yield gray powder and characterized on a zero background silicon substrate in a Crystal Logic diffractometer with Ni-filtered Cu Kα radiation (λ = 1.5418 Å). The obtained pattern of the Pd(0) nanoparticles (Figure 4.2) exhibits an excellent match with a reference Pd pattern, represented by the blue lines at 2θ = 40°, 47°, 68°, 82° and 86°. An impurity peak is also found at 2θ = 16°, this impurity is believed to be caused by the scaling-up of the synthesis procedure since the dispersion experienced less time at the necessary temperature and therefore not all of the palladium chloride was reduced.

Figure 4.3 illustrates the SEM images for graphene/Pd nanocomposites that were deposited on the surface of the device. Similar to the images taken by TEM, bundles of Pd nanoparticles, which were formed after the deposition of the material, were observed on the surface of the graphene.

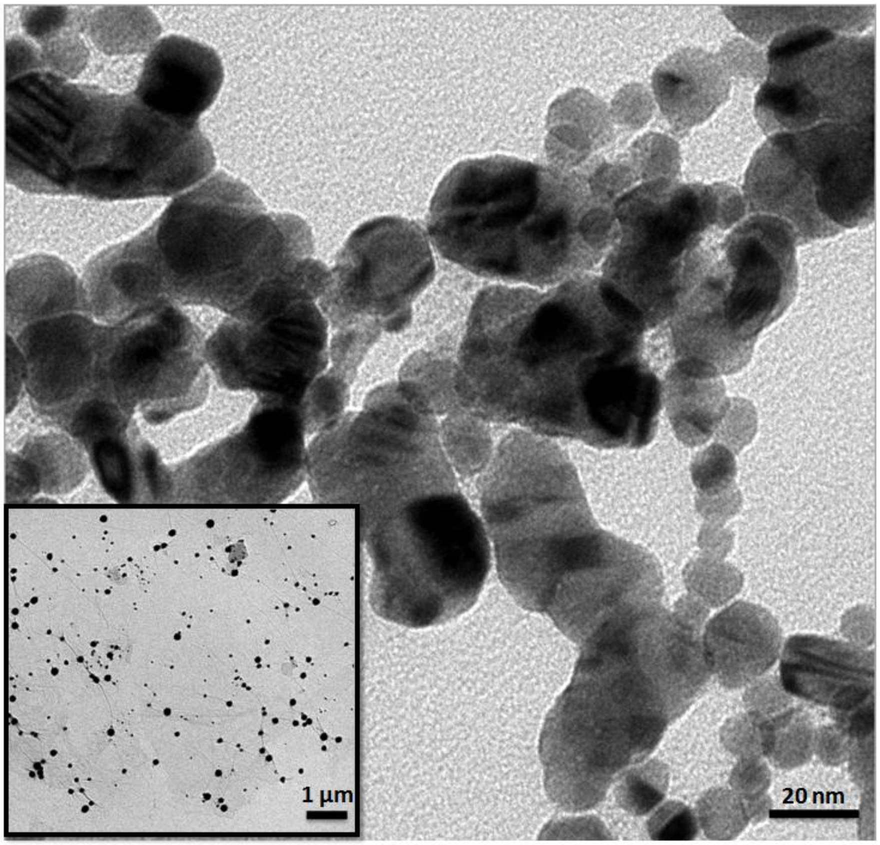

Figure 4.5 TEM image of Pd nanoparticles with an average size of 37 nm. The insert shows a TEM image of Pd nanoparticles in bundles on top of a sheet of graphene.

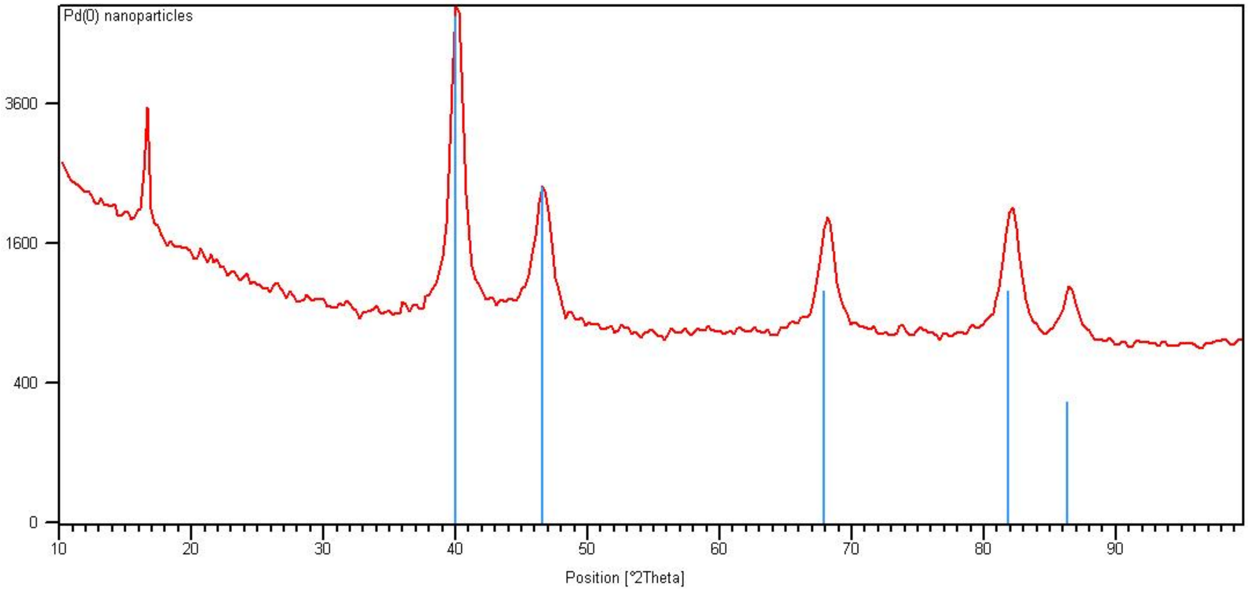

Figure 4.6 An XRD pattern of Pd(0) nanoparticles that matches up well with a reference Pd pattern (blue lines). A small peak at 16° 2θ is due to a small impurity of the precursor material.

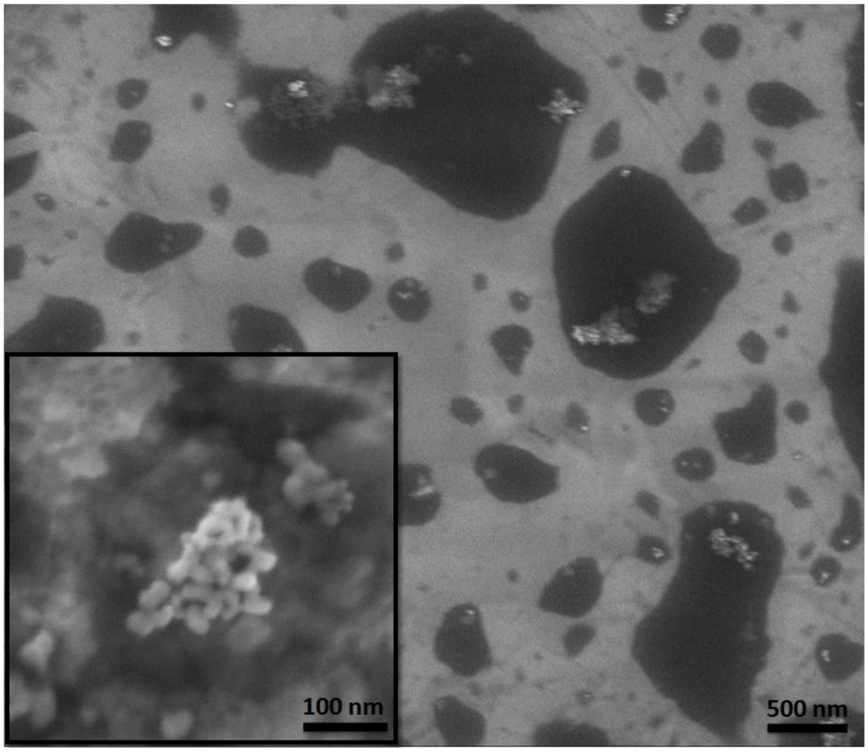

Figure 4.3 SEM images for graphene sheets with Pd nanoparticles taken on the surface of a sensing device. The insert illustrates aggregated Pd nanoparticles on graphene surfaces.

4.2.3 Sensor Testing

The designed IDT consists of four pairs of finger-like metallic electrodes (50 nm Cr and 100 nm Au) with a spacing of 180 μm from each other. The IDTs were patterned onto quartz substrates using standard photolithography procedures followed by chemical etching. After graphene and graphene/Pd were deposited onto the IDTs, the devices were bonded with wires and settled for gas sensing testing. A mass flow controlling system was employed to mix H_2 gas (1%, balanced with synthetic air) and pure synthetic air to achieve different concentrations of H_2 in the gas chamber. A multimeter was utilized to record the real time variation of the device resistances as a function of the sensors' responses.

4.3 Results and Discussions

In Figure 4.3 the Raman spectra of graphene sheets and graphene/Pd are presented. Both spectra are dominated by a D band at approximately 1350 cm^{-1} and a G band at approximately 1600 cm^{-1}. In addition, the 2D band and D + G combination mode are also observed at approximately 2700 and 2950 cm^{-1}, respectively. Such a Raman fingerprint indicates that the sample is a combination of graphene and graphite oxide.[8, 14]

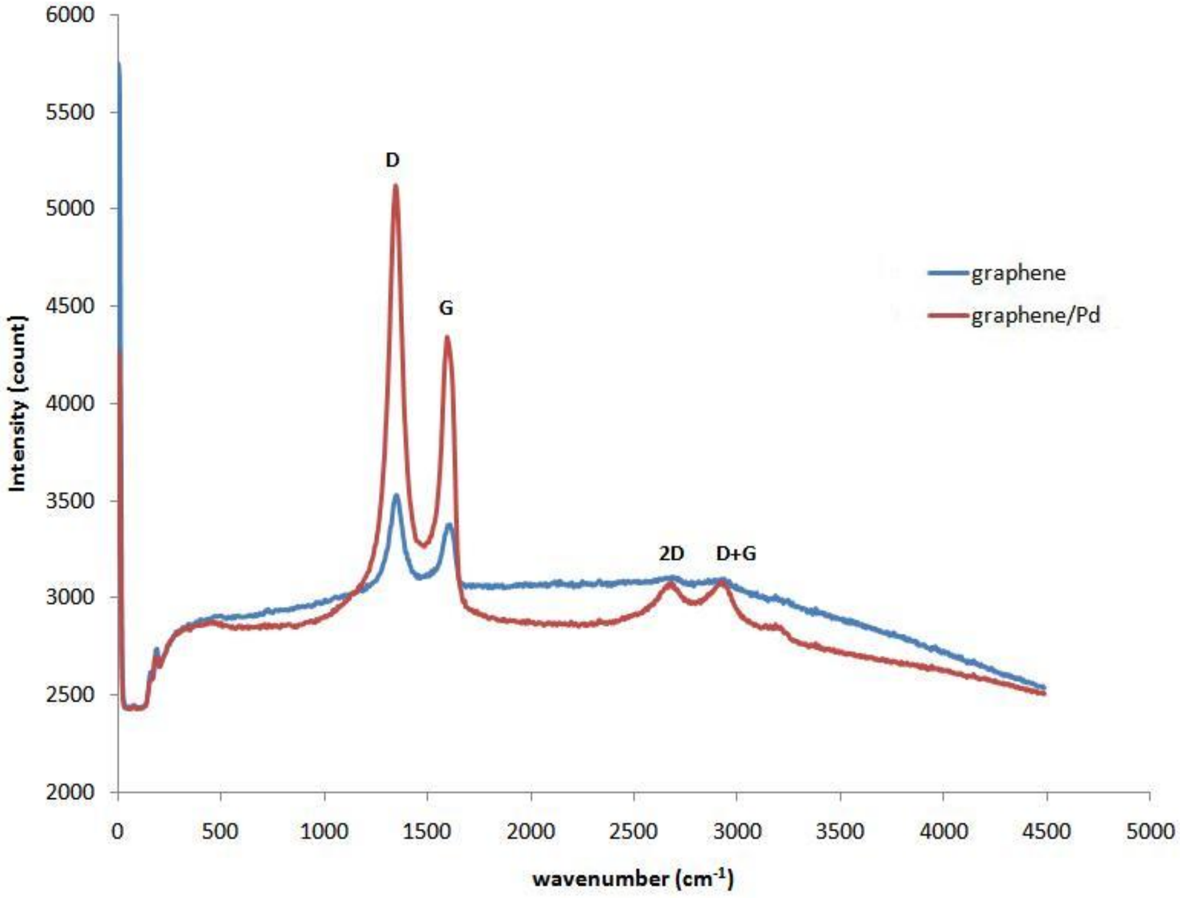

Figure 4.7 Raman spectra of graphene sheet(s) with (red) and without (blue) Pd nanoparticles deposited on conductometric devices obtained using 532 nm laser excitation.

It is evident that Pd nanoparticles enhance the surface Raman scattering of graphene sheets since more counts are received at the spectrum peaks in the presence of Pd nanoparticles. The surface enhanced Raman scattering (SERS) effect is known to occur on surfaces with high roughness and metallic nanostructures.[15, 16] The SERS effect caused by metallic nanoparticles can be explained by either charge transfer theory (an enhancement ratio of ~10^2) and/or localized electric field enhancement theory (an enhancement ratio of ~10^4). [17, 18]

An enhancement of the localized electric field is generally induced by surface plasmon resonance which occurs when the metal has a small real part in its complex permittivity.[16] For metals such as Pd, the real part of its complex permittivity is small, but the imaginary part is too large to produce efficient enhancement.[16] Therefore, the observed SERS effect in our work, which has an enhancement ratio of approximately 5, is believed to result from the electron transfer between Pd nanoparticles and graphene sheets. Transfer of an electron from Pd nanoparticles to graphene will change the potential in the graphene structure; when the electrons tunnel back to the Pd nanoparticles, the graphene structure will in general be left in a vibrationally excited state[18] and SERS will occur.

According to the TEM analysis, the Pd nanoparticles either prefer moving to the defect sites or directly cause such defects in graphene structures. In Raman spectra, an increase of the I_D/I_G (integrated intensity ratio for the D band and G band) from ~1.05 to ~1.18 is observed when Pd nanoparticles are present (as shown in Table 4.1); this suggests that a higher level of structural disorder is induced by the Pd nanoparticles.[19] As a result, it is more likely that Pd nanoparticles have caused such defects.

Table 4.2 Peaks and their intensities of measured Raman spectra for graphene sheet(s) with and without Pd nanoparticles.

	D band *(cm^{-1})*	*Intensity* *(counts)*	*G band* *(cm^{-1})*	*Intensity* *(counts)*	*2D* *(cm^{-1})*	*Intensity* *(counts)*	*D+G* *(cm^{-1})*	*Intensity* *(counts)*	I_D/I_G
Graphene /Pd	1347	5086	1600	4297	2705	3047	2938	3067	1.183
Graphene	1357	3482	1620	3314	2705	3095	2954	3036	1.051

The dynamic responses of the graphene and graphene/Pd sensors towards different concentrations of H_2 gas are shown in Figure 4.4. The normalized device resistances for both sensors were utilized to illustrate their sensitivities, which are defined as:

$$R_{normalized} = \frac{R_{gas}}{R_{bas-line}}, \qquad \textbf{(Equation 4.1)}$$

where R_{gas} is the real time device resistance measured in gas chamber and $R_{base\text{-}line}$ is the device resistance measured when the sensor is stabilized in synthetic air. The testing was conducted at room temperature to prevent any additional oxidization of the graphene structures.

The responses indicate that the graphene sensor has a sensitivity of approximately 0.12% (resistance change) towards 0.06% H_2 gas, while the graphene/Pd sensor has a sensitivity of approximately 0.2% towards the same concentration of H_2 gas. Such an improvement of device sensitivity can be caused by a combination of two effects. First, Pd nanoparticles can induce a higher level of graphene structural disorder and surface defects, which result in a lowered adsorption energy barrier for H_2 molecules. Second, Pd nanoparticles have catalytic properties, which help dissociate hydrogen molecules into atomic hydrogen and promote surface chemisorption of hydrogen.[20]

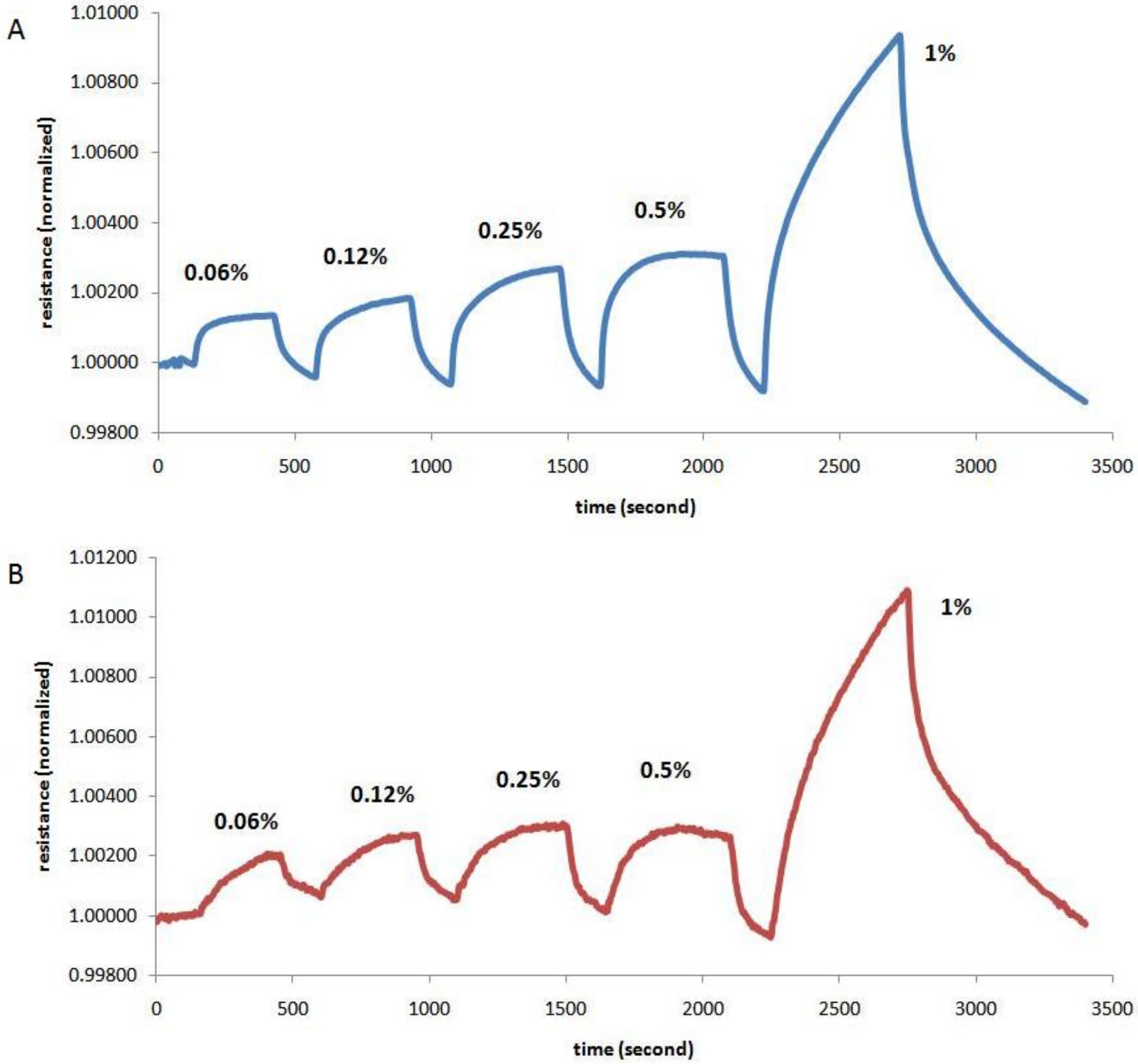

Figure 4.8 Dynamic responses (change in normalized resistance) of the developed conductometric sensors towards different concentrations of H_2 at room temperature: (A) graphene, (B) graphene/Pd. The device was placed in a computerized multi-channel gas calibration system and five pulses (0.06%, 0.12%, 0.25%, 0.5% and 1%) of H_2 gas in synthetic air were applied to the gas chamber.

4.4 Conclusions

In summary, graphene sheets with Pd nanoparticles were successfully synthesised and employed for hydrogen gas sensing. The synthesised materials were characterized using TEM, SEM, XRD and Raman spectroscopy. A surface enhanced Raman effect with an enhancement ratio of approximately 5 was observed due to the presence of the Pd nanoparticles. Since Pd has a large imaginary part in its complex permittivity and cannot produce efficient SERS, the observed SERS is believed to be caused by charge transfer between Pd nanoparticles and graphene. The Raman analysis also indicated an interaction between graphene and Pd nanoparticles as evidenced by the increased I_D/I_G ratio, suggesting an increased level of structural disorder. The sensing responses indicate that the graphene/Pd sensor has a higher sensitivity compared to the graphene sensor. Such performance improvements can be attributed to a combination of a lowered adsorption energy barrier for H_2 molecules induced by Pd nanoparticles and improvement in the surface chemisorption of hydrogen molecules due to the catalytic effect of the Pd nanoparticles.

4.5 References

1. Novoselov, K. S.; Geim, A. K.; Morozov, S. V.; Jiang, D.; Zhang, Y.; Dubonos, S. V.; Grigorieva, I. V.; Firsov, A. A. *Science,* **2004**, *306*, 666 – 669
2. Geim, A. K.; Novoselov, K. S.; *Nature Materials,* **2007***, 6*, 183 – 191
3. Gilje, S.; Han, S.; Wang, M.; Wang, K. L.; Kaner, R. B. *Nano Letters,* **2007**, *7*, 3394 – 3398
4. Fowler, J. D.; Allen, M. J.; Tung, V. C.; Yang, Y.; Kaner, R. B.; Weiller, B. H.; *ACS Nano,* **2009***, 3*, 301 – 306
5. Schedin F.; Geim, A. K.; Morozov, S. V.; Hill, E. W.; Blake, P.; Katsnelson, M. I.; Novoselov, K. S. *Nature Material,* **2007***, 6*, 652 – 655
6. Huang, B.; Li, Z. Y.; Liu, Z. R.; Zhou, G.; Hao, S. G.; Wu, J.; Gu, B. L.; Duan, W. H. *J. Phys. Chem. C,* **2008**, *112*, 13442 – 13446
7. Rangel, N. L.; Seminario, J. A. *J. Phys. Chem. A,* **2008**, *112*, 13699 – 13705
8. Arsat, R.; Breedon, M.; Shafiei, M.; Spizziri, P. G.; Gilje, S.; Kaner, R. B.; Kalantar-Zadeh, K.; Wlodarski, W. *Chem. Phys. Lett.* **2009**, *467*, 344 – 347
9. Dan, Y. P.; Lu, Y.; Kybert, N. J.; Luo, Z. T.; Johnson, A. T. C. *Nano Lett.* **2009**, *9*, 1472 – 1475
10. Lu, G. H.; Ocola, L. E.; Chen, J. H.; *Appl. Phy. Lett.* **2009**, *94,* 083111
11. Ao, Z. M.; Yang, J.; Li, S.; Jiang, Q. *Chem. Phys. Lett.* **2008**, *461*, 276 – 279
12. Ruffieux, P.; Groning, O.; Bielmann, M.; Groning, P. *Appl. Phy. a-Mat. Sci. & Proces.* **2004**, *78*, 975 – 980

13. Sadek, A.; Zhang, C.; Hu, Z.; Partridge, J.; McCulloch, D.; Wlodarski, W.; Kalantar-Zadeh, K. *Phys. Chem. C*, **2010**, *114* (1), 238 – 242

14. Stankovich, S.; Dikin, D. A.; Piner, R. D.; Kohlhaas, K. A.; Kleinhammes, A.; Jia, Y.; Wu, Y.; Nguyen, S. T.; Ruoff, R. S. *Carbon,* **2007**, *45*, 1558 – 1565

15. Dhawan, A.; Du, Y.; Yan, F.; Gerhold, M. D.; Misra, V.; Vo-Dinh, T. *IEEE Sens. J.* **2010***, 10*, 608 – 616

16. Vo-Dinh, T. *Trac-Trends in Analytical Chemistry,* **1998**, *17*, 557 – 582

17. Lombardi, J. R.; Birke, R. L.; Lu, T. H.; Xu, J. *J. Chem. Phy*. **1986***, 84*, 4174 – 4180

18. Persson, B. N. J.; Zhao, K.; Zhang, Z. Y. *Phys. Rev. Lett.* **2006**, *96,* 207401

19. Pimenta, M. A.; Dresselhaus, G.; Dresselhaus, M. S.; Cancado, L. G.; Jorio, A.; Saito, R. *Phys. Chem. Chem. Phys.* **2007**, *9*, 1276 – 1291

20. Kong, J.; Chapline, M. G.; Dai, H. J. *Adv. Mater.* **2001**, *13*, 1384 – 1386

Chapter 5

Patterning and Electronic Tuning of Laser Scribed Graphene for Flexible All-Carbon Devices

5.1 Introduction

In the pursuit of producing high-quality bulk graphene-based devices, a variety of syntheses now incorporate graphite oxide (GO) as a precursor for the generation of large-scale graphene-based materials.[1] This inexpensive method of producing large quantities of GO from the oxidation of graphitic powders, in addition to its water dispersibility, has made GO an ideal starting material. In particular, the water dispersibility of GO, which stems from the electronegative oxygen species bonded to the carbon network,[2] has led, through exfoliation, to the production of individual graphene oxide sheets.[3] Unfortunately, the same oxygen species that give GO its water-dispersible properties also create defects in its electronic structure, and as a result, GO is an electrically insulating material.[4] Therefore, the development of device grade graphene-based films with superior electronic properties requires the removal of these oxygen species, re-establishment of the conjugated carbon network, as well as a method for controllably patterning electronic device features.[5]

Methods for reducing graphite oxide have included chemical reduction *via* hydrazine, hydrazine derivatives or other reducing agents,[6-8] high-temperature annealing under chemical reducing gases and/or inert atmospheres,[9] solvothermal reduction,[10, 11] a combination of chemical and thermal reduction methods,[12] flash reduction,[13, 14] and most recently, laser reduction of GO.[15-19] Although several of these methods have demonstrated relatively high-quality reduction of graphite oxide, many have been limited by expensive equipment, high annealing temperatures, and nitrogen impurities in the final product. In addition, large-scale film patterning *via* an all-encompassing step for both reduction and patterning has proven difficult and has typically been dependent on photomasks to provide the most basic of patterns.

Therefore, an inexpensive process that does not need reducing agents and expensive equipment and is highly tunable is essential to produce high-quality graphene-based films at low cost. The technique described here not only meets these stringent requirements but also provides direct control over film conductivity and image patterning, creating flexible electronic devices in a single-step process. The simple direct fabrication of laser scribed graphene (LSG) on flexible substrates therefore simplifies the development of lightweight electronic devices. Here, an all-organic NO_2 gas sensor, a fast redox-active electrode, and a scaffold for the direct growth of platinum nanoparticles are demonstrated.

5.2 Experimental

5.2.1 Graphite Oxide Films

Graphene oxide was synthesized using a modified Hummers method[55] with dispersions of graphene oxide prepared according to the following concentrations: 3.7, 2.8, and 1.6 mg/mL. Approximately, 16 mL of the respective graphite oxide solutions was drop-cast directly onto a LightScribe-enabled CD/DVD media disk and allowed to dry for 24 h. Spin-coating was also a technique that was used to make films of GO, but depending on the substrate used and the type of experiment needed, drop-casting was typically the better choice for this work. In order to increase the hydrophilicity of the substrate surface and obtain thin uniform films, the LightScribe-enabled DVD substrates were pretreated with an oxygen plasma at 35 mW for 3 min. A thick film of polydimethylsiloxane (PDMS) was used to cover and protect the tracking strip found at the center of the DVD disk from the oxygen plasma. The graphite oxide dispersion was also drop-cast onto a thin substrate such as polyethylene terephthalate (PET), which was resized to the same dimension as the DVD and affixed onto the CD/DVD surface for laser treatment. Silver electrodes with dimensions of 1 mm × 3 mm with an inter-electrode spacing of 3 mm were deposited on the laser-reduced and non-laser-treated graphite oxide films and subsequently divided into pairs. Two-point *I–V* measurements were carried out using a standard probe station. Ten or more measurements were performed on different areas of each film to ensure reproducibility. The film thicknesses were measured on a Dektak 6 profilometer. Sheet resistance and conductivity values were calculated from two-point probe measurements and the film thicknesses.

The LSG morphology was monitored and imaged using an optical microscope (Zeiss Axiotech 100) and a scanning electron microscope (JEOL 6700, Philips XL 30). XPS spectra were recorded using a Kratos Axis Ultra DLD spectrometer. A Renishaw Raman spectrometer with an excitation wavelength of 514 nm was employed to characterize the structural changes between graphite oxide and laser scribed graphene. Sensor experiments were carried out as described by Fowler *et al*.[36]

5.2.2 Electrochemical Setup

All electrochemical experiments were performed with an electrochemical analyzer VeraSTAT3 (Princeton Applied Research, USA). A three-electrode configuration was employed for all of the measurements with a platinum foil counter electrode (6.25 cm^2, Sigma-Aldrich) and an Ag/AgCl, 3 M NaCl reference electrode (Bioanalytical Systems Inc., USA). The working electrodes used were highly reduced-laser scribed graphene (hr-LSG), graphite oxide, or graphite electrodes, all with a working surface area of 0.16 cm^2.

Each hr-LSG electrode was made by cutting a PET sheet coated with hr-LSG into rectangular pieces of the appropriate size. The ends were then lightly painted with conducting silver paint to ensure good electrical contact. Part of the electrode was then covered with polyimide (Kapton) tape so that only a working area of 0.16 cm^2 was allowed to be exposed to the electrolyte. Finally, the electrode was connected to the potentiostat with an alligator clip. Each graphite oxide electrode was prepared by a similar approach using graphite oxide coated PET. Pencil lead obtained from Pentel Co. Ltd., Japan, and named Hi-polymer Super 50-HB was purchased from a local store and used as a graphite electrode. The "lead" had a total length of 6 cm and a diameter of 0.07 cm. The electrode was prepared by renewing its surface using cellophane tape before its use. This procedure involves pressing the surface onto a cellophane tape and removing the top few layers of graphite. After repeating several times, the electrode was then cleaned in acetone to remove any adhesive. A projected surface of 0.16 cm^2 was obtained by sealing part of the electrode with Kapton tape.

5.2.3 Electron Transfer Kinetics

The redox system that was used for the evaluation of the electron transfer kinetics was 5 mM $K_3[Fe(CN)_6]/K_4[Fe(CN)_6]$ (1:1 molar ratio) dissolved in 1.0 M KCl solution. To ensure a stable electrochemical response, the electrodes were first cycled for at least five scans before collecting the experimental data. The heterogeneous electron transfer rate constant ($k_{\mathrm{obs}}{}^{0}$) was determined using a method developed by Nicholson, which relates the peak separation (ΔE_P) to a dimensionless kinetic parameter, ψ, and consequently to $k_{\mathrm{obs}}{}^{0}$ according to the following equation:[48]

$$k_{\mathrm{obs}}^{0} = \psi\left[\sqrt{D_0 \pi \nu \left(\frac{nF}{RT}\right)}\right]\left(\frac{D_R}{D_O}\right)^{\alpha/2}$$

Equation 5.1

where D_{O} and D_R are the diffusion coefficients of the oxidized and reduced species, respectively. The other variables include ν, the applied scan rate; n, the number of electrons transferred in the reaction; F, the Faraday constant; R, the gas constant; T, the absolute temperature; and α, the transfer coefficient. The diffusion coefficients of the oxidized and reduced species are typically similar; therefore, the term $(D_R/D_O)^{\alpha/2} \sim 1$. A diffusion coefficient (D_O) of 7.26×10^{-6} cm^2 s^{-1} was used for $[Fe(CN)_6]^{3-/4-}$ in 1.0 M KCl.[57]

5.2.4 Synthesis of Platinum Nanoparticles/hr-LSG Composites

Electrodeposition of Pt nanoparticles on hr-LSG electrodes was performed in a three-electrode cell (described above) containing 1.0 mM K_2PtCl_6 in 0.5 M H_2SO_4 at a constant potential of −0.25 V. To control the amount and size of the Pt nanoparticles, the deposition was carried out for different periods of time.

5.3 Results and Discussions

5.3.1 Formation of hr-LSG Using LightScribe Drive

Here we show that LightScribe patterning technology can be used as an effective tool for solid-state patterning and generation of laser scribed graphene. LightScribe is a commercially available program that is used in conjunction with a DVD optical drive unit to pattern images on any LightScribe-enabled CD/DVD disk.[20] The program controls the 788 nm infrared laser (maximum power output = 5 mW) inside an optical drive unit by periodically pulsing an objective lens assembly, causing the laser to focus and defocus on an infrared active dye matrix found on the top side of a LightScribe-enabled CD/DVD disk. In order to control the objective lens pulsing mechanism and hence the laser intensity, the LightScribe program uses a computerized grayscale to generate different levels of contrast in the resulting pattern. Thus by focusing the laser on a specific area of the dye matrix, it is possible to selectively pattern complex images.[20] Here we bypass the original dye matrix by depositing a thin layer of graphite oxide on top of a DVD disk prior to the patterning process and use the LightScribe program to effectively and controllably reduce and pattern graphite oxide films.

As an illustration of the diversity in image patterning that is possible, a complex image formed by the direct laser reduction of graphite oxide is shown in Figure 5.1. An elaborate image of a man's head with circuits (Figure 5.1a) is directly patterned on a film of graphite oxide (Figure 5.1b). Essentially, any part of the graphite oxide film that comes in direct contact with the 788 nm infrared laser is effectively reduced, with the amount of reduction being controlled by the laser intensity, a factor that is determined by the degree of laser focus and/or pulsing of the objective lens assembly unit. The resulting image is an effective print of the original image, but it is set in a series of gray and black colors, which is directly related to the laser intensities that are used to generate the image. As expected, the darkest black areas indicate exposure to the strongest laser intensities, while the lighter gray areas are only partially reduced. Since different grayscale colors directly correlate with the laser's intensity, it is possible to tune the electrical properties of the generated LSG over 5 orders of magnitude in sheet resistance (Ω/sq) by simply changing the grayscale color used during the patterning process. In fact, there is a clear relationship between sheet resistance, grayscale color, and the number of times the graphite oxide film is laser irradiated, as illustrated in Figure 5.1c. Control over conductivity from a completely insulating graphite oxide film, with typical sheet resistance values of >20 MΩ/sq to a conducting highly reduced laser scribed graphene (hr-LSG) registering a sheet resistance value of approximately 80 Ω/sq, which translates to a conductivity of ~1650 S/m, is possible. This method is sensitive enough to differentiate between visibly similar grayscale colors, as shown in the graph, with the sheet resistance varying significantly with only a small change in grayscale. In addition, the number of times a film is laser-treated results in a significant and controllable change in sheet resistance. Each additional laser treatment lowers the sheet resistance, as seen in Figure 5.1c, where a film is laser-reduced once (black squares), twice (red circles), and three times (blue triangles) with respect to the grayscale. Therefore, the film's sheet resistance is tunable by controlling both the grayscale color used and the number of times the film is reduced by the laser, a property that has so far been difficult to control through other methods.

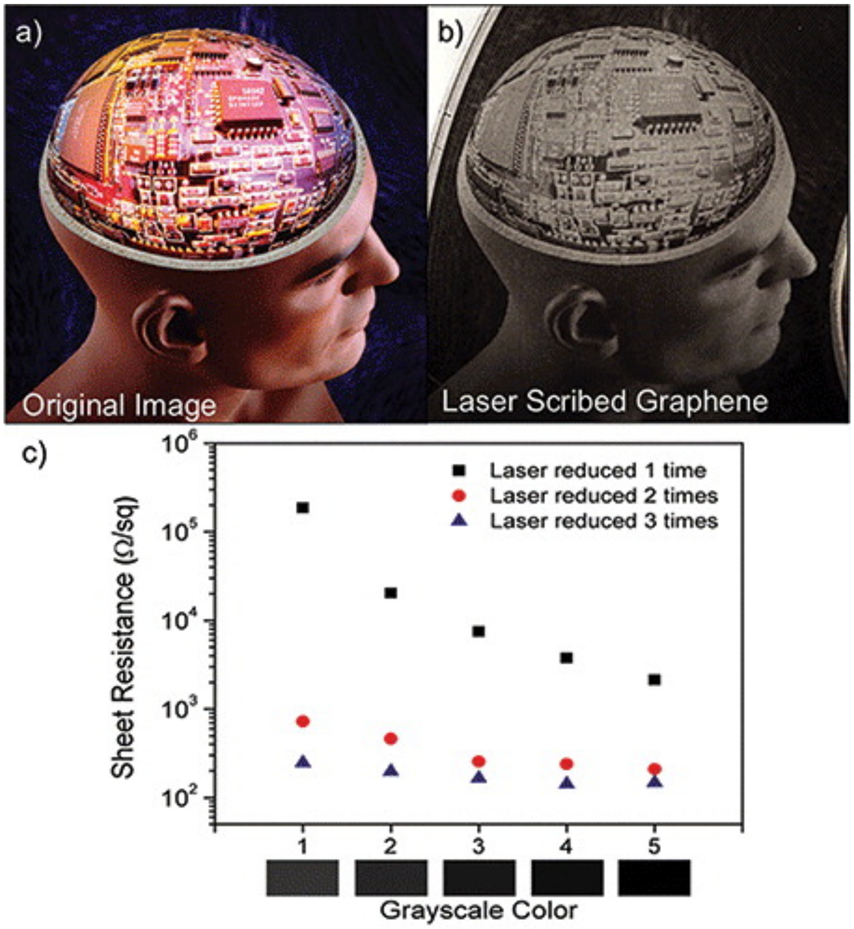

Figure 5.1 Comparison between (a) a standard complex colored image of a man's head filled with circuits and (b) the same image reproduced by reducing graphite oxide at various levels, which corresponds to a change in electrical properties (Copyright Lester Lefkowitz). A correlation between laser intensity and sheet resistance is shown in (c) where the sheet resistance of LSG is controlled in two ways, by printing in grayscale color and/or by controlling the number of times the film is irradiated with the 788 nm infrared laser. The log base graph clearly shows the sheet resistance decreasing by orders of magnitude when different grayscale colors are used, which is directly related to the laser intensity. In addition, the number of times the graphite oxide film is irradiated with that specific grayscale color, for example, laser reduced once (black squares), twice (red dots), or three time (blue triangles), also produces a significant decrease in sheet resistance, which provides a second mode of controlling the electrical properties of LSG.

5.3.2 hr-LSG Magnified

Scanning electron microscopy (SEM) is used to understand the effects a low energy infrared laser has on the structural properties of GO film by comparing the morphological differences between highly reduced laser scribed graphene and un-treated graphite oxide film. Figure 5.2a illustrates the infrared laser 's effect on graphite oxide film; prior to laser treatment, the GO film appears flat (right side of image) in contrast to the aligned, stacked laser reduced graphite oxide that occurs immediately after contact with the infrared laser (left-side of image). The image not only gives a clear definition between laser scribed graphene and un-treated GO regions, but also demonstrates the level of precision possible when using this method as a means to pattern and reduce graphite oxide. The regions of stacked and reduced graphitic carbon, which result from the laser treatment, can be further analyzed through cross-sectional SEM. The cross-sectional view shown in Figure 5.2b is of a freestanding film of laser treated and un-treated GO, which shows a significant difference between film thicknesses. In fact, laser scribed graphene increases in thickness by approximately 10 times that of un-treated GO film, as indicated by the blue brackets in Figure 5.2b. The increased thickness stems from rapid degassing of gases generated and released during laser treatment, similar to thermal shock, which effectively cause the reduced graphite oxide's expansion and exfoliation as these gases rapidly pass through the film. In addition, the film does not suffer any detrimental effects even after several irradiation cycles, and the film thickness remains consistent and stable even after several months in ambient conditions. Figure 5.2c is a cross-sectional image of a single laser scribed graphene stack, which clearly shows a porous and expanded structure. By magnifying a selected area within the stacked region in Figure 5 . 2c, the thickness of the expanded sheets can be calculated to be between 5-10 nm (Figure 5.2d).

Additionally, transmission electron microscopy (TEM) was taken of the expanded and exfoliated laser scribed graphene film in order to fully characterize the film. As is clearly visible by the highly transparent sheet shown in Figure 5.3, the laser irradiation of graphite oxide results in the generation of large thin sheets of few-layer laser scribed graphene, which is consistent with SEM analysis. Although irradiation from an infrared laser is only marginally absorbed by graphite oxide, with enough power and focus, it can cause sufficient thermal energy to efficiently reduce, deoxygenate, expand, and exfoliate a graphite oxide film.

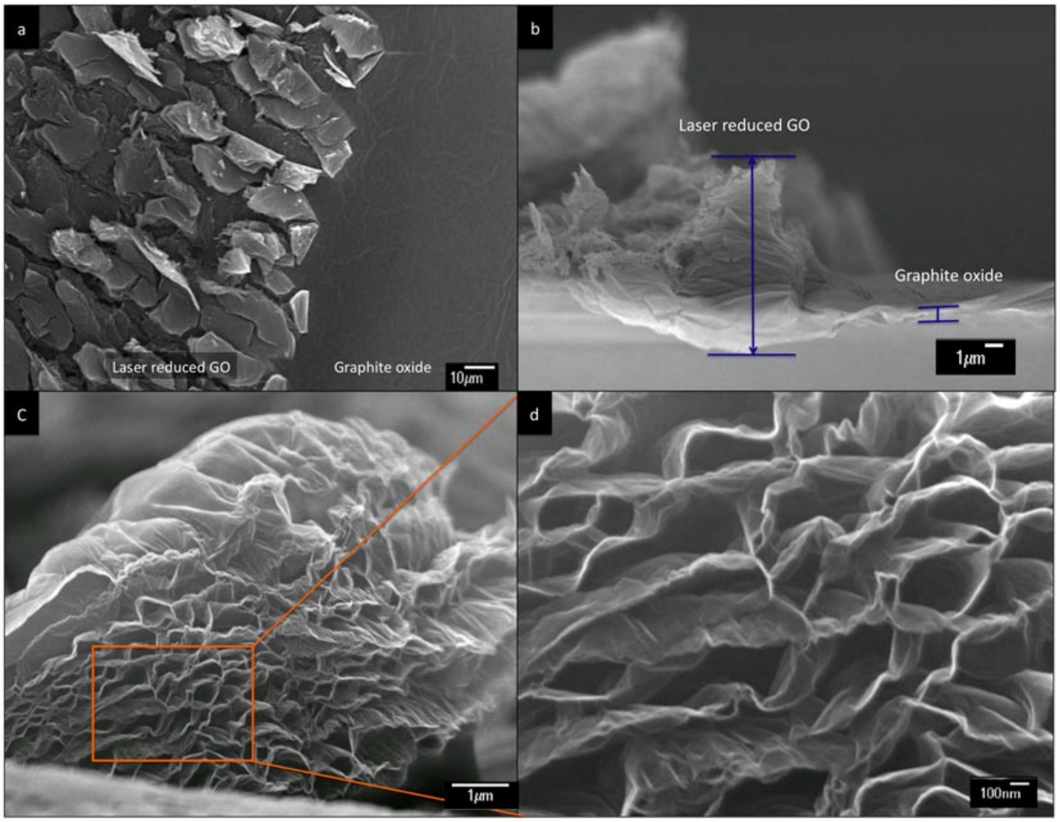

Figure 5.2 Scanning electron microscope (SEM) images of laser scribed graphene (LSG). a) Top-view of GO before laser treatment (right) and after laser treating (left). Laser treating GO film results in large domains of stacked laser scribed graphene. b) Cross-sectional view of a freestanding film, which compares the expanded and exfoliated laser scribe graphene film with that of graphite oxide film. An increase in film thickness is clearly visible for laser scribed graphene. c) A higher magnification cross-sectional view. d) Selective area magnification of LSG demonstrating the large open network, which results from the laser reduction process.

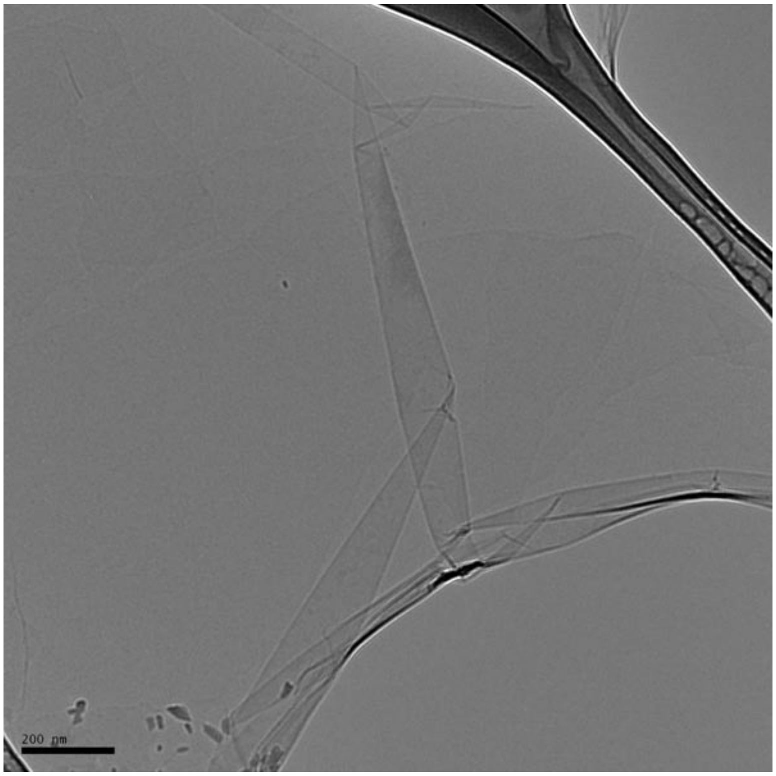

Figure 5.3 A transmission electron microscope (TEM) image of few layer laser scribed graphene deposited on lacy carbon TEM grids. Scale bar = 200 n

5.3.3 Raman, XRD and XPS Analysis

Raman spectroscopy was used to characterize and compare the structural changes induced by laser treating graphite oxide. As can be seen in Figure 5.4a, characteristic D, G, 2D, and 3S peaks are observed in both graphite oxide and highly reduced laser scribed graphene (hr-LSG). The presence of the D band in both spectra suggests that carbon sp^3 centers still exist after reduction.[6] The LSG spectrum shows a slight increase in the D band peak at ~1350 cm^{-1}; this unexpected increase is due to a larger presence of structural edge defects and indicates an overall increase in the amount of smaller graphene domains.[21] The result is consistent with SEM analysis, where the generation of exfoliated accordion-like graphitic regions (Figure 5.2) caused by the laser treatment creates a large amount of edges.[22, 23] However, the D band also shows a significant overall peak narrowing, suggesting a decrease in the types of defects in the laser scribed graphene. The G band experiences a narrowing and a decrease in peak intensity as well as a peak shift from 1585 to 1579 cm^{-1}. These results are consistent with the re-establishment of sp^2 carbons and a decrease in structural defects within the basal planes.[24, 25] The overall changes in the G band indicate a transition from an amorphous carbon state to a more crystalline carbon state. In addition, a prominent and shifted 2D peak from 2730 to 2688 cm^{-1} is seen after GO is treated with the infrared laser, indicating a considerable reduction of the GO film and strongly points to the presence of few layer graphene.[26, 27] Finally, as a result of lattice disorder, the combination of D–G generates an S3 second-order peak, which appears at ~2927 cm^{-1} and, as expected, diminishes with decreasing disorder after infrared laser treatment.[28] The Raman analysis demonstrates the effectiveness of treating graphite oxide with an infrared laser as a means to effectively and controllably produce few-layer hr-LSG.

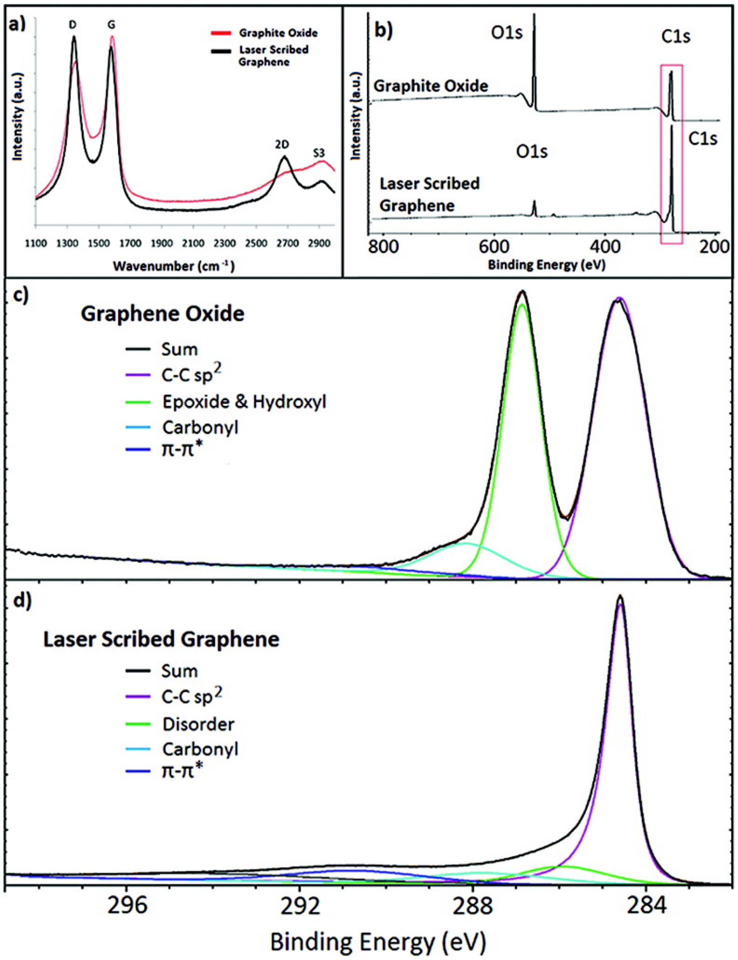

Figure 5.4 Raman and XPS comparisons between GO and hr-LSG. (a) Raman showing graphite oxide (solid red line) exhibiting typical D, G, and amorphous 2D bands. The LSG (solid black line) spectrum shows an increase in the D band due to an increase in edge planes after laser irradiation as well as a shifted and diminished G band as a result of the enhanced crystallinity of the LSG. The shift and presence of the 2D band indicates the synthesis of few-layer graphene. (b) Overview of the XPS spectra confirms the decrease in the ratio of oxygen to carbon as a result of laser irradiation of the graphite oxide film. By taking a closer look at the boxed area, it is possible to compare the carbon–oxygen functionalities of (c) graphite oxide and (d) laser scribed graphene. In contrast to graphite oxide, the LSG film shows a significant loss of C–O functionalities, an increase in sp^2 carbons, and a significant increase in the π to π* satellite peak.

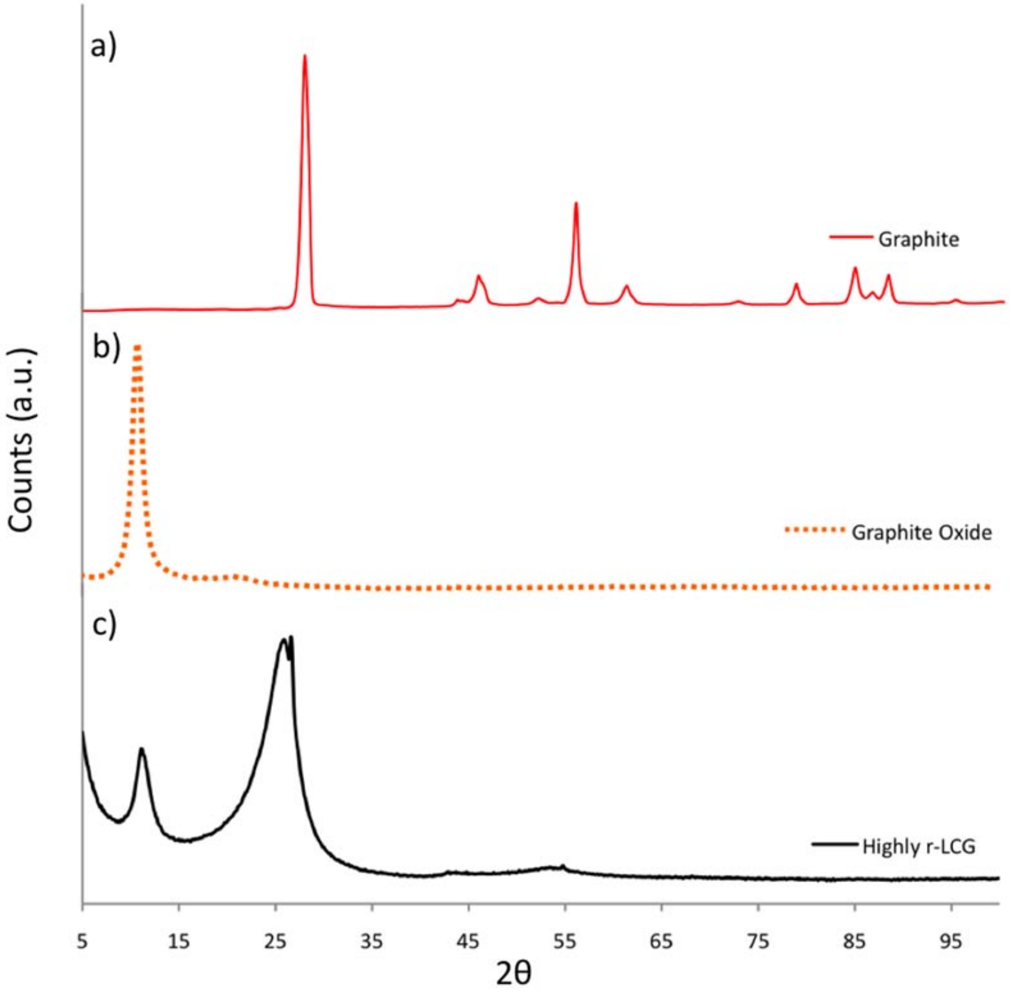

Figure 5.5 Powder X-ray Diffraction pattern of a) graphite, b) graphite oxide, and c) highly reduced laser scribed graphene.

A powder X-ray diffraction (XRD) pattern of highly reduced laser scribed graphene is compared to both graphite and graphite oxide diffraction patterns (Figure 5.5). A typical XRD pattern for graphite, shown in Figure 5.5a, displays the characteristic peak of $2\theta = 27.8°$ with a d-spacing of 3.20 Å. An XRD pattern for graphite oxide, on the other hand, exhibits a single peak at $2\theta = 10.76°$, which corresponds to an interlayer d-spacing of 8.22 Å (Figure 5.5b). The increased d-spacing in graphite oxide is due to the oxygen containing functional groups in graphene oxide sheets, which trap water molecules between the basal planes and the sheets which then expand and separate.[29-32] The XRD pattern of hr-LSG shows the presence of both GO (10.76° 2θ) and a broad graphitic peak at 25.97° 2θ associated with a d-spacing of 3.43 Å (Figure 5.5c). The GO presence in LSG is expected since the laser has an optimum penetration depth, which will result in the reduction of only the top portion of the film with the bottom layer being unaffected by the laser. The small presence of GO is more prominent in thicker films, but begins to diminish in thinner films. In addition, one can also observe a partially obstructed peak at 26.66° 2θ, which shows a similar intensity to the broad 25.97° 2θ peak. Both of these peaks, considered graphitic peaks, and are associated with two different lattice spacing between basal planes.

X-ray photoelectron spectroscopy (XPS) was employed to correlate the effects of laser irradiation on the oxygen functionalities and to monitor the structural changes in the GO film. Comparing the carbon to oxygen (C/O) ratios between graphite oxide and highly reduced laser scribed graphene provides an effective measurement of the extent of reduction achieved using a simple low-energy infrared laser. Figure 5.2b illustrates the significant disparity between the C/O ratios before and after laser treatment of the graphite oxide films. Prior to laser reduction, typical graphite oxide films have a C/O ratio of approximately 2.6, corresponding to a carbon/oxygen content of ~ 72 and 38%. On the other hand, the hr-LSG has an enhanced carbon content of 96.5% and a diminished oxygen content of 3.5%, giving an overall C/O ratio of 27.8. Since the laser reduction process takes place under ambient conditions, it is postulated that some of the oxygen present in the hr-LSG film is a result of the film having a static interaction with oxygen found in the environment.

The C1s XPS spectrum of GO displays two broad peaks (Figure 5.2c), which can be resolved into three different carbon components corresponding to the functional groups typically found on the GO surface, in addition to a small π to π* peak at 290.4 eV.[21] These functional groups include carboxyl, sp^3 carbons in the form of epoxide, and hydroxyl carbons, which are associated with the following binding energies: approximately 288.1, 286.8, and 284.6 eV, respectively.[33, 34] As expected, the large degree of oxidation in graphite oxide results in the various oxygen components in the GO C1s XPS spectrum, in contrast to the highly reduced laser scribed graphene spectrum, which shows a significant decrease in oxygen-containing functional groups and an overall increase in the C–C sp^2 carbon peak (Figure 5.2d). This points to an efficient deoxygenation process as well as the re-establishment of C═C bonds in the carbon network. These results are consistent with the Raman analysis. Thus the infrared laser is powerful enough to remove a majority of the oxygen functional groups, as is evident in the LSG XPS spectrum, which only shows a small disorder peak and a peak at 287.6 eV. The latter corresponds to the presence of sp^3-type carbons, suggesting that a small amount of carboxyl groups remain in the final product. In addition, the presence of a π to π* satellite peak at ~ 290.7 eV is found, indicating that delocalized π conjugation is significantly stronger in the highly reduced laser scribed graphene as this peak is miniscule in the graphite oxide XPS spectrum.[35] The appearance of the delocalized π peak is a clear indication that conjugation in the GO film is restored during the laser reduction process and adds support that an sp^2 carbon network has been re-established. The decreased intensity of the oxygen-containing functional groups, the dominating C–C bond peak, and the presence of the delocalized π conjugation all indicate that a low-energy infrared laser is an effective tool in the generation of hr-LSG.

5.4 hr-LSG Sensors

Having established that hr-LSG has effective π conjugation, it is possible to construct devices to make use of the conducting material. Figure 5.3a shows a set of interdigitated electrodes with dimensions of 6 mm × 6 mm, spaced at ~ 500 μm, that are directly patterned onto a thin film of graphite oxide. Prior to being patterned, the graphite oxide film was deposited on a thin flexible substrate, polyethylene terephthalate (PET), in order to fabricate a set of electrodes that are mechanically flexible. A green arrow points to the laser scribed graphene region that makes up the black interdigitated electrodes, while a red arrow points to the unreduced golden colored graphite oxide film. Since the electrodes are directly patterned onto the GO film on a flexible substrate, the necessity for post-processing, such as transferring the film to a new substrate, is unnecessary. Although, if desired, a peel and stick method could be used to selectively lift-off the LSG with, for example, polydimethylsiloxane (PDMS) and transfer it onto other types of substrates (Figure 5.3b). The simplicity of this method allows substantial control over pattern dimensions, substrate selectivity, and even the electrical properties of the LSG by controlling the laser intensity and thereby the amount of reduction.

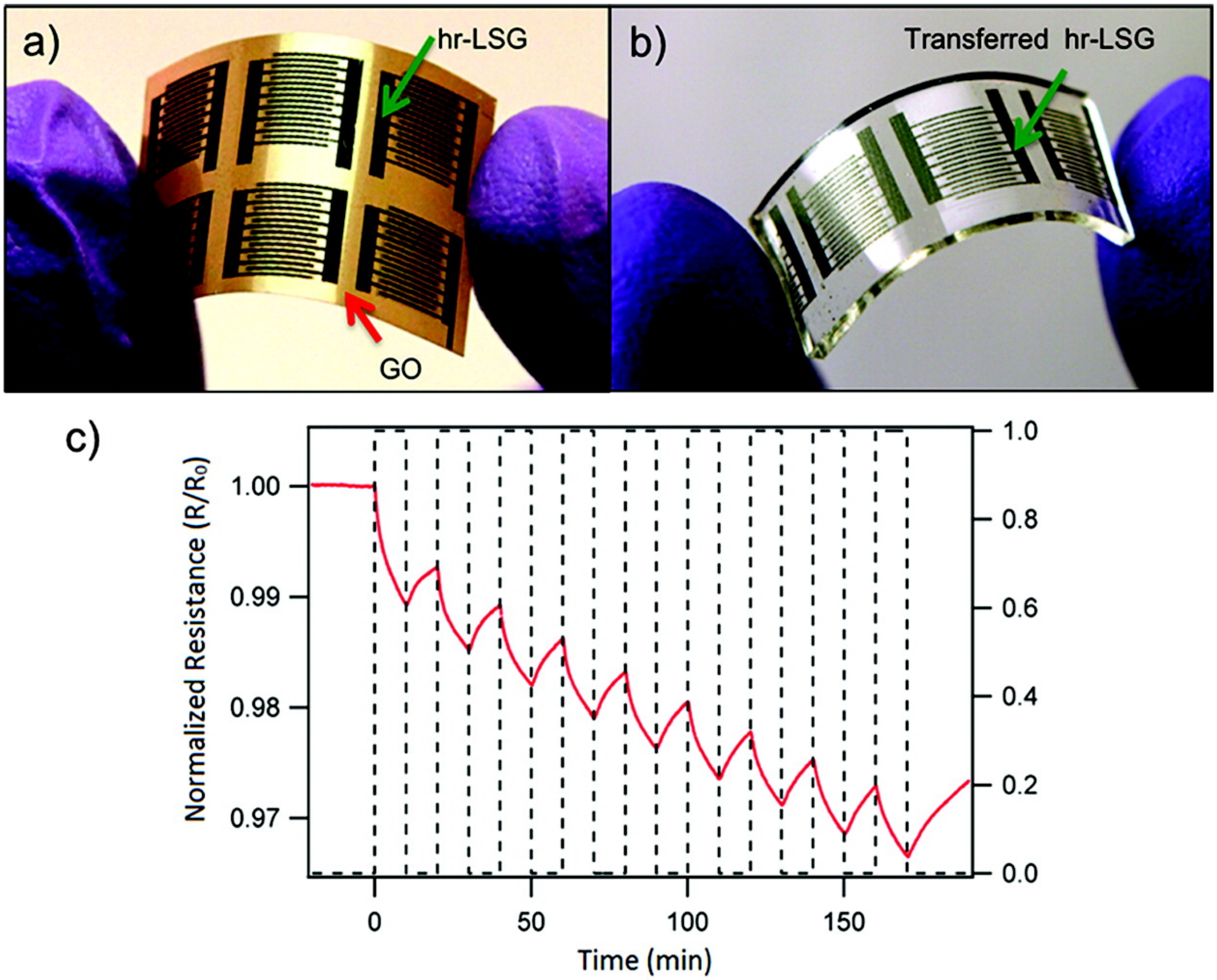

Figure 5.3 (a) All-organic flexible set of interdigitated electrodes generated from highly reduced laser scribed graphene (hr-LSG). (b) Same interdigitated electrodes transferred onto polydimethylsiloxane (PDMS). (c) NO_2 detection using the same all-organic flexible interdigitated electrodes. Here the sensor uses hr-LSG as the active electrodes and marginally laser-reduced graphite oxide as the detecting media. The NO_2 concentration is 20 ppm in dry air gas.

These interdigitated electrodes can in turn be used as an all-organic flexible gas sensor for the detection of NO_2. Figure 5.3c shows the sensor response for a patterned flexible set of interdigitated LSG electrodes that are exposed to 20 ppm of NO_2 in dry air. This sensor was fabricated by patterning hr-LSG as the active electrode and marginally reducing the area between the electrodes to have a consistent sheet resistance of ~7775 Ω/sq. In this way, it is possible to bypass the use of metal electrodes and directly pattern both the electrode and the sensing material on the flexible substrate simultaneously. The plot relates NO_2 gas exposure to R/R_0, where R_0 is the sheet resistance at the initial state and R is the resistance of the LSG film after exposure to the gas. The film was exposed to NO_2 gas for 10 min followed immediately by purging with air for another 10 min. This process was then repeated nine more times for a total of 200 min. Even with a slightly lower sensitivity than more sophisticated and optimized sensors, the un-optimized LSG sensor still shows good, reversible sensing for NO_2, and its easy fabrication makes it quite advantageous for these systems.[36, 37] Therefore, the LSG sensor for NO_2 holds promise for improving the fabrication of all-organic flexible sensor devices at low cost by using inexpensive starting materials directly patterned with an inexpensive laser.

5.5 Results and Discussions

The high conductivity and the increase in surface area resulting from the expanded LSG make this material a viable candidate for use as a heterogeneous catalyst for metal nanoparticles. In particular, the direct growth of platinum nanoparticles on LSG could aid in the improvement of methanol-based fuel cells, which have shown enhanced device performance from large surface area and conducting carbon-based scaffolds.[38] Here, we demonstrate that hr-LSG is a viable scaffold for the controllable growth of Pt nanoparticles. By electrochemically reducing 1 mM of K_2PtCl_4 with 0.5 M H_2SO_4 at −0.25 V for different periods of time, it is possible to actively control the platinum particle size that is electrodeposited on the hr-LSG film. Figure 5.4 shows scanning electron microscopy images illustrating the growth of Pt nanoparticles with respect to electrodeposition times corresponding to 0, 15, 60, and 120 s. As expected, there are no platinum particles present at 0 s of electrodeposition (Figure 5.4a), but small Pt nanoparticles are clearly visible after just 15 s (Figure 5.4b) with nanoparticle sizes ranging from 10 to 50 nm (Figure 5.4b, inset). After 60 s of electrodeposition, larger platinum nanoparticles grow with particle sizes averaging 100 to 150 nm (Figure 5.4c). Finally, after 120 s, 200 to 300 nm particles are found evenly distributed across the surface of the LSG. The active growth of Pt nanoparticles at controllable diameters on LSG could make it a potentially useful hybrid material for applications that require metal nanoparticles, such as methanol fuel cells and gas phase catalysts.[39-42] These applications are now being explored.

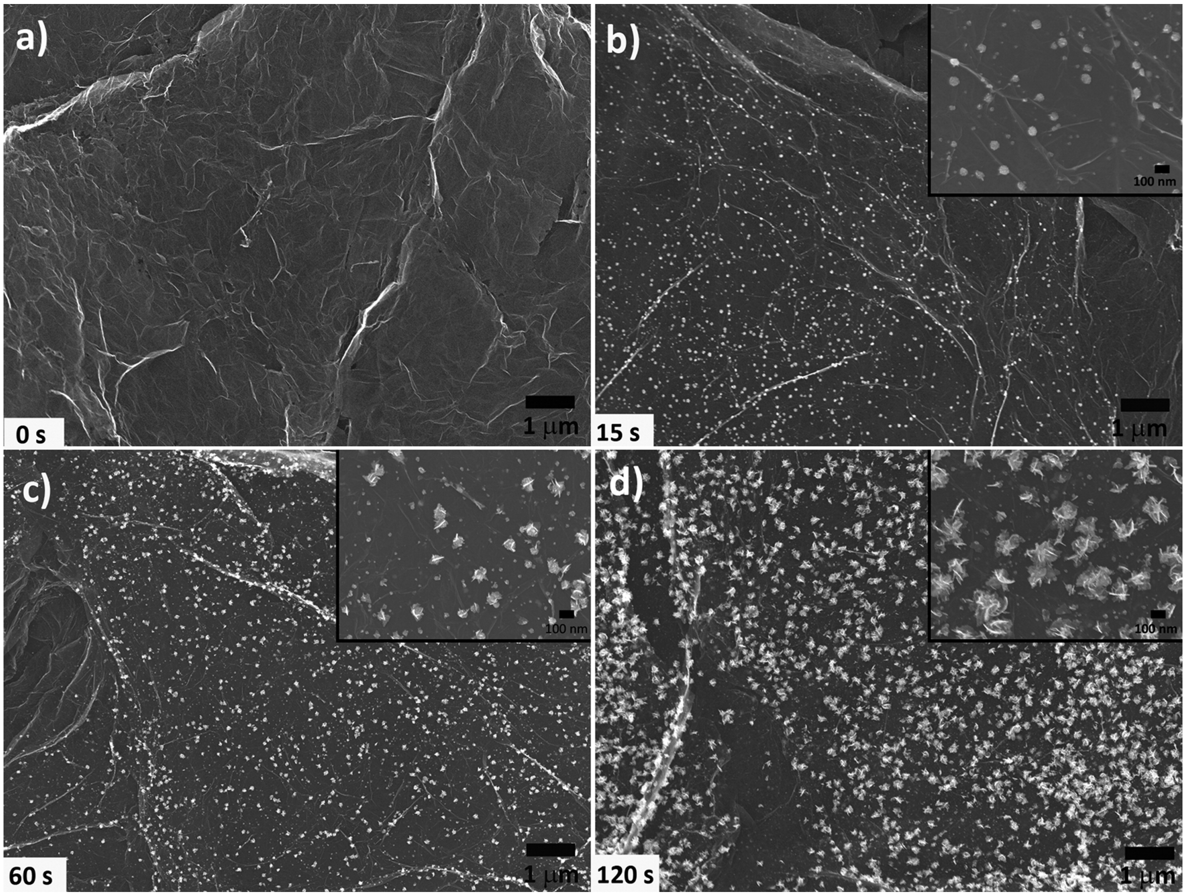

Figure 5.4 Scanning electron microscopy (SEM) analysis of platinum nanoparticle growth on LSG films. LSG is shown to be an excellent heterogeneous scaffold for the growth of platinum nanoparticles by electrochemically reducing 1 mM K_2PtCl_4 + 0.5 M H_2SO_4 at –0.25 V for (a) 0 s, (b) 15 s, (c) 60 s, and (d) 120 s. The result is an increase in the size of the Pt nanoparticles as a function of electrodeposition time. The insets in b–d show a magnified view of each set of nanoparticles, with nanoparticles ranging from 10 to 50 nm after 15 s to 200–300 nm after 120 s. Inset scale bars = 100 nm.

5.6 Electrochemical Analysis of hr-LSG

It has been previously shown that the immobilization of carbon nanotubes (CNTs) on glassy carbon electrodes will result in a thin porous CNTs film, which directly affects the voltammetric behavior of the CNT modified electrodes.[43] In a ferro/ferrocyanide redox couple, the voltammetric current measured at the CNT modified electrode will likely have two types of contributions. The thin layer effect is a major type of contribution that stems from the oxidation of ferrocyanide ions, which get trapped between the nanotubes. The other contribution results from the semi-infinite diffusion of ferrocyanide towards the planar electrode surface. Unfortunately, the mechanistic information is not easily de-convoluted and requires knowledge of the film thickness. In our case, on the other hand, no thin layer effect is observed since a plot of $\log_{10}$ of peak current versus $\log_{10}$ of the applied voltammetric scan rate (Figure 5.5) is linear with a slope of 0.53 (the average of three measurements). A value that is very close to the theoretical value calculated using the semi-infinite diffusion model as governed by the Randles-Sevcik equation:[44]

$$i_p = 0.3443AC_0^*\sqrt{\frac{D_0v(nF)^3}{RT}} \qquad \textbf{Equation 5.2}$$

The fact that graphene-based modified electrodes have no thin layer effect is similar to previous observations of other research groups.[45, 46]

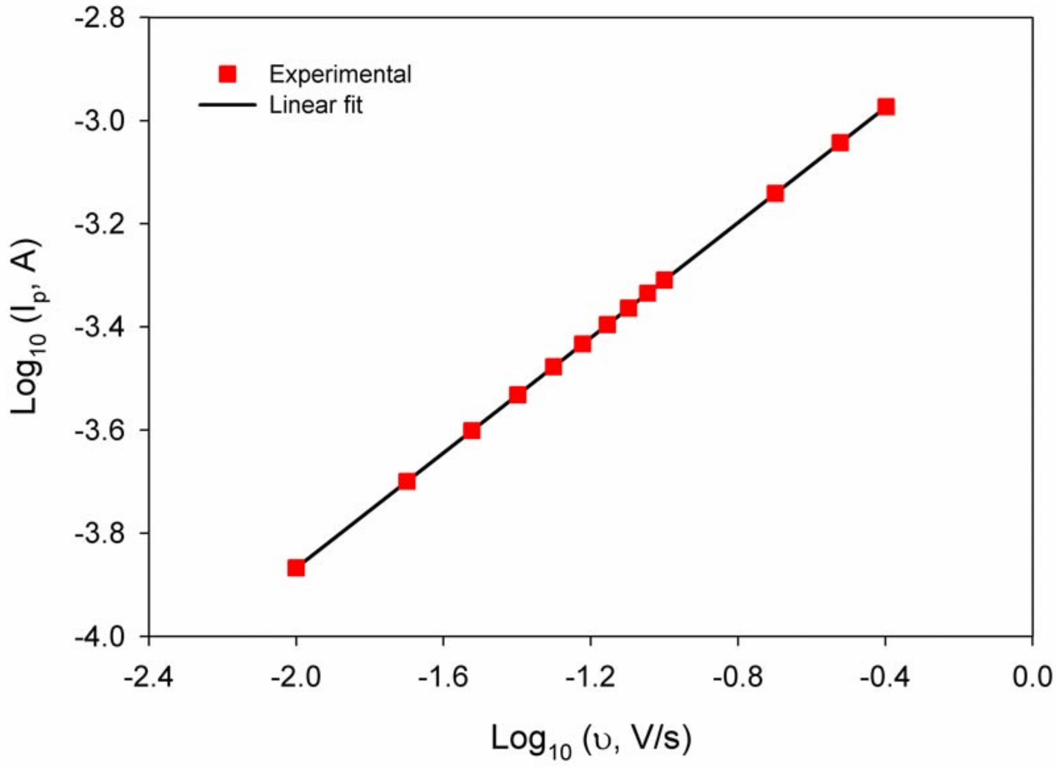

Figure 5.5 Electron transfer kinetics. Dependence of the peak current (i_p) of $[Fe(CN)_6]^{3-/4-}$ redox couple on the applied scan rate (υ) for hr-LSG electrode. The peak currents were obtained from the cyclic voltammograms of hr-LSG electrode in 5 mM $K_3[Fe(CN)_6]/K_4[Fe(CN)_6]$ (1:1 molar ratio) dissolved in 1.0 M KCl solution and run at scan rates of 0.01 to 0.4 V/s. The plot is linear with a slope of 0.53 indicating a semi-infinite diffusion mechanism.

Carbon electrodes have attracted tremendous interest for various electrochemical applications because of their wide potential window and good electrocatalytic activity for many redox reactions.[47, 48] Given its high surface area and flexibility and the fact that it is an all-carbon electrode, laser scribed graphene could revolutionize electrochemical systems by making miniaturized and fully flexible devices. Here, understanding the electrochemical properties of laser scribed graphene is highly beneficial to determine its potential for electrochemical applications. Recently, graphene's electrocatalytic properties have been demonstrated to stem, in large part, from the efficient electron transfer at its edges rather than its basal planes. In fact, it has been reported that graphene exhibits in certain systems electrocatalytic activity similar to that of edge plane highly ordered pyrolytic graphite.[49] In addition to having a highly expanded network, hr-LSG also displays a large amount of edge planes (Figure 5.2), making it an ideal system for studying the role of edge planes on the electrochemistry of graphene-based nanomaterials. Here, we explore the electrochemical behavior associated with the electron transfer of flexible hr-LSG electrodes using an $[Fe(CN)_6]^{3-/4-}$ couple as a redox probe. Figure 5.6 compares the CV profiles of GO, graphite, and hr-LSG electrodes in an equimolar mixture of 5 mM $K_3[Fe(CN)_6]/K_4[Fe(CN)_6]$ dissolved in 1.0 M KCl solution at a scan rate of 50 mV/s. Unlike GO and graphite, the hr-LSG electrode approaches the behavior of a perfectly reversible system with a low ΔE_p (peak-to-peak potential separation) of 59.5 mV at a scan rate of 10 mV/s to 97.6 mV at a scan rate 400 mV/s. The low ΔE_p values approach the calculated theoretical value of 59 mV. Given that ΔE_p is directly related to the electron transfer rate constant (k_{obs}^0), the low experimental value of ΔE_p indicates a very fast electron transfer rate.[45] The calculated k_{obs}^0 values vary from 1.266×10^{-4} cm s^{-1} for graphite and as expected increases for hr-LSG to 1.333×10^{-2} cm s^{-1}. In addition to the impressive increase in the electron transfer rate at the hr-LSG electrode (2 orders of magnitude faster than a graphite electrode), there is also substantial electrochemical activity for the hr-LSG electrode as seen by an increase of ~ 268% in the voltammetric peak current. These drastic improvements are attributed to the expanded architecture of hr-LSG films, which provide large open areas for the effective diffusion of the electroactive species and allow a better interfacial interaction with the LSG surface.

Additionally, it is surmised that the amount of edge-like surface per unit mass is thus much higher than graphite and therefore contributes to the higher electron transfer rates as seen here. Given the large number of exposed edge sites in hr-LSG, it is not surprising to find that it not only has a higher ${k_{obs}}^0$ value than graphite, but also surpasses that of carbon-nanotube-based electrodes[51, 52] and that of stacked graphene nanofibers.[53]

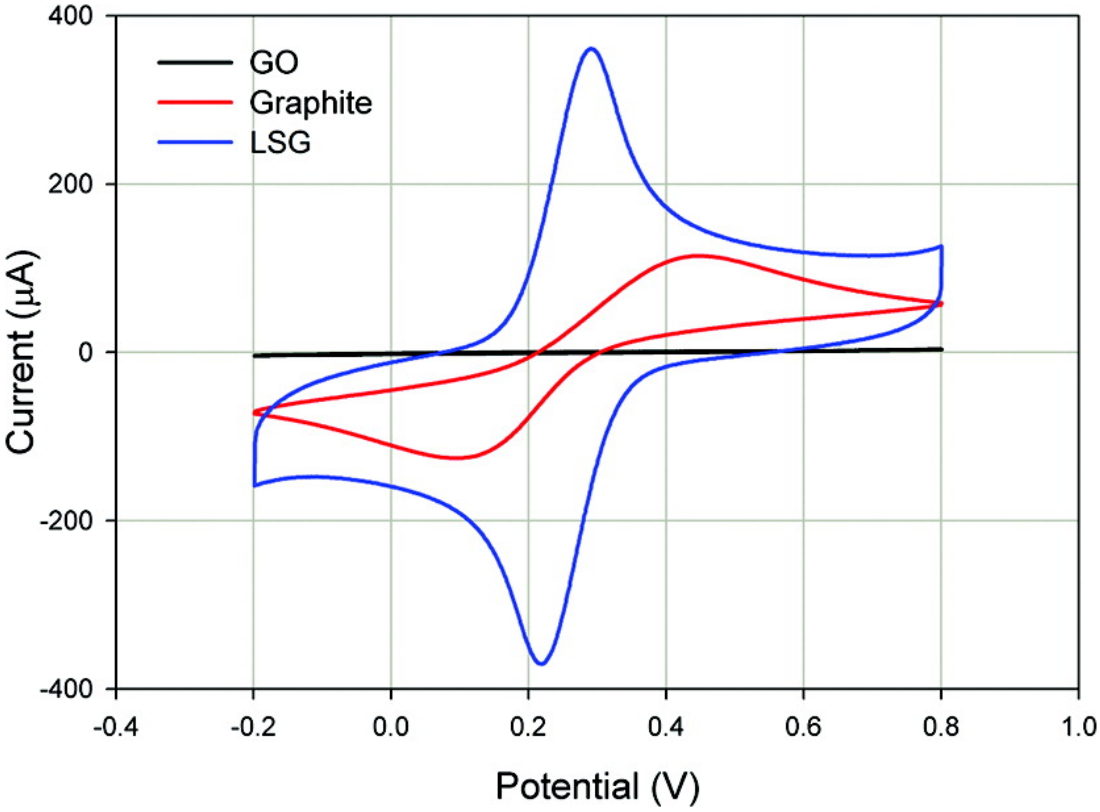

Figure 5.6 CV profiles of graphite oxide (GO), graphite, and hr-LSG electrodes in equimolar mixture (5 mM) of $K_3[Fe(CN)_6]/K_4[Fe(CN)_6]$ dissolved in 1.0 M KCl solution at a scan rate of 50 mV/s. The hr-LSG electrode approaches the behavior of a perfect reversible system with a peak-to-peak potential of 59.5 mV at 10 mV/s, which is close to the theoretical Nerstian value of 59 mV. The hr-LSG shows high electron transfer rates, 105 times faster than graphite and even higher than values reported for carbon nanotube electrodes[51] and stacked graphene nanofibers.[53]

Note that the hr-LSG electrodes are fabricated on flexible PET substrates covered with graphite oxide, which when laser-reduced serves as both the electrode and the current collector, thus making this particular electrode not only lightweight and flexible but also inexpensive. In addition, the low oxygen content in hr-LSG (~3.5%), as shown through XPS analysis, is quite advantageous to the electrochemical activity seen here since a higher oxygen content at the edge plane sites has been shown to limit and slow down the electron transfer of the ferri-/ferrocyanide redox couple.[54] We believe this new process presents an interesting methodology for making highly electroactive electrodes for potential applications in vapor sensing, biosensing, electrocatalysis, and energy storage.

5.7 Conclusions

A new method has been presented for producing graphene-based materials that is not only facile, inexpensive, and versatile but is a one-step "green" process for reducing and patterning graphene films in the solid state. A simple low-energy, inexpensive infrared laser is used as a powerful tool for the effective reduction and subsequent expansion and exfoliation and fine patterning of graphite oxide. Aside from the ability to directly pattern and effectively produce large areas of highly reduced laser scribed graphene films, this method is applicable to a variety of other thin substrates and has the potential to simplify the manufacturing process of devices made entirely from organic materials. A flexible all-organic gas sensor has been fabricated directly by laser patterning of graphite oxide deposited on thin flexible PET. LSG is also shown to be an effective scaffold for the successful growth and size control of Pt nanoparticles *via* a simple electrochemical process. Finally, a flexible hr-LSG electrode was fabricated, which displays a textbook-like reversibility with an impressive increase of ~238% in electrochemical activity when compared to graphite toward the electron transfer between the ferri-/ferrocyanide redox couple. This proof-of-concept process has the potential to effectively improve applications that would benefit from the high electrochemical activity demonstrated here including batteries, sensors, and electrocatalyts.

5.8 References

1. Compton, O. C.; Nguyen, S. T. *Small* **2010**, *6*, 711 – 723
2. Zhu, Y.; Stoller, M. D.; Cai, W.; Velamakanni, A.; Piner, R. D.; Chen, D.; Ruoff, R. S. *ACS Nano* **2010**, *4*, 1227 – 1233
3. De, S.; King, P. J.; Lotya, M.; O'Neill, A.; Doherty, E. M.; Hernandez, Y.; Duesberg, G. S.; Coleman, J. N. *Small* **2010**, *6*, 458 – 464
4. Jung, I.; Dikin, D. A.; Piner, R. D.; Ruoff, R. S. *Nano Lett.* **2008**, *8*, 4283 – 4287
5. Stankovich, S.; Piner, R. D.; Chen, X.; Wu, N.; Nguyen, S. T.; Ruoff, R. S. *J. Mater. Chem.* **2006**, *16*, 155 – 158
6. Stankovich, S.; Dikin, D. A.; Piner, R. D.; Kohlhaas, K. A.; Kleinhammes, A.; Jian, Y.; Wu, Y.; Nguyen, S. T.; Ruoff, R. S. *Carbon* **2007**, *45*, 1558 – 1565
7. Gilje, S.; Han, S.; Wang, M.; Wang, K. L.; Kaner, R. B. *Nano Lett.* **2007**, *7*, 3394 – 3398
8. Tung, V. C.; Allen, M. J.; Yang, Y.; Kaner, R. B. *Nature Nanotech.* **2009**, *4*, 25 – 29
9. McAllister, M. J.; Li, J. L.; Adamson, D. H.; Schniepp, H. C.; Abdala, A. A.; Liu, J.; Herrera-Alonso, M.; Milius, D. L.; Car, R.; Prud'homme, R. K. *Chem. Mater.* **2007**, *19*, 4396 – 4404
10. Dubin, S.; Gilje, S.; Wang, K.; Tung, V. C.; Cha, K.; Hall, A. S.; Farrar, J.; Varshneya, R.; Yang, Y.; Kaner, R. B. *ACS Nano* **2010**, *4*, 3845 – 3852
11. Wang, H.; Robinson, J. T.; Li, X.; Dai, H. *J. Am. Chem. Soc.* **2009**, *131*, 9910 – 9911
12. Eda, G.; Fanchini, G.; Chhowalla, M. *Nat. Nanotechnol.* **2008**, *3*, 270 – 274
13. Gilje, S.; Dubin, S.; Badakhshan, A.; Farrar, J.; Danczyk, S. A.; Kaner, R. B. *Adv. Mater.* **2010**, *22*, 419 – 423

14. Cote, L. J.; Cruz-Silva, R.; Huang, J. *J. Am. Chem. Soc.* **2009**, *131*, 11027 – 11032

15. Abdelsayed, V.; Moussa, S.; Hassan, H. M.; Aluri, H. S.; Collision, M. M.; El-Shall, M. S. *J. Phys. Chem. Lett.* **2010**, *1*, 2804 – 2809

16. Huang, L.; Liu, Y.; Ji, L.-C.; Xie, Y.-Q.; Wang, T.; Shi, W.-Z. *Carbon* **2011**, *49*, 2431 – 2436

17. Sokolov, D. A.; Shepperd, K. R.; Orlando, T. M. *J. Phys. Chem. Lett.* **2010**, *1*, 2633 – 2636

18. Zhang, Y.; Guo, L.; Wei, S.; He, Y.; Xia, H.; Chen, Q.; Sun, H.-B.; Xiao, F.-S. *Nano Today* **2010**, *5*, 15 – 20

19. Gao, W.; Singh, N.; Song, L.; Liu, Z.; Reddy, A. L. M.; Ci, L.; Vajtai, R.; Zhang, Q.; Wei, B.; Ajayan, P. M. Films *Nat. Nanotech.* **2011**, *6*, 496 – 500

20. Stinson, D. G.; Maguire, M. LightScribe Direct Disc Labeling, **2005**.

21. Yang, D.; Velamakanni, A.; Bozoklu, G.; Park, S.; Stoller, M. D.; Piner, R. D.; Stankovich, S.; Jung, I.; Field, D. A.; Ventrice, C. A. *Carbon* **2009**, *47*, 145 – 152

22. Ferrari, A. C.; Meyer, J. C.; Scardaci, V.; Casiraghi, C.; Lazzeri, M.; Mauri, F.; Piscanec, S.; Jiang, D.; Novoselov, K. S.; Roth, S. *Phys. Rev. Lett.* **2006**, *97*, 187401 – 187404

23. Cong, C. X.; Yu, T.; Ni, Z. H.; Liu, L.; Shen, Z. X.; Huang, W. *J. Phys. Chem. C* **2009**, *113*, 6529 – 6532

24. Tuinstra, F.; Koenig, J. L. *J. Chem. Phys.* **1970**, *53*, 1126 – 1130

25. Kudin, K. N.; Ozbas, B.; Schniepp, H. C.; Prud'homme, R. K.; Aksay, I. A.; Car, R. *Nano Lett.* **2008**, *8*, 36 – 41

26. Ferrari, A. C. *Solid State Commun.* **2007**, *143*, 47 – 57

27. Dato, A.; Radmilovic, V.; Lee, Z.; Phillips, J.; Frenklach, M. *Nano Lett.* **2008**, *8*, 2012 –

2016

28. Cuong, T. V.; Pham, V. H.; Tran, Q. T.; Hahn, S. H.; Chung, J. S.; Shin, E. W.; Kim, W. J. *Mater. Lett.* **2010**, *64*, 399 – 401

29. Dikin, D. A.; Stankovich, S.; Zimney, E. J.; Piner, R. D.; Dommett, G. H. B.; Evme- nenko, G.; Nguyen, S. T.; Ruoff, R. S. *Nature* **2007**, 448, 457 – 460.

30. Park, S.; Lee, K.-S.; Bozoklu, G.; Cai, W.; Nguyen, S. T.; Ruoff, R. S. *ACS Nano* **2008**, *2*, 572 – 578.

31. Buchsteiner, A.; Lerf, A.; Pieper, J. J. Phys. Chem. B **2006**, *110*, 22328 – 22338.

32. Lerf, A.; Buchsteiner, A.; Pieper, J.; Schöttl, S.; Dekany, I.; Szabo, T.; Boehm, H. P. *J. Phys. Chem. Solids* **2006**, *67*, 1106 – 1110.

33. Dreyer, D. R.; Park, S.; Bielawski, C. W.; Ruoff, R. S. *Chem. Soc. Rev.* **2010**, *39*, 228 – 240

34. Shin, H. J.; Kim, K. K.; Benayard, A.; Yoon, S. M.; Park, H. K.; Jung, I.-S.; Jin, M. H.; Jeong, H. K.; Kim, J. M.; Choi, J.-Y. *Adv. Funct. Mater.* **2009**, *19*, 1987 – 1992

35. Gao, W.; Alemany, L. B.; Ci, L.; Ajayan, P. M. *Nat. Chem.* **2009**, *1*, 403 – 408

36. Fowler, J. D.; Allen, M. J.; Tung, V. C.; Yang, Y.; Kaner, R. B.; Weiller, B. H. *ACS Nano* **2009**, *3*, 301 – 306

37. Robinson, J. T.; Perkins, F. K.; Snow, E. S.; Wei, Z.; Sheehan, P. E. *Nano Lett.* **2008**, *8*, 3137 – 3140

38. Li, Y.; Gao, W.; Ci, L.; Wang, C.; Ajayan, P. M. *Carbon* **2010**, *48*, 1124 – 1130

39. Qiu, J.-D.; Wang, G.-C.; Liang, R.-P.; Xia, X.-H.; Yu, H. W. *J. Phys. Chem. C* **2011**, *115*, 15639 – 15645

40. Seger, B.; Kamat, P. V. *J. Phys. Chem. C* **2009**, *113*, 7990 – 7995

41. Ha, H. W.; Kim, I. Y.; Hwang, S. J.; Ruoff, R. S. *Electrochem. Solid State* **2011**, *14*, B70 – B73

42. Moussa, S.; Abdelsayed, V.; El-Shall, M. S. *Chem. Phys. Lett.* **2011**, *510*, 179 – 184

43. Streeter, I.; Wildgoose, G. G.; Shao, L.; Compton, R. G. *Sensors and Actuators B* **2008**, *133*, 462 – 466.

44. Zoski, C. G., Ed. Handbook of Electrochemistry, 1st ed.; Elsevier: Radarweg 29, P.O. Box 211, 1000 AE Amsterdam. The Netherlands, 2007.

45. Hallam, P. M.; Banks, C. E. *Electrochem. Commun.* **2011**, *13*, 8 – 11.

46. Ambrosi, A.; Bonanni, A.; Pumera, M Nanoscale **2011**, *3*, 2256 – 2260.

47. Chen, D.; Tang, L.; Li, J. *Chem. Soc. Rev.* **2010**, *39*, 3157 – 3180

48. Yang, W.; Ratinac, K. R.; Ringer, S. P.; Thordarson, P.; Gooding, J. J.; Braet, F. Carbon *Angew. Chem., Int. Ed.* **2010**, *49*, 2114 – 2138

49. Kampouris, D. K.; Banks, C. E. *Chem. Commun.* **2010**, *46*, 8986 – 8988

50. Hallam, P. M.; Banks, C. E. *Electrochem. Commun.* **2011**, *13*, 8 – 11

51. Pumera, M.; Sasaki, T.; Iwai, H. *Chem. Asian J.* **2008**, *3*, 2046 – 2055

52. Streeter, I.; Wildgoose, G. G.; Shao, L.; Compton, R. G. *Sens. Actuators, B* **2008**, *133*, 462 – 466

53. Ambrosi, A.; Bonanni, A.; Pumera, M. *Nanoscale* **2011**, *3*, 2256 – 2260

54. Ji, X.; Banks, C. E.; Crossley, A.; Compton, R. G. *Chem. Phys. Chem.* **2006**, *7*, 1337 – 1344

55. Kovtyukhova, N. I.; Oliver, P. I.; Martin, B. R.; Mallouk, T. E.; Chizhik, S. A.; Buzaneva, E. V.; Gorchinskiy, A. D. *Chem. Mater.* **1999**, *11*, 771 – 778

56. Nicholson, R. S. *Anal. Chem.* **1965**, *37*, 1351 – 1355

57. Konopka, S. J.; McDuffie, B. *Anal. Chem.* **1970**, *42*, 1741 – 1746

Chapter 6

Investigation of Barrier Properties of Graphene and Graphene Oxide on PET for Electronic Encapsulation

6.1 Introduction

Optoelectronic devices, such as organic light-emitting diodes (OLEDs) and organic photovoltaics (OPVs) are rapidly gaining momentum as the technologies of choice for future flat panel displays and solar power generation, respectively. To achieve an operating lifetime in excess of a few tens of hours, however, isolation of the OLED from atmospheric oxygen and water vapor is necessary. On glass, this is typically accomplished with a glass or metal lid, attached to the substrate using a bead of UV-cured epoxy, but rigid materials like glass and metal inhibit flexibility, deemed advantageous and desirable for the future of OLED and OPV devices.[1] Polymeric material have been shown to be successfully used for manufacturing both OLED and OPV devices.[2] However, the moisture sensitivity of OLEDs has thus far prevented the realization of their full potential to form the basis for next-generation emissive displays on lightweight or flexible plastics, due to the extremely rapid permeation of both water and oxygen through all known plastic substrates.

Conventional barrier film fabrication is carried out by costly, energy intensive nanometer-thin film growth processes of amorphous oxides like SiO_xN_y, SiO_xC_y, Al_2O_3, or Zr_2O_4 on flexible plastic substrates by Chemical Vapor Deposition (CVD). PET, poly(ethylene terephthalate), is a typical base film that's used. A single sub-ten nanometer thick film of these oxides can, theoretically, provide a hermetic barrier against water and oxygen gas. Practically, there is no way to achieve such a film by current technology. Films are laden with defects such as pinholes from process variances like substrate inhomogeneities and thermal gradients. To compensate for these defects, repeating multilayers of oxide films/polymer films are deposited, called dyads. Dyad stacking creates a tortuous path for gas molecules to migrate, effectively rendering a flexible barrier showing a $1x10^{-4}$ g/cm^2 day water vapor transmission rate (WVTR)[3] on a commercial scale. However, this is still not acceptable for flexible electronics. It's been suggested that a film with $1x10^{-7}$ g/cm^2 day will enable the practical use of flexible organic electronics.[4]

Graphene is an atom thick, single layer of two-dimensional sp^2-hybridized carbon that has attracted great interest since its discovery in 2004 due to its long-range π-conjugation, and extraordinary thermal, mechanical, and electrical properties.[5] It attenuates 2.3% of visible light per single sheet of graphene[5]; however, it has been demonstrated that a single sheet of graphene inhibits copper and silver corrosion and may be used as a flexible, transparent, virtually impermeable barrier material on plastics.[6, 7] The goal of this project is to investigate graphene, graphene oxide and their polymer composites as transparent gas barrier materials for electronic applications, where water and oxygen permeation are detrimental to life and efficiency of the devices.

6.2 Experimental Setup

6.2.1 Graphite Oxide Films

Graphite oxide (GO) was synthesized using a previously published procedure.[8] Dispersions of graphite oxide in water were synthesized by taking a 3 wt% GO slurry and diluting it with water to make 100, 60, 30, 20, 10, 5, 2, 1 mg of GO in 20 ml of water. The subsequent mixture was sonicated for 90 minutes at 50 °C to achieve complete graphite oxide exfoliation. Graphite oxide dispersions were drop-cast onto 108 μm thick, transparency grade PET (3M, PP2950), which was punched out into 3" circles by using a round punch hole (McMaster-Carr, Los Angeles, CA). Film thicknesses were measured using a digital micrometer with a precision of 1 μm (Mitutoyo, 293-348).

6.2.2 Gas Permeability System

A schematic of the permeability measuring system based on the manometric method for measuring film permeability, also known as the constant volume method, is shown in Figure 6.1.[9] Gas pressure is applied from a cylinder, through the regulator (Figure 6.1R) and can be monitored using a digital pressure transducer (Figure 6.1P), the gas is connected or isolated from the upstream (top side) of the permeation cell system through a high pressure valve (Figure 6.1A). Both the upstream and the downstream sides of the permeation cells are connected to a high vacuum system, capable of reaching 1×10^{-5} Torr, through two high vacuum/pressure valves

(Figure 6.1B) and (Figure 6.1C). The film sample is mounted in a custom stainless-steel pressure cell with VCO vacuum fittings (Swagelok, CA) (Figure 6.1 inset). The test cell consists of two blank Conflat flanges (Varian Associates), sealed together with a Viton o-ring. The interior of the flanges are machined to contain the 3” sample, a bronze porous disk, and a Teflon aligning disk stacked in that order. The upper flange is machined for an o-ring, which seals to the upstream side of the membrane sample and defines the cross-sectional area for permeation. The downstream side of the test cell is connected to a series of Conflat flanges comprising the downstream volume. The downstream volume (Figure 6.1V_0) is a known volume container where the permeating gas will be collected and the rate of the gas permeation through the membrane will be recorded, using a computerized vacuum transducer.

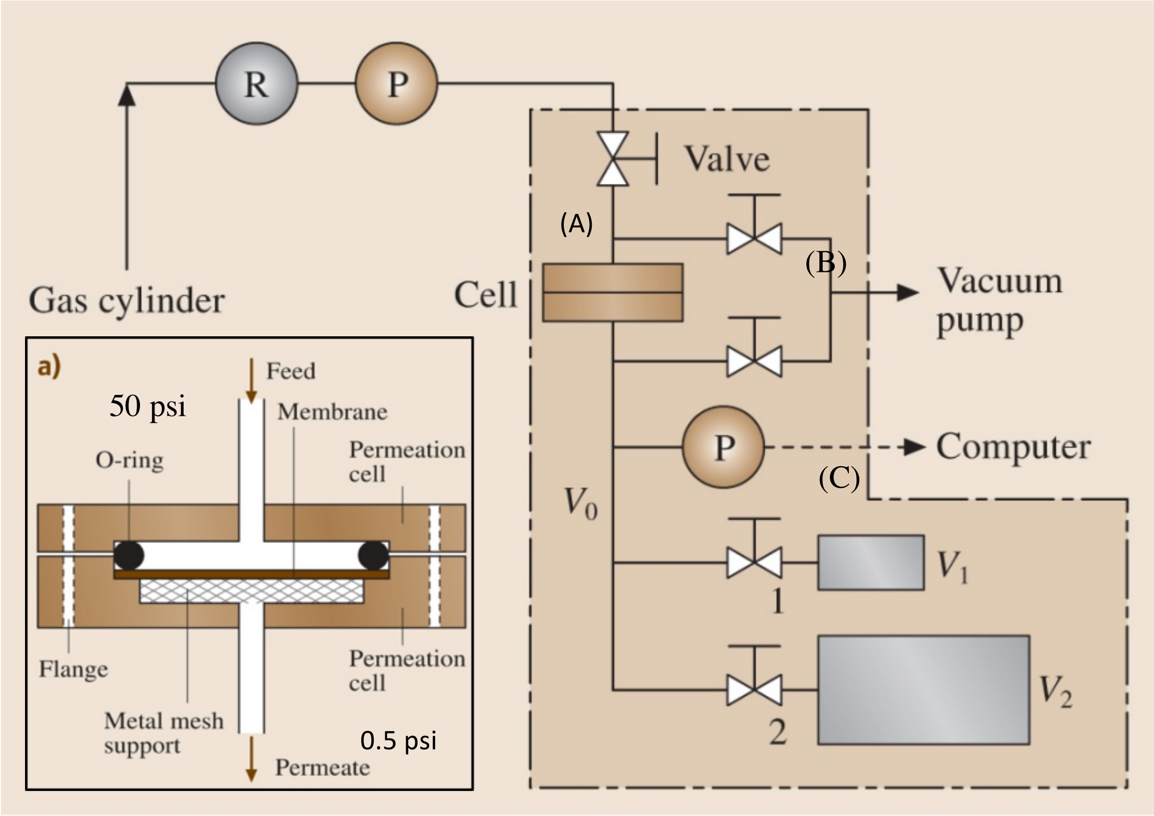

Figure 6.1 A schematic drawing of a typical manometric setup. A pressure of approximately 50 psi is applied from a gas cylinder through the regulator (R) which can be monitored using a pressure transducer (P), the gas is controlled through a high pressure valve (A) before it reaches a permeation cell on the upstream (top) side of the membrane. The downstream side (bottom), can be evacuated and has a mounted computerized vacuum transducer (P). When the desired vacuum is reached, the downstream side is isolated from the vacuum pump by closing valves (B) and (C). As the gas permeates through the membrane to the downstream volume (V_0) and collects in volume (V_1) or (V_2), it will cause the pressure rise, and the rate of the pressure rise can be used to calculate the permeability of the membrane. The inset shows a schematic drawing of the permeation cell.

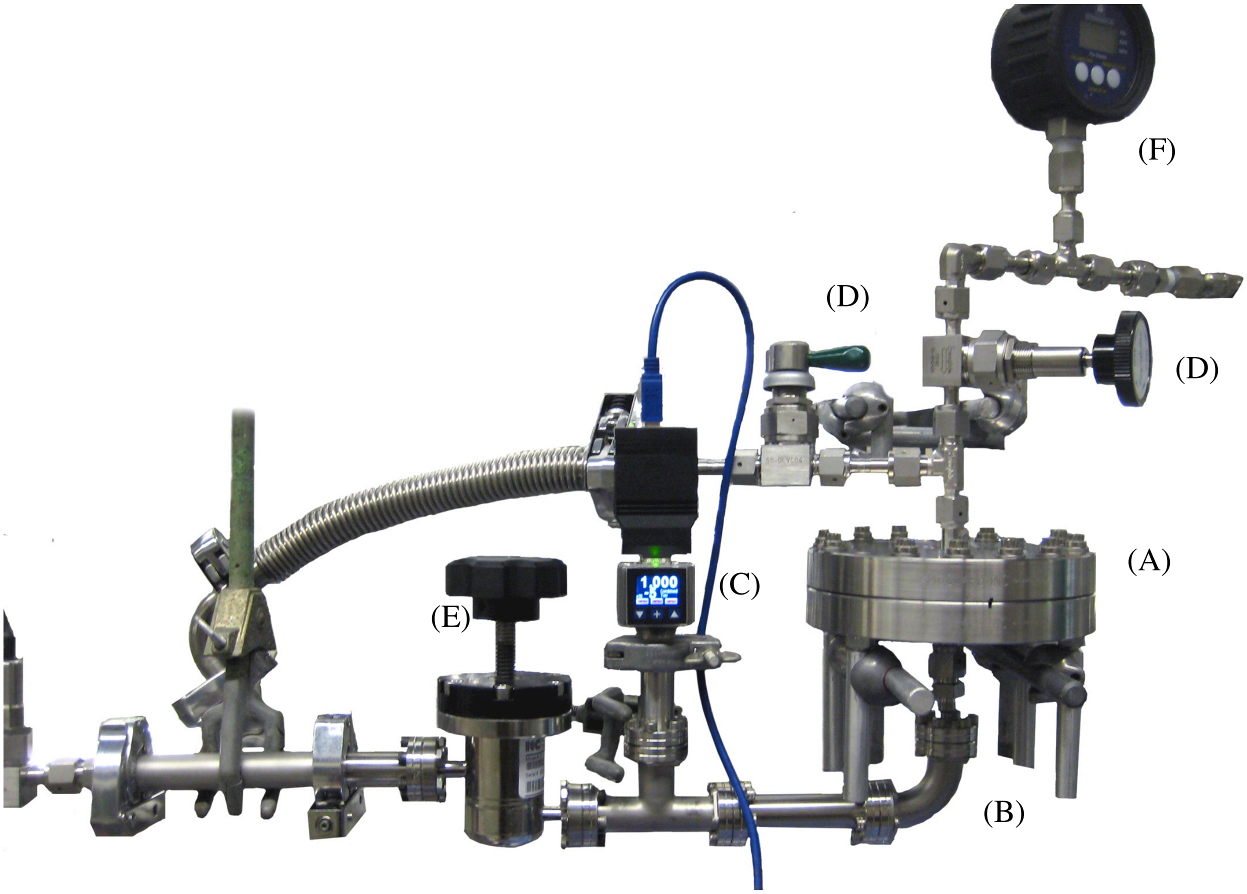

Figure 6.2 A photograph of the constructed gas permeation setup: A) permeation cell, B) downstream volume, C) digital vacuum transducer, D) high pressure valve, E) high vacuum valve, and F) high-pressure gauge.

In a typical experiment, both the upstream and downstream sides of the test cell are evacuated for 24 hours to achieve a pressure of $<1\text{x}10^{-5}$ Torr. Next, all vacuum valves are closed and $(dp_1/dt)_{leak}$, the leak rate of the system, is calculated by letting the setup accumulate pressure either through miniscule leaks in the seals or through off-gassing of the seals or the membrane material. The leak rate should be as small as possible in order to get highly sensitive measurements. A typical leak rate is approximately 3 mTorr/hr, but prolonged evacuation using a diffusion pump can lower the leak rate down to 1 mTorr/hr. A system leak rate of 14 mTorr/hour leads to a permeation sensitivity of $2\text{x}10^{-13}$ cc@STP conditions. After achieving the desirable leak rate, the system is evacuated again for 24 hours, the vacuum valves are closed and the high-pressure gas valve is open to pressurize the system on the upstream side to 50 psi. A test is run until the rate of pressure rise over time becomes constant. By using the permeation rate and the leak rate as given in Equation 6.1 below, we can calculate permeability of the membrane knowing its thickness, the test temperature, and the upstream pressure and area of the film available for transport.

$$P_a = \frac{V_d L}{p_2 ART}\left[\left(\frac{dP_1}{dt}\right)_{ss} - \left(\frac{dP_1}{dt}\right)_{leak}\right] \qquad \textbf{Equation 6.1}$$

V_d – Downstream volume (cm^3)

A – Film area available for gas (cm^2)

L – Film thickness (cm)

R – Gas constant: 0.278 cmHg cm^3/cm^3(STP) K

p_2 – Upstream pressure (cmHg)

T – Temperature (K)

$\left(\frac{dP_1}{dt}\right)_{ss}$ & $\left(\frac{dP_1}{dt}\right)_{leak}$ – Rates of pressure at steady-state and leak rate conditions (cmHg/s)

6.2.3 WVTR Permeability System

Measurements of water vapor transmission rates (WVTR) required certain modifications to be performed to the gas permeation setup. The high pressure cylinder was replaced with a water containing glass vessel (Figure 6.3D) connected inline to the upstream side of the setup through a series of Pyrex glassware (Figure 6.3C) and stainless steel fittings, as shown in Figure 6.3. The water contaning glass container is equiped with a valve which allows us to seal it off from the system when pulling vacuum on the upstream side. The water in the container was degassed under vaccum prior to the permeation experiments. A typical procedure for a WVTR measurement is as follows: Evacuate the downstream side of the permeation setup to $1x10^{-5}$ Torr, while also evacuating the upstream side to $2.0x10^{-3}$ Torr. Then, both sides of the permeation cell are isolated from the vacuum pump, and the valve is opened exposing the upstream side to the water vapor. As soon as the water vapor can escape its container and fill in the vacuum between the test cell and the vacuum pump, it creates a 100% humidity environment on the upstream side with a pressure of about 8 to 10 Torr. The length of the experiment correlates with the permeation properties of the membrane being tested, with thicker membranes often taking close to a week to obtain accurate measurements.

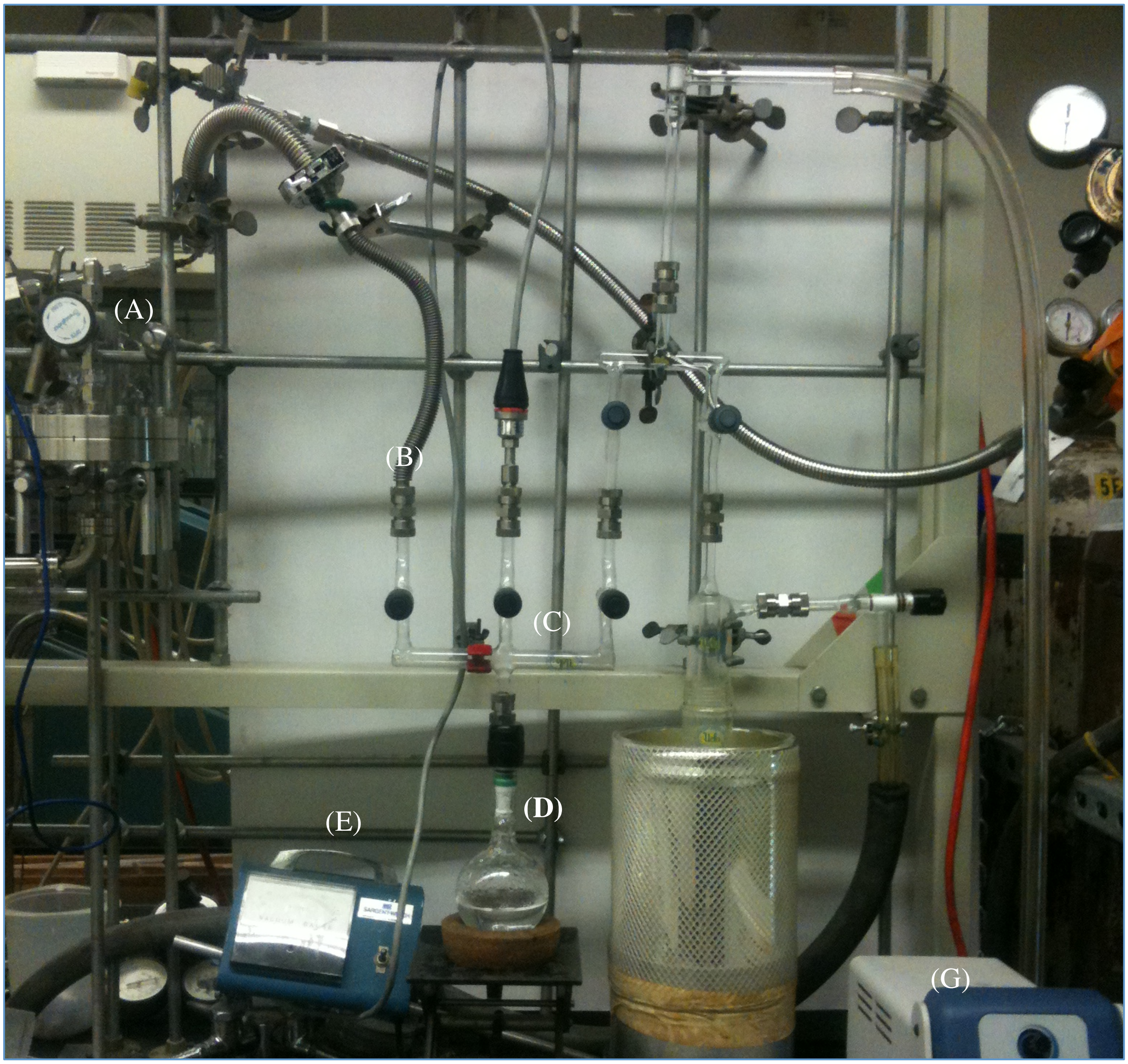

Figure 6.3 A photograph illustrating the water permeation attachment connected to the upstream side of the test cell. A valve (A) is connected on the bottom side of the test cell and on the top side to a series of metal tubing (B) ending with a multiarm Pyrex connector (C). The multiarm connector is also connected to the water container (D), a vacuum gauge (E), the liquid nitrogen condenser (F), and the vacuum pump (G).

6.2.4 Synthesis of Graphene

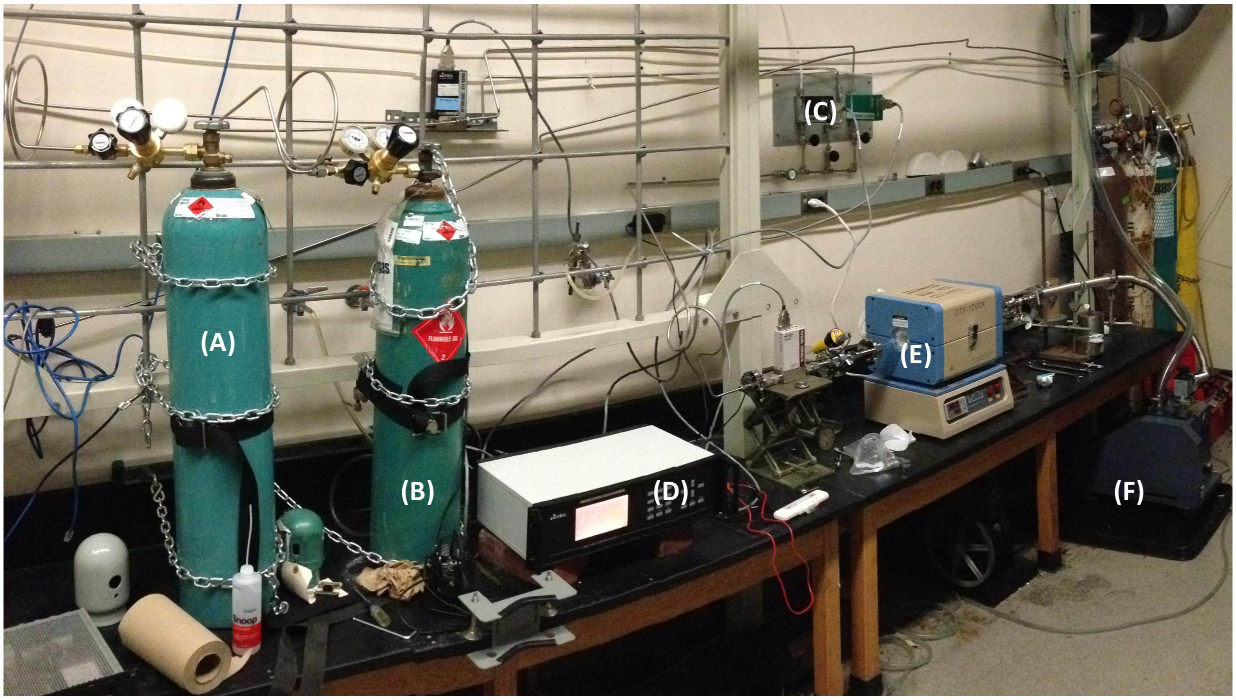

Figure 6.4 A photograph of a graphene CVD setup: (A) & (B) Hydrogen and methane gas, respectively; (C) mass flow controllers (MFCs); (D) power supply & regulator for MFCs; (E) furnace with a 1.5" glass tube; and (F) vacuum pump.

The system consists of a tube furnace (Figure 6.4E) into which a 1.5” quartz tube is inserted. The left hand side of the tube is connected to a mass flow controller (Figure 6.4C) which controls the overall pressure in the system, ideally set to 1000 mTorr. The pressure in the CVD chamber is due to a combination of several gases: methane and hydrogen plus argon as a carrier gas. The right hand side of the tube is connected to a needle valve that is used to adjust the vacuum as obtained from a vacuum pump. In a typical graphene growth experiment, a copper substrate (99.999% pure foil, Alfa-Aesar), with a 25 μm thickness, is inserted inside a quartz tube and annealed under flowing hydrogen for 10 min at 1000 °C to remove the oxide and to increase the average copper grain size. After 10 minutes, methane is added to the mixture of gasses and allowed to flow for 20 minutes. Finally, the furnace is rapidly cooled and the product is a single layer of graphene grown on the copper surface. The size of the oven as well as the glass tube are the limiting factors in the growth process; in principle, one can grow graphene as large as desired, as long as one has a large enough instrument.

Graphene transfer onto a PET substrate is accomplished by spin-coating and soft-baking poly(methyl methacrylate) (495 PMMA C9, Micro-Chem) onto the graphene-coated copper foil, at 180 °C for 2 min. PMMA serves as a support and a protective layer for graphene after the copper is etched away in an aqueous bath of $FeCl_3$, H_2O and concentrated HCl (3.5 g, 100 mL, and 10 mL, respectively). A rigid support is used to transfer the graphene/PMMA into a bath of de-ionized water, where it is rinsed for 30 min to remove any trace ion contaminates. Finally, the graphene is scooped up onto a target substrate and gently blown dry under nitrogen gas. Care is taken to avoid ripping the underlying graphene. A second PMMA layer is drop-cast onto the initial soft-baked PMMA layer, which dissolves the support and relaxes the strain in the underlying graphene film. Unlike previously described methods, the photo-resist was not cured, and instead each sample was directly soaked in acetone to remove the polymer support. The graphene is finally annealed in an argon and hydrogen environment for 6 h at 300 °C to remove any trace PMMA residue.

6.2.5 Setup for Hydrophobic Functionalization

Functionalization of GO was performed in a retrofitted vacuum oven as shown in Figure 6.5 below. The system consists of a vacuum oven into which the samples of GO/PET composites were loaded. Using an attached diaphragm vacuum pump, atmospheric pressure inside the vacuum oven was reduced to 1 Torr and the oven was heated to 85°C. After 15 minutes, the vacuum pump was turned off and the valve on the He tank was opened to the carrier gas to bubble through the hexamethyldisilazane (HMDS) and carry HMDS inside the oven through the oven's exhaust valve.

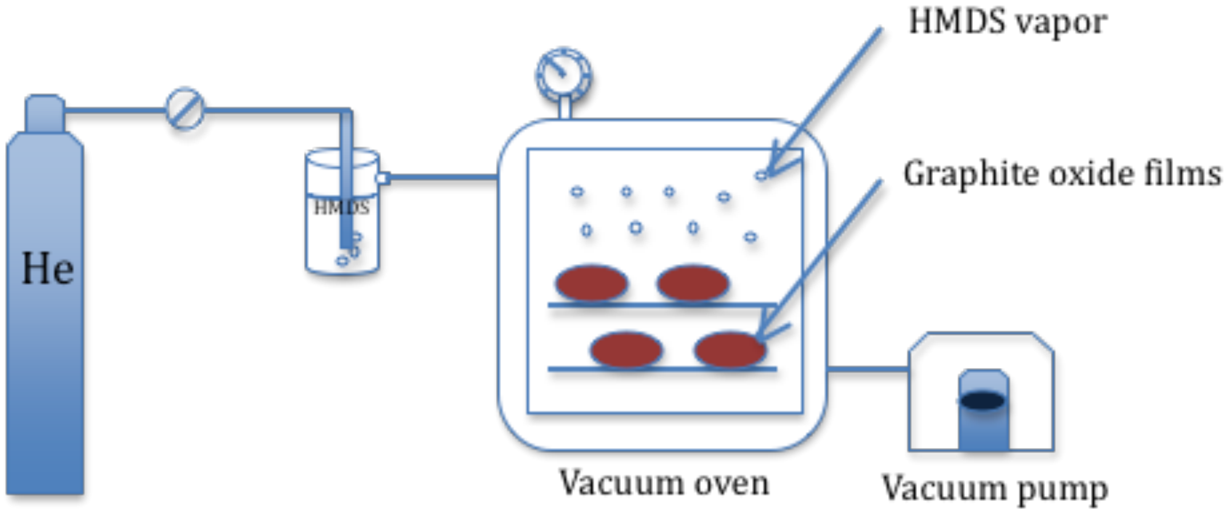

Figure 6.5 A schematic drawing of the vapor deposition setup. A helium tank is connected through a bleed valve into a sealed container with hexamethyldisilazane (HMDS). When the valve is open, the carrier gas (He) carries the HMDS into the pre-heated reaction chamber where it is allowed to react with hydroxyl groups on the GO surface for 24 hours at 85 °C. After the reaction is complete, the entire chamber is evacuated for 30 minutes and the sample is removed for characterization and analysis.

6.3 Results and Discussion

6.3.1 Oxygen and Helium Permeability of SRM and PET

Our intitial testing was done on standard material with known gas permeability such as National Bureau of Standards, Standard Research Material 1470 (NBS, SRM 1470) using helium and oxygen as the permeating gasses. It was determined that the systematic error observed for oxygen and helium was 20% and 29%, respectively. Testing of GO films was done on top of transparency grade PET, since it is an affordable media and serves well as a testbed for testing formulations and composites. Figure 6.6 shows that uncoated transparancy grade PET has an oxygen permeability of 4.753 X 10^{-13} cm cm^3(STP) cm^{-2} s^{-1} $cmHg^{-1}$. This is based on a pressure rise in the downstream volume of our manometric setup at a rate of 1.15 mTorr/hr. Since the leak rate of the system is on the order of 1 - 3 mTorr/hr and the supporting substrate (PET) has a permeation rate of 1.15 mTorr/hr, this indicates that any additional barrier coating of graphene or GO on the surface of PET will inhibit the rate of permeability below the detection limit of our instruments, possibly to the point where we would not be able to distinguish between the leak rate and the permeation rate.

Gases with smaller kinetic diameter will have higher permeation rates. Helium, with a kinetic diameter of 2.65 Angstroms (Å), should have a higher permeation rate than oxygen (O_2) molecules, with a kinetic diameter of 3.46 Å, and since the end goal of the project is to evaluate water vapor permeability, which has a kinetic diameter of 2.65 Å, we have chosen to go with helium (He), diameter = 2.6 Å, as the permeating gas. Helium permeation for NBS, SRM 1470 is shown in Figure 6.7. Testing multiple samples of uncoated PET to helium revelaed that the system has less than a 2% deviation between samples of the same material (Figure 6.8).

6.3.2 Helium Permeability of GO/PET

We have also investigated thin films of GO coated on top of PET. In a typical procedure a 3 wt% dispersion of GO is diluted to the desired concentration and sonicated for 1.5 hours at 50 °C to exfoliate individual graphene oxide sheets. Then the dispersion is drop-cast onto the desired substrate and allowed to dry. Once the film has dried, it is loaded into the test cell with the GO film facing the upstream side of the testing apparatus. Using this technique we can achieve films of various thicknesses and transparencies.

Figure 6.9 shows overlaid plots of several permeation runs, consisting of GO coated PET with various thicknesses of GO coatings. The graph indicates a 756% improvement in retarding helium permeation for the red plot and as much as a 1252% reduction for the blue plot. The difference in the plots is the amount of GO that was drop-cast onto the PET. The red plot sample had 2.25 mg of GO drop-cast per 1 cm^2 of substrate surface area; whereas, the sample in the blue plot had 4.5 mg of GO/cm^2 of PET. At first sight there seems to be a linear dependance on permeability of He and amount of GO per surface aea of PET; however, more data are needed to draw such conclusions.

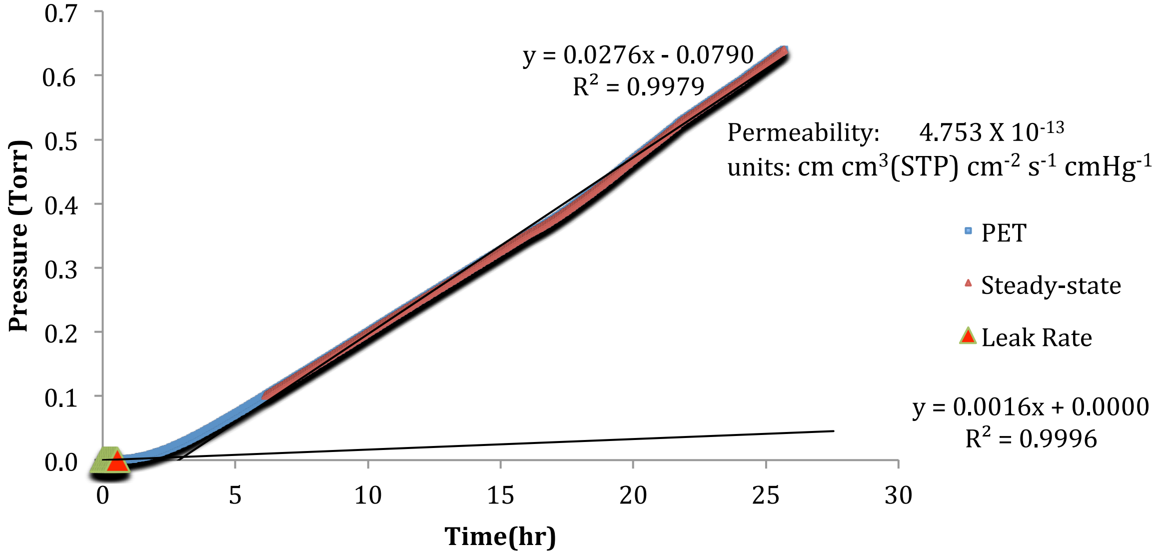

Figure 6.6 A graph of O_2 permeation through uncoated PET, resulting in a permeability of 4.753 x 10^{-13} cm cm^3(STP) cm^{-2} s^{-1} $cmHg^{-1}$. The black bottom line is the leak rate of the system.

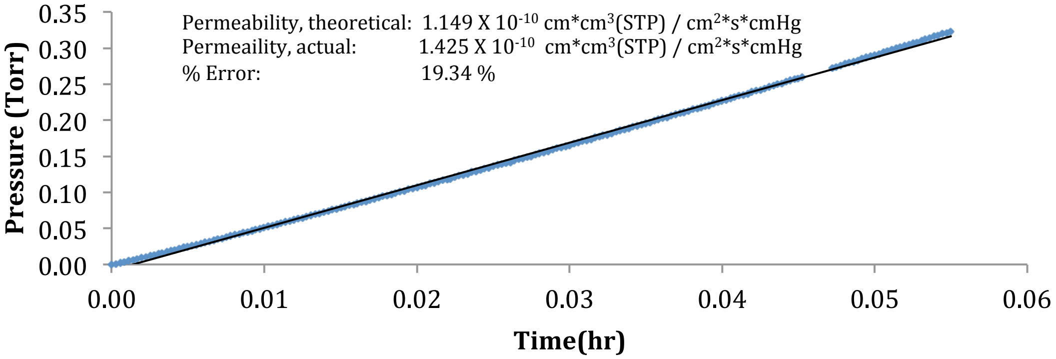

Figure 6.7 Graph of helium gas permeating through NBS, SRM 1470; note that a steady-state equilibrium is reached within minutes.

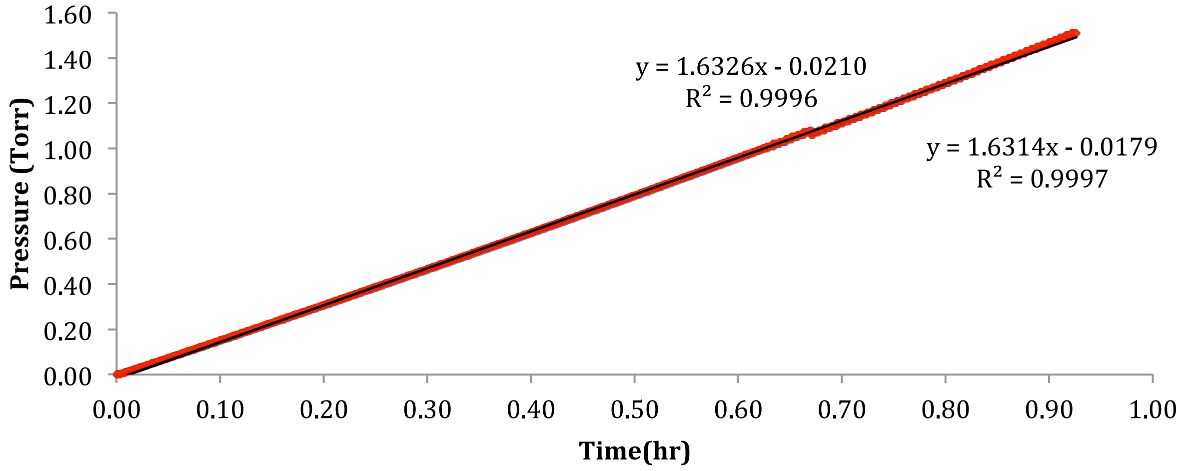

Figure 6.8 Graph of two plots of He permeability overlaid on top of each other indicating only a 2% deviation in sample to sample testing error.

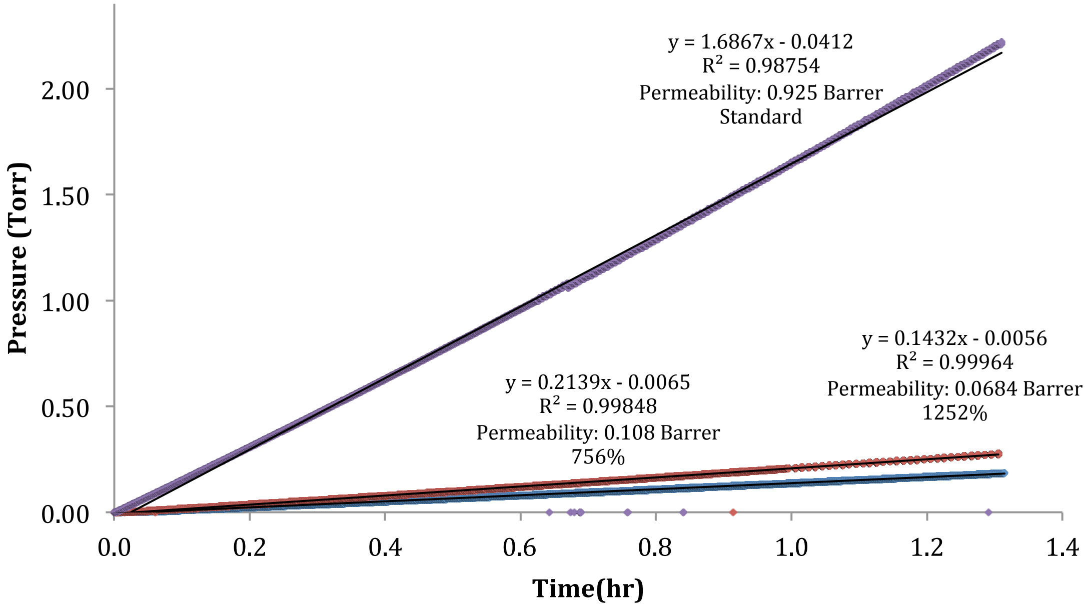

Figure 6.9 Graph of three plots of He permeability. The top (purple) graph indicaes 0.925 Barrer permeability of uncoated PET to helium. Where as 1 Barrer is defined as 1x10^{-10} cm cm^3(STP) cm^{-2} s^{-1} cmHg^{-1}. The red plot is a permeability of 0.108 Barrer and coresponds to the sample of PET coated with graphene oxide in the amount of 2.25 mg GO per 1 cm^2 of PET. The blue line is a PET sample coated with 4.5 mg of GO per 1 cm^2 of PET.

6.3.3 WVTR of GO/PET

We have also investigated the permeability of GO films to water vapor. Our initial testing was carried out on uncoated PET as shown in Figure 6.10. An uncoated PET film has a water vapor transport rate (WVTR) of 3.6 x 10^{-1} g/m^2 day. For comparison, the Mitsubishi supplied material (PET) has a WVTR of 5.0 x 10^{-1} g/m^2 day, making transparency grade PET a great test bed for rough measurements. Figure 6.10 also shows a second plot of PET covered with 1.7 μm of GO film. The resultant PET/GO composite yielded a WVTR of 2.9 x 10^{-1} g/m^2 day or a 21.4% improvement. By varying the thickness of the GO film on top of the PET, we were able to produce a set of samples with varying degrees of WVTR improvement. As can be seen from Table 6.1, the most dramatic change in WVTR occurs with just a 170 nm coating of GO; with thicker GO film coatings, the WVTR improvement tapers off. This is better represented visually by graphing WVTR vs. GO film thickness, as shown in Figure 6.11. In contrast to oxygen and helim, the WVTR of GO indicates that GO has limited use as a water vapor barrier. The likely reason for this is that GO is hygroscopic and inherently contains oxygen containing functional groups on the basal plane of the sheets. The oxygen containing functional groups can hydrogen bond to water molecules and may remain trapped within the GO layered structure even under a high vacuum environment. If one side of the GO membrane is exposed to 100% humidity, while the other side is kept under vacuum, the GO membrane can serve as a transport medium for water vapor, absorbing water from one side and immediately releasing into the other side, while water slowly propagates through the GO structure. In an effort to understand the rapid transport of water through a GO/PET membrane, we have also investigated the surface of the GO film after WVTR has been measured. Figure 6.12 shows an image from a scanning electron microscope (SEM), with the upstream side facing up in the image. The image clearly shows pitting of the GO film. The pitting is thought to originate from water permeating through GO defects in the film (Figure 6.12).

6.3.4 Hydrophobic Functionalization of GO

Hexamethyldisilazane (HMDS) is used industrially to render surfaces hydrophobic. It reacts with surface hydroxyl groups according to the mechanism shown in Figure 6.13. Reaction with surface hydroxyl groups is very slow at room temperature; however, the rate of the reaction can be increased dramatically when heated to 85 °C. It is also known that graphite oxide is thermodynamically unstable and will decompose and start losing surface water when heated. Therefore, control samples of pure GO/PET annealed at 85 °C were made in addition to HMDS treated samples of GO/PET. All samples were tested using ATR-IR and a contact angle goniometer. The contact angle of a water droplet on the surface of untreated GO/PET was 27.8°. Exposure of GO/PET to HMDS at a pressure of 300 Torr at 85 °C over a period of 24 hours increases the contact angle to 53.9° (Figure 6.14). However, when the experiment was repeated without the presence of HMDS, the contact angle recorded was 55.2°, which indicates that factors other than HMDS are the primary driving force for an increase in contact angle. We also discovered that heating GO/PET in a vacuum oven for 72 hours at 85 °C under an atmosphere of 1 Torr produced a contact angle of 70.5°.

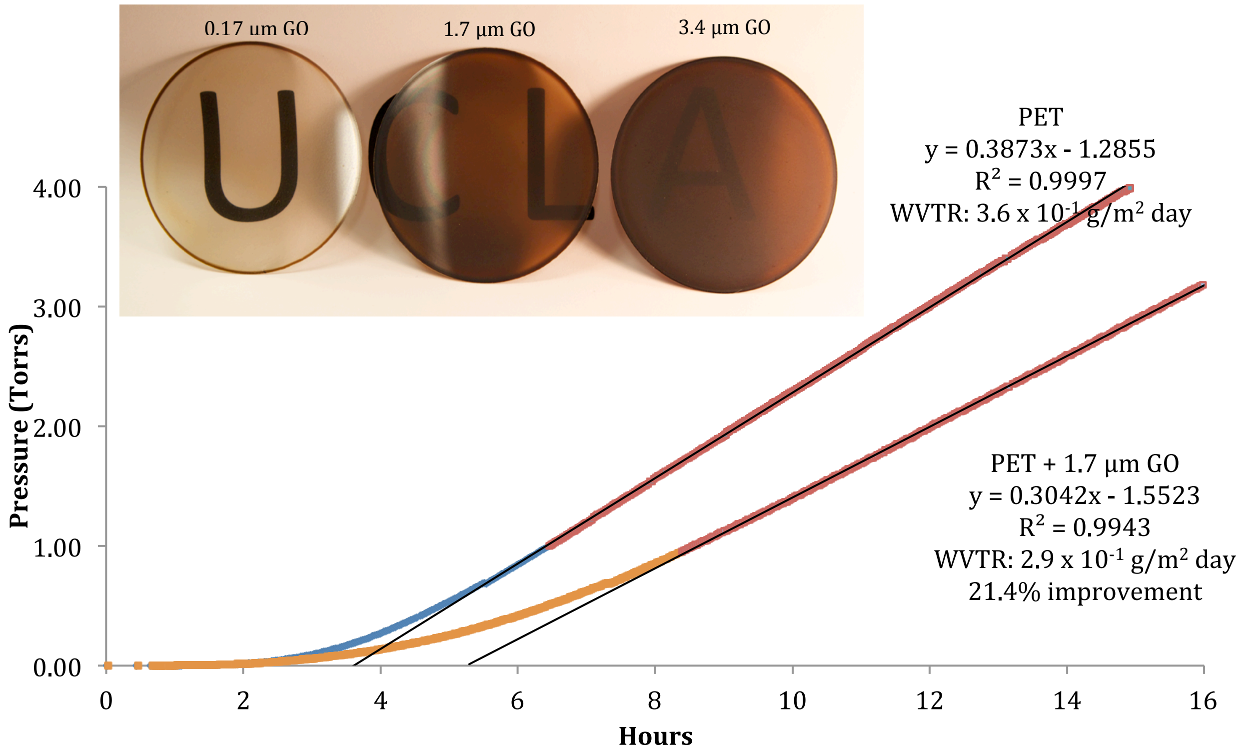

Figure 6.10 Plot of WVTR for PET and PET/GO, indicating a 21.4% improvement in barrier properties over a standard PET film using only a 1.7 micron thick GO film.

Table 6.1 WVTR of PET and PET/GO Composites

GO film thickness (µm)	WVTR (g/m^2 day)	Improvement (%)
17.00	0.1711	52.9%
10.20	0.2073	43.0%
5.10	0.2255	37.9%
3.40	0.2445	32.7%
1.70	0.2858	21.4%
0.85	0.2916	19.8%
0.34	0.3091	14.9%
0.17	0.3232	11.1%
0	0.3634	0%

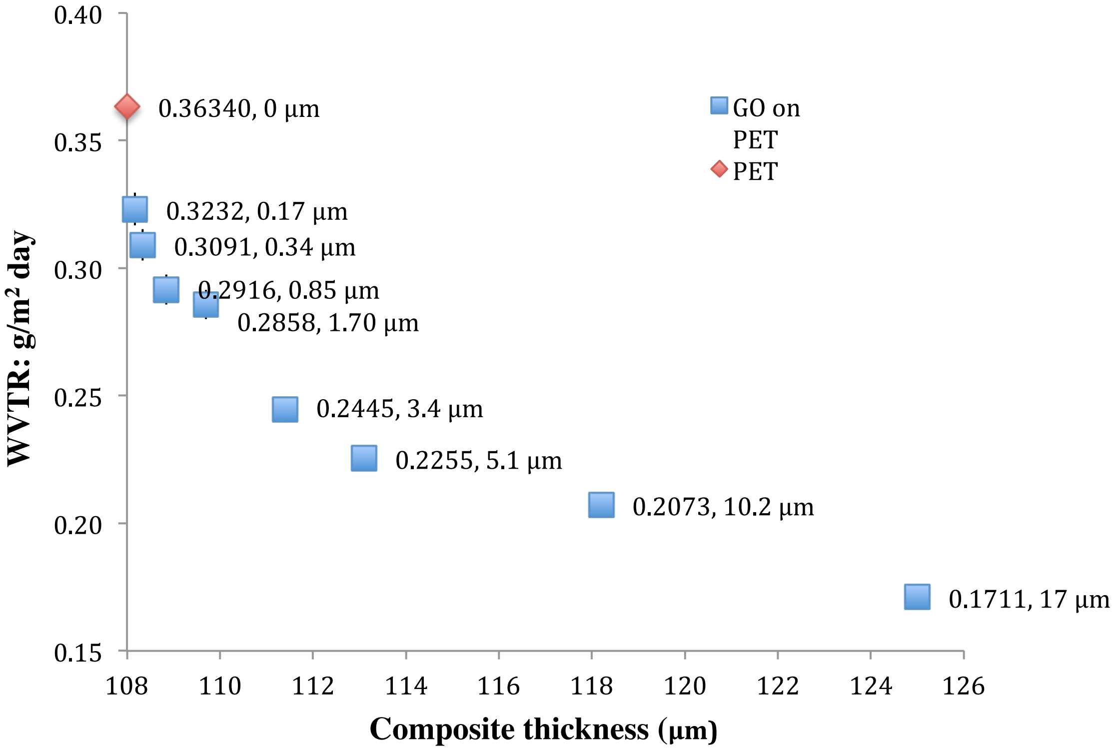

Figure 6.11 A plot of water vapor transmission rate (WVTR) as a function of GO film thickness from Table 6.1. The first value next to each datum point indicates the WVTR, while the second is the thickness of the GO film.

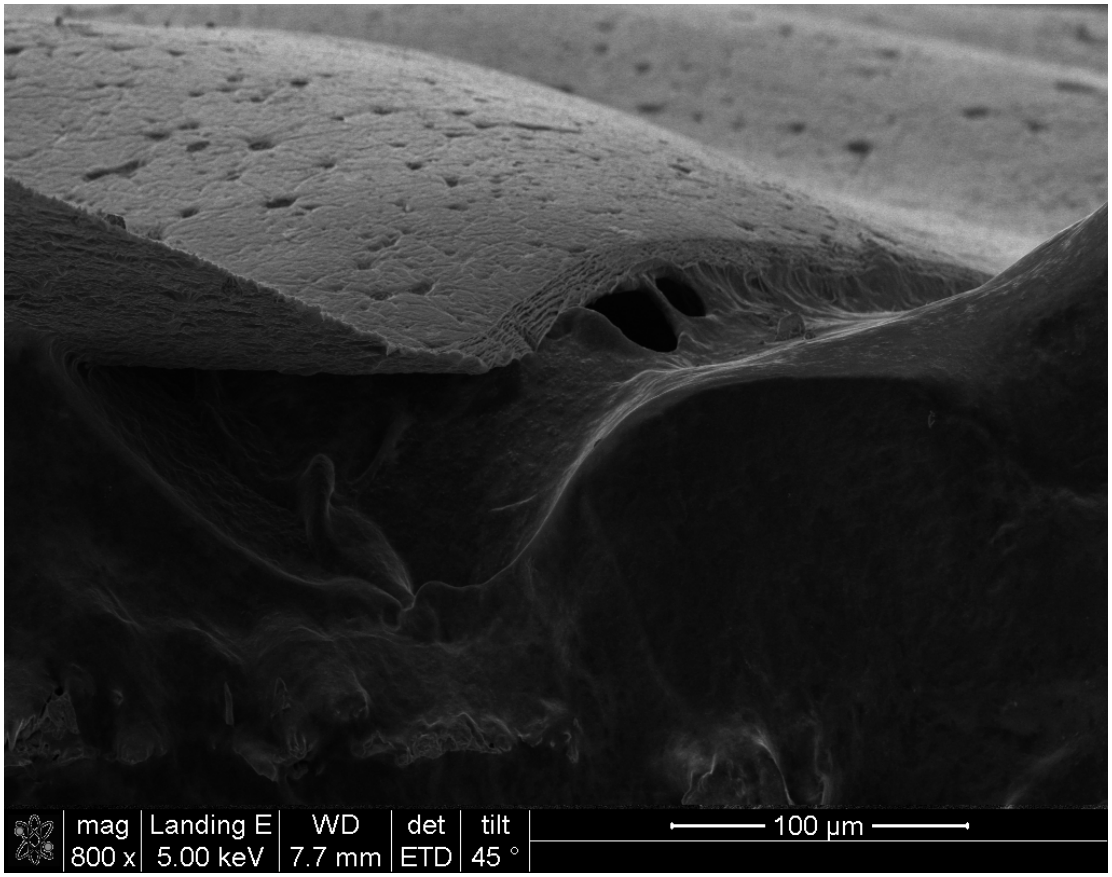

Figure 6.12 A scanning electron microscope (SEM) image shows an interesting surface morphology of the upstream side of the GO/PET membrane after WVTR testing. The pitting is thought to originate from water permeating through GO defects in the film.

At this point it is worth noting that the contact angle of graphite is close to 90° [10], while the reported contact angle of GO is on average 30 - 50° [11] owing to the number of functional groups on its surface and the amount of water intercalated between the sheets. It would appear that thermal dehydration/deoxygenation is primarily responsible for a change in the contact angle.

To further confirm out theories and about thermal processing and a change in contact angle, we have analyzed the samples of GO using ATR-IR (Figure 6.15) and have found no peaks corresponding to the reaction of HMDS with hydroxyl groups. If HMDS has bonded to GO there would be new peaks at 1260 cm^{-1} (Si-CH_3 symmetric deformation), 2800-3000 cm^{-1} (C-H stretching vibration), and 1100 cm^{-1} (Si-O asymmetrical stretching vibration); however, either those peaks are buried behind overlapping peaks from GO or the reaction simply didn't occur for a number of possible reasons.

One solution to reveal overlapping peaks from ATR-IR is to use GO/PET as a background in ATR-IR when analyzing HMDS treated samples. Additionally X-ray photoelectron spectroscopy (XPS) is a highly sensative surface analysis instrument which can be used to determine the presence of C-Si bond and both experiments have been planned for future studies. An alternative chemical is a fluorinated chlorosilane, which may lead to better rates of reaction and higher product thermodynamic stability.

Even though functionalization of GO using HMDS was unsuccessful, we have succeeded in changing the contact angle of GO, which may provide us with an increase in retardation of water permeation. By annealing GO films at higher temperature we may achieve a higher contact angles, more hydrophobic surfaces, while still retaining the GO laminar structure.

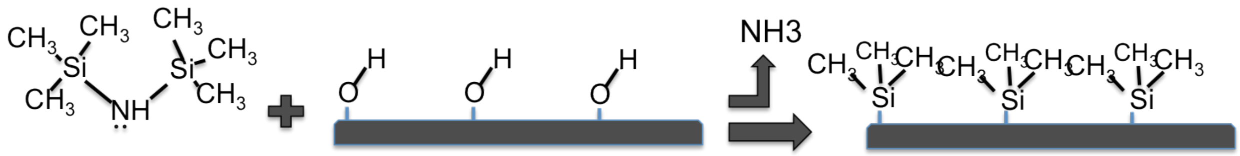

Figure 6.13 A mechanism for the reaction of HMDS with the surface functional groups on graphite oxide (GO).

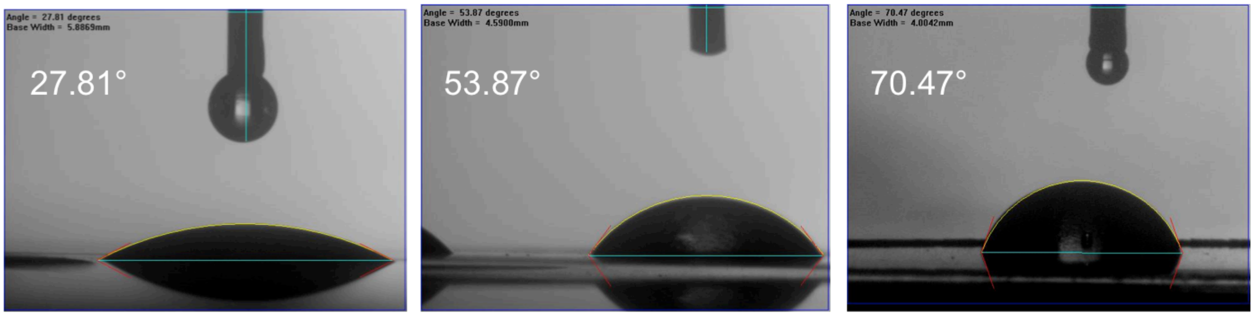

Figure 6.14 Photographs of contact angle measurements. From left to right: Untreated GO, 24 hr annealed GO, 72 hr annealed GO.

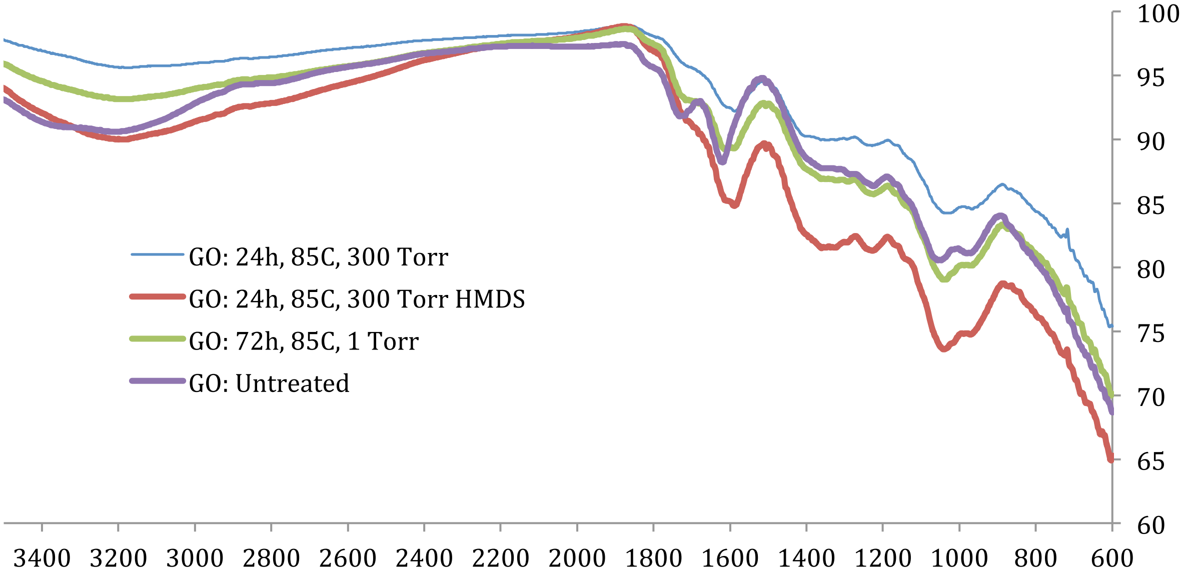

Figure 6.15 ATR-IR overlay spectra of GO treated under various conditions.

6.3.5 WVTR of Graphene/PET

Using the method described above and previously published,[12] we have been able to successflully grow a single layer of graphene on a 3” Cu substrate and have transferred it onto a PET substrate as shown in Figure 6.16. As can be seen from Figure 6.16, when graphene is transferred onto PET it can have significant defects as indicated by the blue arrow and brackets. The diameter of the hole highlighted by the blue arrow is on the order of 7 mm. Even though the sample is riddled with defects, we went ahead and performed a water permeation study on it and found it was still able to improve, i.e. decrease the permeability of water by 10% or 0.3285 g/m^2 day. To put this into perspective, PET coated with a single layer of graphene, 0.0034 micrometers thick, yielded the same water vapor transmission rate (WVTR) as a 60 times thicker graphite oxide coating on a PET substrate; hence, graphene is an extremely good barrier for water considering its thickness.

To address the number of defects introduced into graphene sheets during transfer, we have also investigated a different transfer, which is a more direct route to produce graphene on a polymer substrate. We have focused on a UV-curable polymer as the substrate of choice. First, a liquid, polyurethane-based, UV-curable polymer was spin-coated onto the graphene grown on copper to form a thin protective layer (Figure 6.19). Next, a much thicker layer was deposited using either a doctor blade or drop-cast using the same or a different polymer, as the initial layer already resides directly on the graphene. The staging of polymer deposition is necessary to prevent any unwanted polymer sliding under the graphene or copper layer which would prevent effective copper etching. The resulting Cu/polymer substrate can then be used directly to test the effects of graphene on the WVTR as compared to the polymer control.

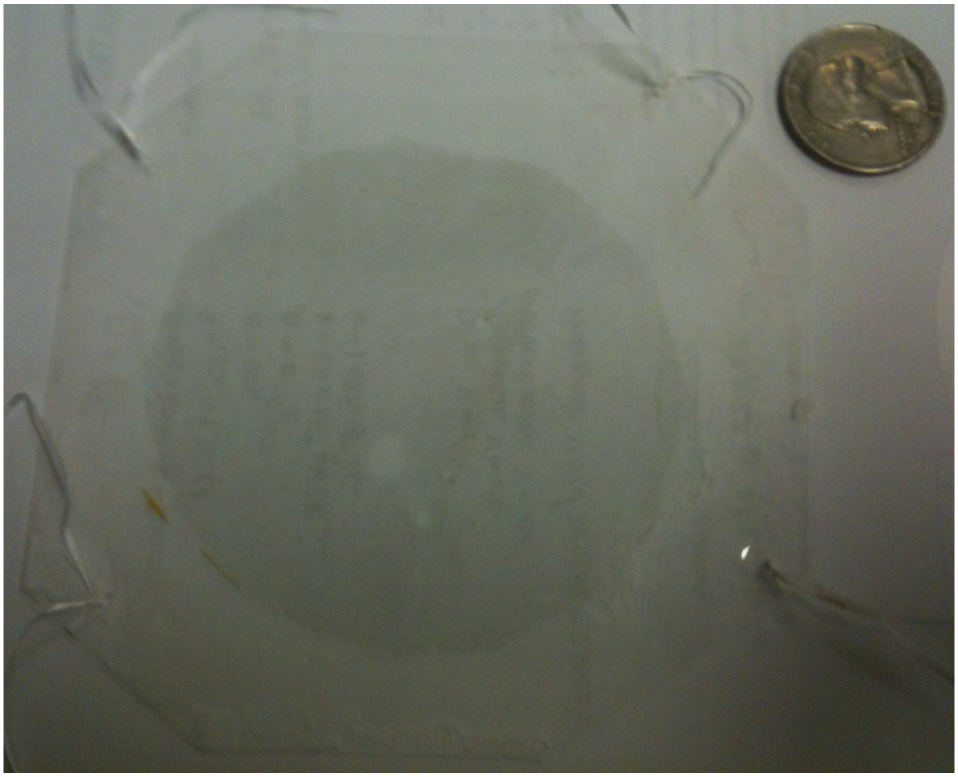

Figure 6.16. Photograph of an octogonal shaped piece of PET with a 3” circular deposit of atomically thin graphene. The layer is only 1 atom thick, but since it attenuates 2.3% of visible light, it can be seen with the naked eye under certain contrast conditions. A quarter placed in the top right corner is for size reference.

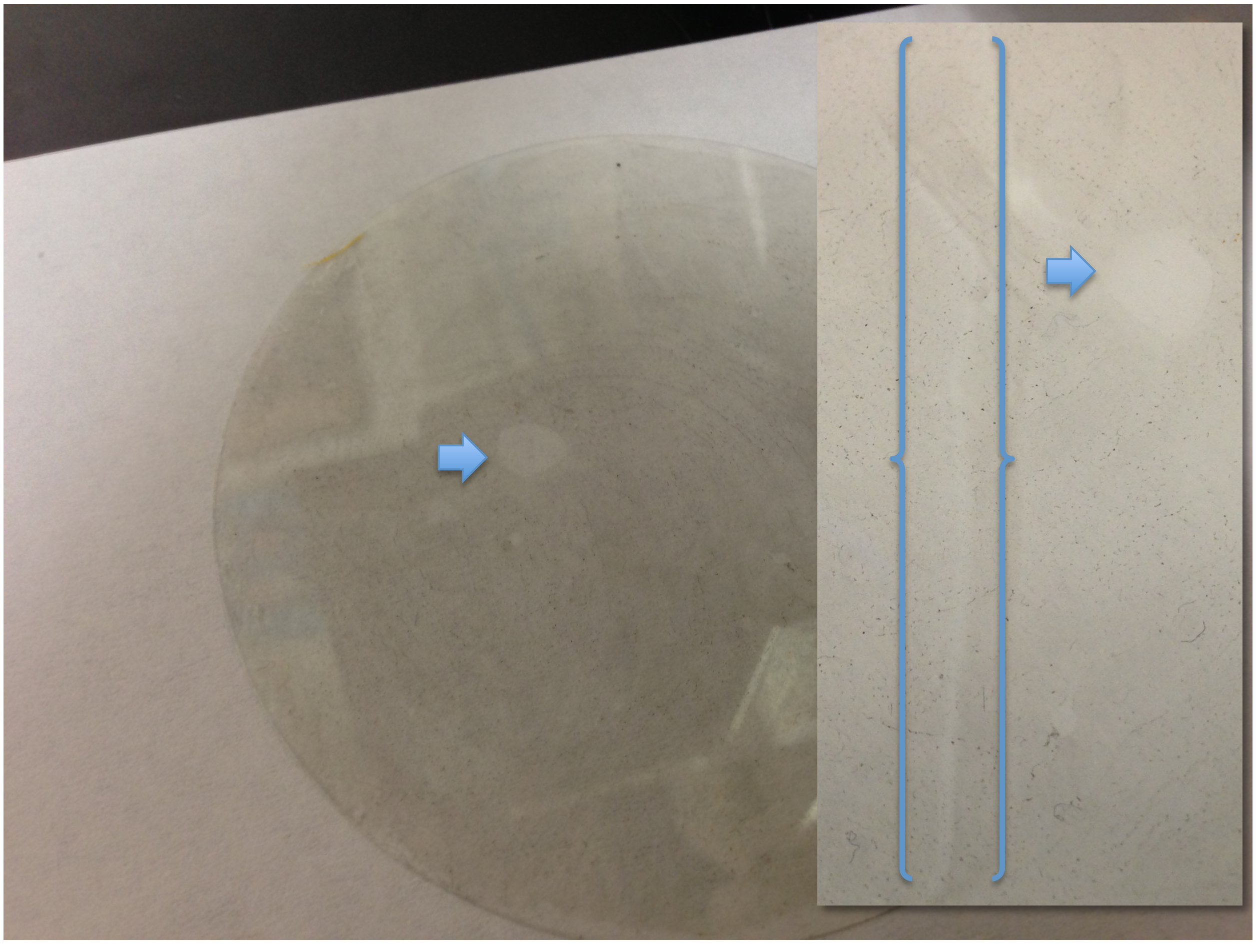

Figure 6.17 3” Graphene film on top of a PET substrate, arrows and brackets indicates holes and defects due to transfer.

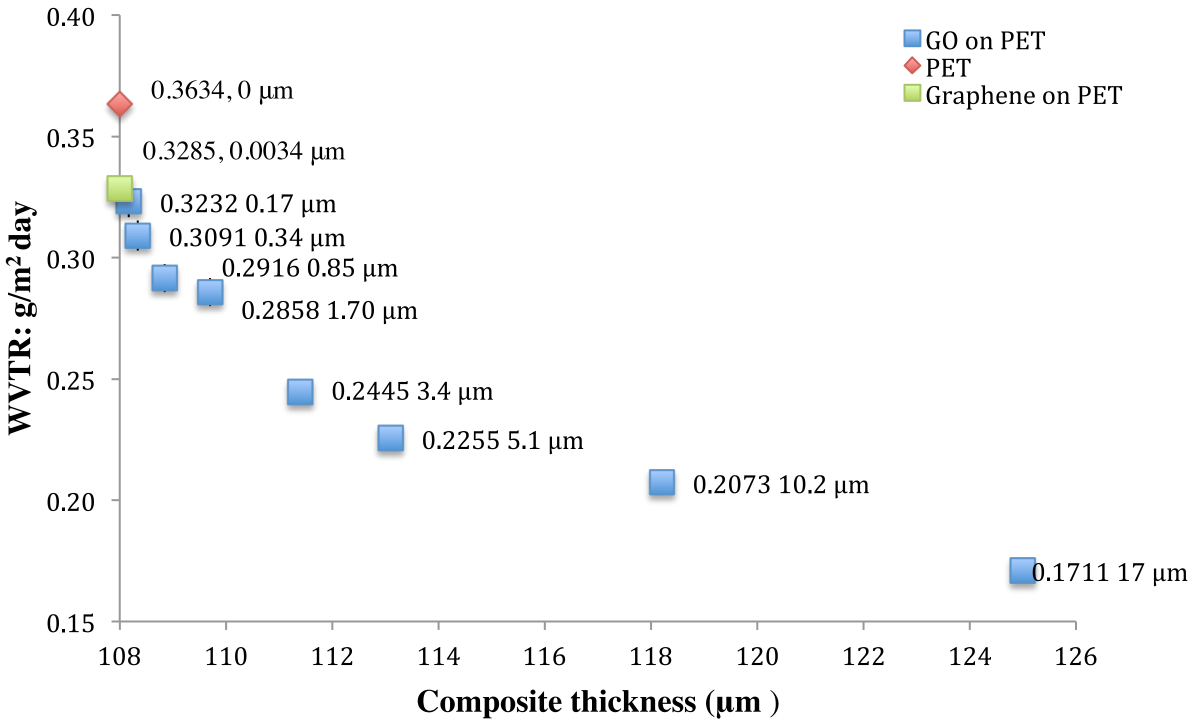

Figure 6.18 A plot of water vapor transmission rates as a function of graphene coated PET and graphite oxide coated PET film thickness. The first value next to each datum point indicates the WVTR, while the second is the thickness of the GO film.

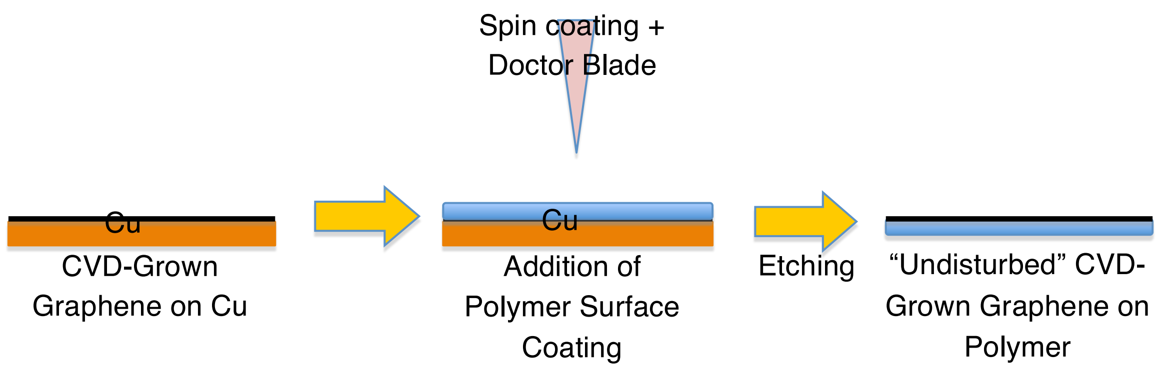

Figure 6.19 Schematic illustration of the new transfer method developed for moving CVD-grown graphene to a polymer support, while maintaining good mechanical integrity.

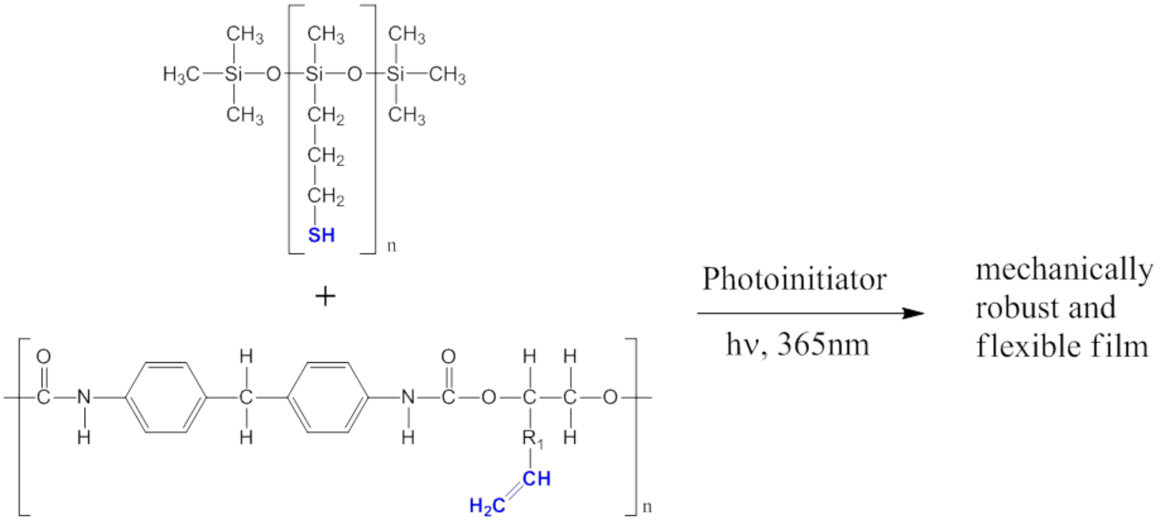

Figure 6.20 A drawing of the chemical formula for the UV-curable polymer used in this study. The clear polymer solidifies and cures in under an hour producing a rigid support.

We have experimented with the UV-curable polymer shown in Figure 6.20, which has been provided by Dr. Jeff Gerbec (UCSB). Our initial experiments to characterize the film using Raman spectroscopy were inconclusive since the Raman absorption of graphene and the underlying substrate are quite similar (Figure 6.21). However, upon closer inspection of the UV-cured polymer when used as a substrate to "fish out" the floating graphene on the surface of water, we have been able to confirm that CVD graphene and UV-cured polymer have two Raman peaks that can be used to identify graphene on the polymer. In particular, the graphene G and 2D bands at ~1600 cm^{-1} and ~2700 cm^{-1}, respectively, can be used as a fingerprint for graphene on the polymeric material as can be clearly seen in Figure 6.21.

Several of the PET/bilayer graphene samples were tested at Illinois Instruments to determine their WVTR. 3M transparency grade PET, tested as received has a WVTR of 4.4 g/m^2 day, while bilayer graphene samples show 3 g/m^2 day; all samples were tested in duplicates as shown in Figure 6.22. Our initial assessment suggested that the test may be flawed and water permeates through the adhesive layer in the aluminum mask used to mount the samples in the test cell. However, testing of the PET provided by Mitsubishi Plastics revealed a WVTR of 0.15 g/m^2 day, consistent with the 10^{-1} g/m^2 day value measured by Mitsubishi. These results indicate that the adhesive on the aluminum mask is indeed doing its job and not an issue at the current WVTR rates. We then turned to our graphene as a next possible culprit and wanted to investigate the number of defect sites in a graphene layer before transfer takes place. What we have discovered is that our graphene is not defect free as can be seen in Figure 6.23.

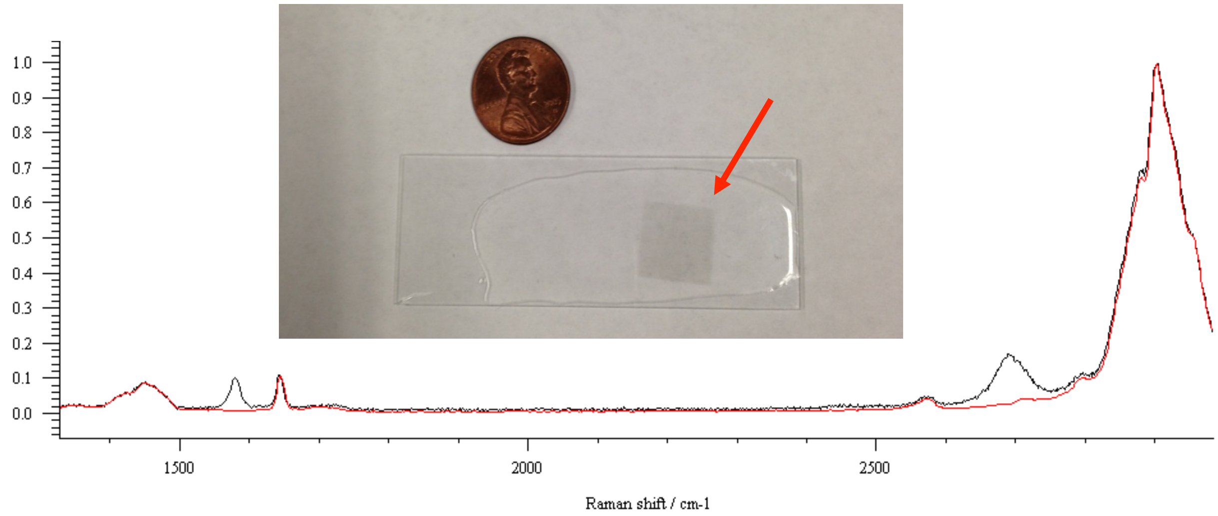

Figure 6.21 Top: A photograph of the UV-cured polymer containing a single layer of graphene. **Bottom:** Raman spectroscopy showing the high degree of overlap for peaks from the UV-cured polymer and CVD-graphene. However, using the G and 2D bands of graphene at ~1600 cm^{-1} and ~2700 cm^{-1}, respectively, we can confirm the presence of both graphene and the polymer.

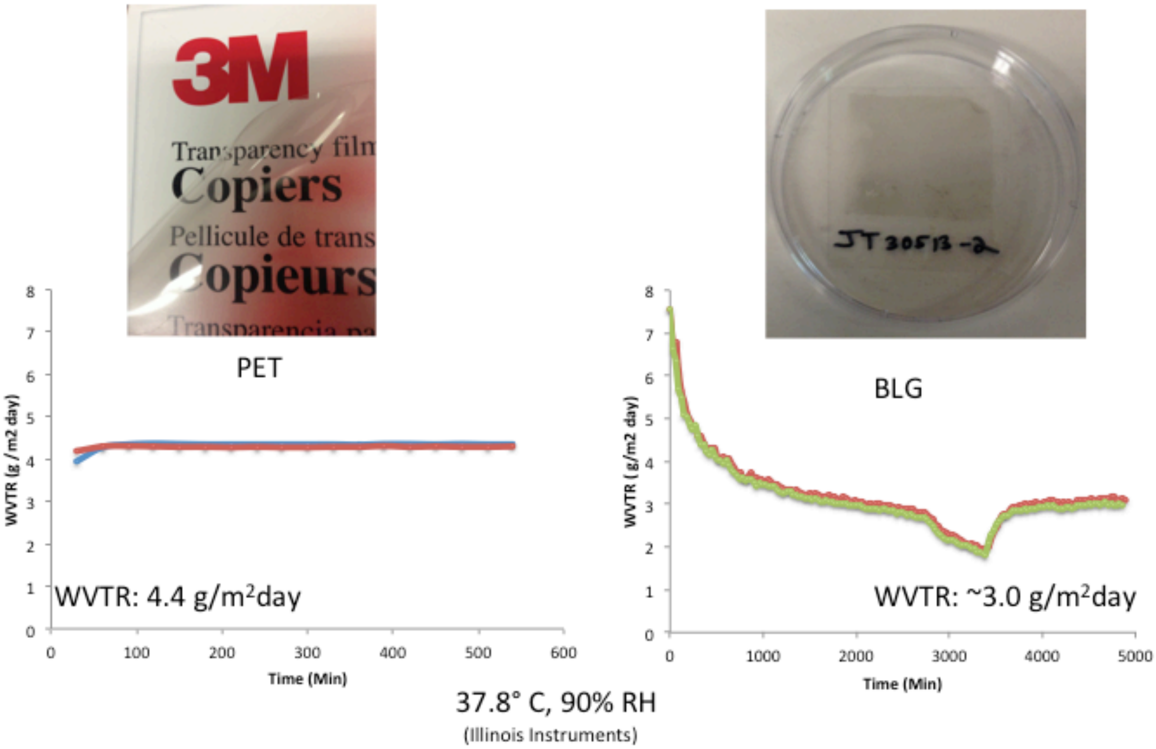

Figure 6.22 A plot of water vapor permeation rate (WVTR) through an uncoated ~100 micrometer PET sheet (left) and a WVTR of the same grade PET coated with bilayer graphene.

A series of scanning electron microscope (SEM) images reveal that dramatic fragmentation of the graphene sheet has occurred. A perfect sheet of graphene would show a uniform dark gray image; however, all our images contain a light shade of gray trenches in the graphene indicating the presence of the underlying copper substrate. Furthermore, where copper shows through, there is always a presence of insulating nanoparticles. We believe that these nanoparticles, ranging from 50 - 100 nm in size, are copper oxide. The source of this contamination is an air leak in the system or residual chemical contamination.

In pursuit of measuring the WVTR of pristine graphene, we have modified the permeation setup further to be able to measure domain sizes as small as a pinhole in graphene. In the past, a sample with PET was to be coated with graphite oxide (GO) or graphene and sandwiched between two steel plates with Viton o-rings making an airtight seal. The problem with this setup is: 1) a large sample requirement (3”) and 2) as the Viton o-ring is compressed, it expands its contact path with the material to be tested, potentially “rubbing away” at the material to be tested and introducing defects radially at the O-ring sample interface. To circumvent both of these problems we have implemented a new mounting system, in which two pieces of aluminum foil are die cut to 3” in diameter, while the inside of the foil is die cut to a 1.5” opening. Using a 5 min epoxy, we then coat the inside of both foils and sandwich the test sample between the foils for 24 hours. The technique may allow us to test permeability through a sheet as little as 500 μm in lateral dimensions, which is exciting since it is possible to grow single grains of graphene on the order of 500 μm, therefore enabling an understanding of the effects of grain boundary defects on permeability.

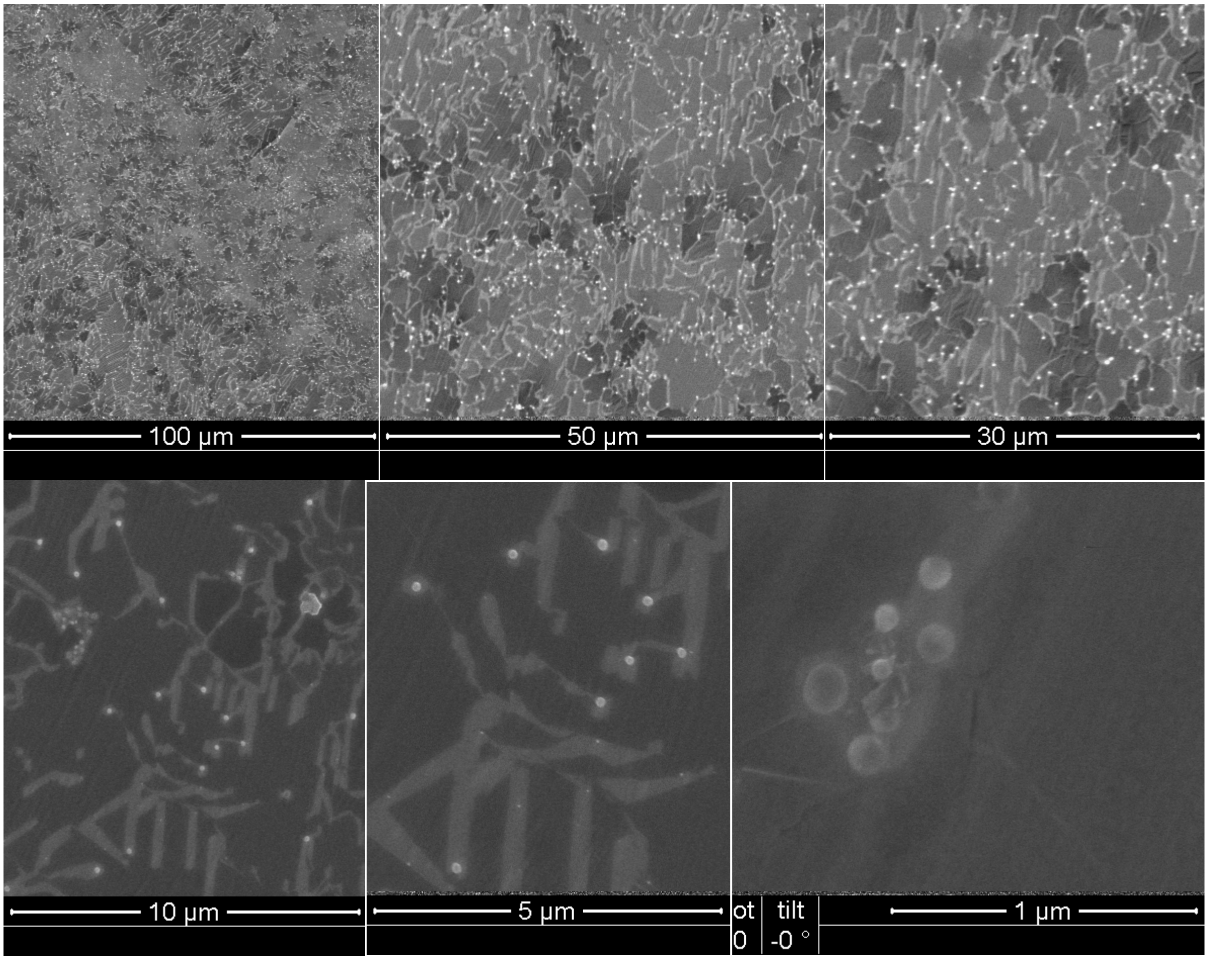

Figure 6.23 A series of photographs from a scanning electron microscope (SEM) of as-grown graphene on Cu foil. Starting from a zoomed out 0.1 mm (top left) scale through a nanometer scale we can observe fragmentation of a graphene sheet as well as decoration of graphene-free regions with impurity nanoparticles.

6.4 Conclusions

In summary, we have been able to achieve more than three orders of magnitude in retardation of helium permeation across PET by coating it with a 17 μm thick layer of graphite oxide. Barrier properties of GO/PET to helium and other gases at STP may be simply controlled by changing the thickness of the GO coating. Excellent barrier properties of graphite oxide may stem from the intrinsic structure of this two-dimensional material. Unfortunately, the same intrinsic properties that allow GO/PET to be such an excellent barrier to gases at STP, also hinder its ability to stop water permeation, which occurs by simple water displacement of molecules from one side to the other. We have also been able to show that graphene is at least a 60 times better barrier material when the thickness of the membrane is considered.

6.5 References

1. Park, J.; Chae H.; Chung, H. K.; Lee, S. I. *Semicond. Sci. Technol.* **2011**, *26*, 034001
2. Wang, Z. B.; Helander, M. G.; Qiu, J.; Puzzo, D. P.; Greiner, M. T.; Hudson, Z. M.; Wang, S.; Liu, Z. W.; Lu, Z. H. *Nature Photonics* **2011**, *5*, 753 – 757
3. Mitsubishi Plastics Inc, View-Barrier©
4. Lewis, J. S.; Weaver, M. S. *IEEE J. Sel. Top. Quantum Electron* **2004**, *10*, 45
5. Wassei, J. K.; Kaner, R. B. *Acc. Chem. Res.* **2013**, *46* (10), 2244 – 2253
6. Chen, S.; Brown, L.; Levendorf, M.; Cai, W.; Ju, S. Y.; Edgeworth, J.; Ruoff, R. S. *ACS Nano* **2011**, *5* (2), 1321 – 1327.
7. Reed, J. C.; Zhu, H.; Zhu, A. Y.; Li, C.; Cubukcu, E.; *Nano Lett.* **2012**, *12* (8), 4090 – 4094.
8. Kovtyukhova, N. I.; Ollivier, P. J.; Martin, B. R.; Mallouk, T. E.; Chizhik, S. A.; Buzaneva, E. V.; & Gorchinskiy, A. D. *Chem. Mat.* **1999**, *11* (3), 771 – 778.
9. Burnett. E. S. *J. Appl. Mech.* **1936**, *3*, 136 – 140
10. Taherian, F.; Marcon, V.; van der Vegt. N. F. A. *Langmuir* **2013**, *29* (5), 1457 – 1465
11. Xue, Y.; Liu, Y.; Lu, F.; Qu, J.; Chen, H.; Dai, L. *J. Phys. Chem. Lett.* **2012**, *3* (12), 1607 – 1612
12. Wassei, J. K.; Mecklenburg, M.; Torres, J. A.; Fowler, J. D.; Regan, B. C.; Kaner, R. B.; Weiller B. H. **2012**, *8* (9), 1415 – 1422

Chapter 7

One-step Synthetic Approach to Graphene Metal/Metal Oxide Nanocomposites for Supercapacitors and Catalysis Applications

7.1 Introduction

Graphene, a two-dimensional, sp^2 hybridized sheet of carbons with one atom thickness, is the thinnest material in the universe.[1] Graphene has a theoretical surface area of 2630 m^2 g^{-1} and a thermal conductivity of 5000 W m^{-1} K^{-1}.[2] Graphene also exhibits the highest known electrical conductivity at room temperature of 10^6 S/cm.[3–6] The unique structure and properties of graphene as well as fast paced developments in graphene research may offer great potential in the fields of electronics, optoelectronics, and electrochemical applications.[6-11] However, pure graphene sheets are limited for many applications despite their excellent characteristics. For example, the capacitance of graphene is limited by the electrochemical double-layer and is relatively low. Therefore large-scale practical applications of graphene could benefit from enhanced functionalities added to the pure graphene sheets.

Metal oxide nanoparticles are of great interest because of their unusual properties and have been widely used to decorate CNTs to form a new class of composites. For instance MnO_2

nanoparticles display a high specific capacitance of 1029 F/g, but by themselves are insulating and must be supported on a conducting substrate of suitable porosity and surface area. Similarly, NiO, and Co_3O_4 exhibit high specific capacitance, but need a high surface area and highly conducting support for supercapacitor applications. Noble metal nanoparticles are also of particular interest, for instance, Pd(0) nanoparticles have been shown to be extremely efficient in as a catalyst in Suzuki coupling reactions, while Ag(0) on graphene has been shown to useful for surface enhanced Raman spectroscopy (SERS)[12, 13]

To address the challenges in graphene applications, it is possible to combine graphene with a metal or metal oxide nanoparticle (NP), creating a hybrid graphene nanocomposite, with enhanced properties. There are generally two routes one can take when making graphene/NPs composites. The first approach relies on mixing graphite oxide in solution with the NP precursor and followed by simultaneous reduction to form a graphene/NP nanocomposite. This is a one-step approach that is both quick and efficient; however, due to non-homogeneous nucleation of particles, wide particle distribution is usually achieved.[14, 15] In the second approach, graphene and NPs are prepared by reducing graphite oxide and metal precursors separately and then a nanocomposite is made by combing the two.[16 - 18] Compared to the one-step synthesis, the size and distribution of the metal NPs can be precisely tailored to the desired specifications. However, due to the loss of functional groups, graphene sheets readily aggregate in solution, which leads to a non-uniform distribution of the nanoparticles on the surface of the graphene, and loss of loading. Both methods also suffer from poor nanoparticle adhesion to the graphene substrate since they synthesis is performed in solution.

Our group has demonstrated a light initiated, non-solution based approach to reduction of graphene oxide using a laser to form laser scribed graphene (LSG).[19] More recently Kim et al., has demonstrated a proof-of-concept where graphite oxide was mixed with metal nanoparticle precursors and initiated deflagration of graphite oxide by heating it with a soldering iron.[20] Their group reports excellent particle size distribution and adhesion to graphene, even after sonication. Although the authors reported that their reactions were done in air as well as in a nitrogen glove box, they strongly discourages reactions outside of the nitrogen glove box, as they are highly energetic when initiated with a soldering iron. Here, we present a one-step synthetic approach to graphene metal/metal oxide nanoparticle composites. Using a low-power infrared laser found inside a LightScribe DVD drive, we were able to initiate reduction of graphite oxide mixed with NP precursors. When the laser light hits the graphite oxide layer, reduction takes place, creating laser scribed graphene (LSG), in the process, the energy released is used to drive a side reaction reducing the NP precursor. To our knowledge this is the first report of a laser induced cascade reaction.

7.2 Experimental

7.2.1 Solution Preparation

Graphite oxide (GO) was synthesized using a modified Hummers method. In order to generate a stable GO colloidal dispersion, 3 wt.% slurry of GO was diluted with water to achieve a 3 mg/ml concentration and sonicated at 50 °C for 60 min using a VWR Ultrasonic Cleaner (B2500A-DTH, 210W). Stable dispersions of GO with silver acetate, CH_3COOAg (85140, Sigma-Aldrich), nickel (II) acetate tetrahydrate, $Ni(OCOCH_3)_2{\cdot}4H_2O$ (72225, Sigma-Aldrich), manganese (II) acetate tetrahydrate, $(CH_3COO)_2Mn{\cdot}4H_2O$ (221007, Sigma-Aldrich), copper(II) acetate monohydrate, $Cu(CO_2CH_3)_2{\cdot}H_2O$ (217557, Sigma-Aldrich), palladium acetate, $Pd(OAc)_2$ (205869, Sigma-Aldrich) and palladium trifluoroacetate, $Pd(TFA)_2$ (299685, Sigma-Aldrich) were made by first creating a dispersion of GO in water and then adding a concentrated solution of metal salt to achieve resulting concentrations of 3 mg/ml GO and either 0.1 or 1 mg/ml metal salts. Approximately 16 ml of GO with metal salt dispersions were drop-cast onto polyethylene terephthalate (PET) (PP2950, 3M), which was fixed to the LightScribe DVD disc using a spray adhesive glue (70-0050-1482-7, 3M).

7.2.2 Instrumental Analysis

XPS spectra were recorded using a Kratos Axis Ultra DLD spectrometer. TEM samples of the graphene/nanoparticle composite were prepared by mechanically transferring some of the laser-scribed material onto carbon-coated TEM grids. The TEM images and SAED patterns were collected on a FEI Tecnai G2 TF20 TEM operated at 200 kV. The HRTEM and SAED data were analyzed using EMMENU4 and ImageJ. The d-spacing values extracted from SAED were calibrated with an aluminum standard. SEM was performed on FEI Nova 230.

7.2.3 Electrochemical Measurements

Sandwich type devices made from NiO LSG electrode material with 6 M KOH electrolyte and a polypropylene separator were tested for their electrochemical behavior using a Biologic VMP3 potentiostat at room temperature. The voltage window used for all measurements is -0.1 to 0.6 V.

7.2.4 Suzuki-Miyaura Coupling with LSG/Pd(0)

Digestion of LSG/Pd: 2.5 mg of graphene was weighed out in a 20 ml vial with 5 ml concentrated nitric acid. The solution was covered and left heated at 100 °C until the whole liquid volume of the vial became a homogeneous solution. Once the solution cooled, it was transferred into a 25 mL volumetric flask. The flask was covered to the fill mark by adding 5% nitric acid and then shaken. The solution was then poured into a plastic vial for ICP-OES testing.

Phenyl boronic acid (1.25 eq), sodium hydroxide (4 eq), and bromobenzene (1 eq) were added to a round bottom flask. 5 mL of ethanol and 5 mL of water were then added to the flask. 10 mg (0.24% Pd) of the palladium/graphene composite was added next and the solution was put into an oil bath at 80 °C. After the reaction, the solution was allowed to cool to room temperature. The organic product was extracted by washing with (3 x 10 ml) dichloromethane. The organic layers were then combined and dried over magnesium sulfate and dried using a rotovap. Analysis of product was carried out by NMR.

7.3 Results and Discussions

7.3.1 Mechanism of formation

When a 788 nm laser encounters the surface of graphite oxide it causes deflagration and results in laser-scribed graphene (LSG).[19] The reaction is self-propagating, and exothermic, reaching temperatures in excess of 400 °C. The energy generated during deflagration can be used to drive a side reaction such as the reduction of the metal nanoparticle precursor, homogeneously dispersed in the graphite oxide film. Mixing graphite oxide with a salt such as a metal acetate enables us to create dispersions of graphite oxide with metal acetate dispersed on an atomic scale. The dispersions are stable for up to several months with no visible agglomerates formed in metal salt concentrations up to 1 mg/ml. Higher concentrations of the nanoparticle precursor are possible, but their long term stability is hindered. For instance, a concentration of 35 mg/ml of metal salt in solution will result in flocculation of graphite oxide within a day. It is, however, still possible to make higher loadings of LSG nanocomposites if solutions are used right away. We have experimented with acetate salts of Manganese (II), Cobalt(III), Iron (III), Silver(I), Palladium (II), Nickel (II), and Copper(II). After laser scribing, the products they formed on the surface of LSG were identified as: MnO, Co_3O_4, Fe_2O_3, Ag(0), Pd(0), NiO, Cu_2O respectively. It is also possible to tailor the resulting oxides of the nanoparticles, based the ligands they are attached to. For instance, reduction of manganese acetate leads to the formation of MnO, while manganese nitrate will result in MnO_2. Furthermore, if laser scribing were performed in an inert vacuum or in a nitrogen rich environment, this would affect the resulting product as well. The difference lies in the mechanism of thermal decomposition of these compounds and is beyond the scope of this paper. However, using this information one can tailor the LSG nanoparticle composites to the desired application, with a possibility of using almost all elements in the periodic table.

7.3.2 Analysis by Electron Microscopy

As can be seen in Figure 7.1, as the LightScribe laser moves across the surface of a coated DVD disc, it creates trenches in the resulting LSG/NiO nanocomposite. The trenches are the product of gases escaping from the laminar structure of graphite oxide. Localized heating, generated during the GO deflagration reaction, fuels the thermal decomposition of nickel acetate tetrahydrate surrounding the GO sheets resulting in nanoparticles (Figure 7.1, inset). The concentration of nanoparticles appears to be homogeneous from one side of the trench to the other; however, SEM analysis taken between trenches, and within sheets needs to be carried out to confirm the presence of nanoparticles within the sheets as well. Comparable SEM images can be observed for films of LSG with Ag and Pd nanoparticles – see Figure 7.2 and Figure 7.3, respectively.

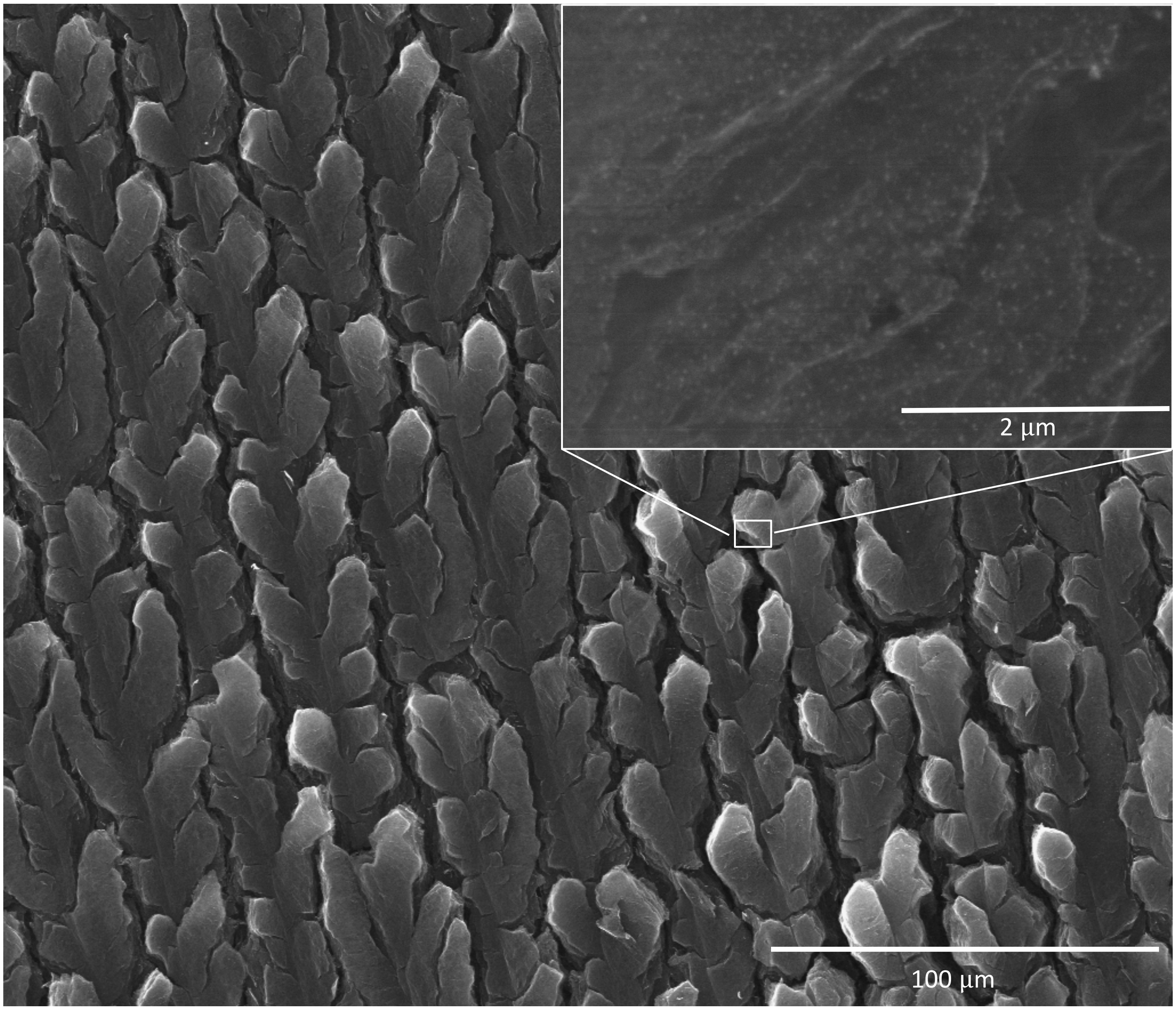

Figure 7.1 Shows a 1,000x magnification scanning electron microscope (SEM) image of a laser-scribed graphene (LSG) sample decorated with nickel oxide (NiO) nanoparticles. The inset shows a 50,000x-magnified view of LSG covered with insulating NiO nanoparticles.

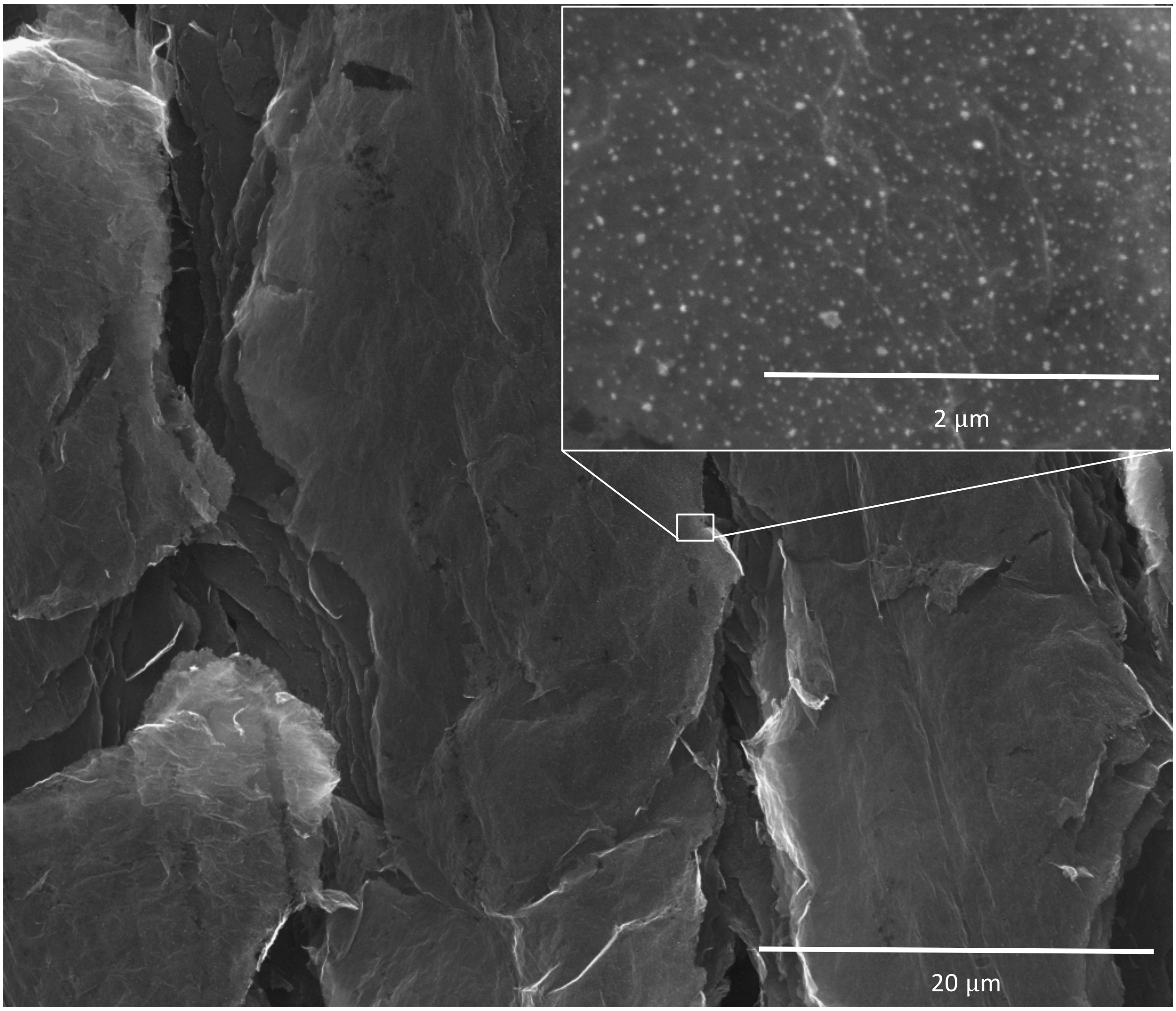

Figure 7.2 A 5,000x magnified scanning electron microscope (SEM) image of laser scribed graphene (LSG) decorated with Ag(0) nanoparticles. The inset shows a 50,000x-magnified view of graphene covered with insulating NiO nanoparticles.

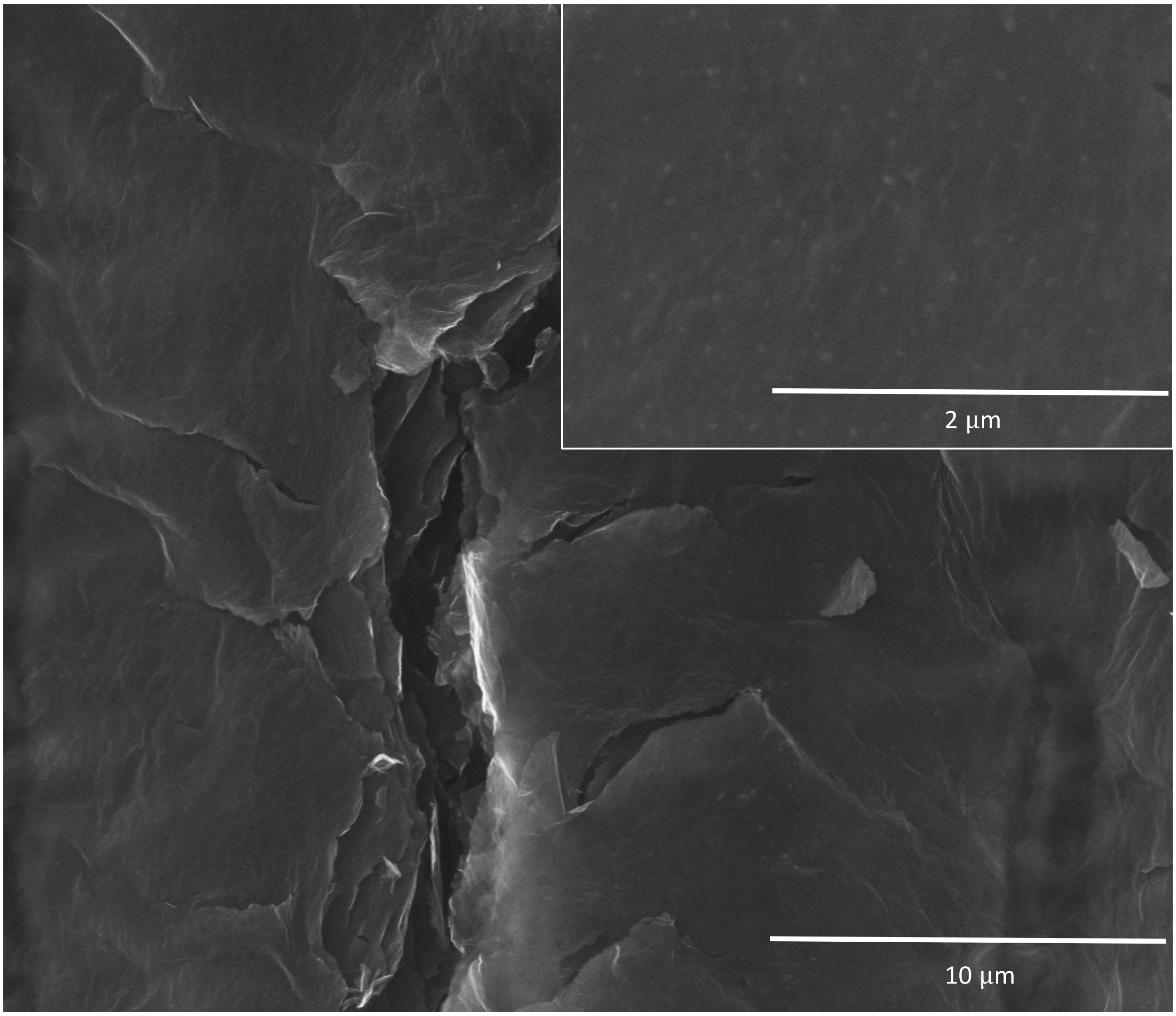

Figure 7.3 A 10,000x magnified scanning electron microscope (SEM) image of a laser scribed graphene (LSG) sample decorated with Pd(0) nanoparticles. The inset shows a 50,000x-magnified view of graphene with homogeneously dispersed nanoparticles.

Analysis of LSG/Ag nanocomposites by TEM reveals the presence of silver nanoparticles throughout the LSG surface (Figure 7.4 - 7.5). Figure 7.6 shows a close-up view of nanoparticles in close proximity to few layer graphene sheets. The lattice fringes are clearly visible in the nanoparticles as well as in the graphene, indicating a high degree of crystallinity. Figure 7.7 shows a 10 nm Ag nanoparticle with lattice spacing of 0.23 nm, which matches the (111) diffraction plane in the fcc lattice of silver. The average Ag(0) nanoparticle size in the LSG/Ag(0) nanocomposite is 5-15 nm. TEM analysis of the LSG/Pd(0) nanocomposite revealed a lower concentration of nanoparticles per area than is observed for Ag(0). This is presumably due to the fact that palladium acetate has very low solubility in water; therefore, some of palladium acetate may have precipitated out during nanocomposite processing. Figure 7.8, inset also shows that the nanoparticles have a narrow size distribution based on evaluation of TEM images, with an average of diameter of 12 nm (Figure 7.8). LSG/NiO nanocomposites also exhibit sparsely populated NiO nanoparticles; however, the cause of this is unknown. Figure 7.9, inset shows a NiO nanoparticle with an interplanar distance of 0.205 nm, corresponding to the (200) reflection in the fcc lattice of a NiO crystal.

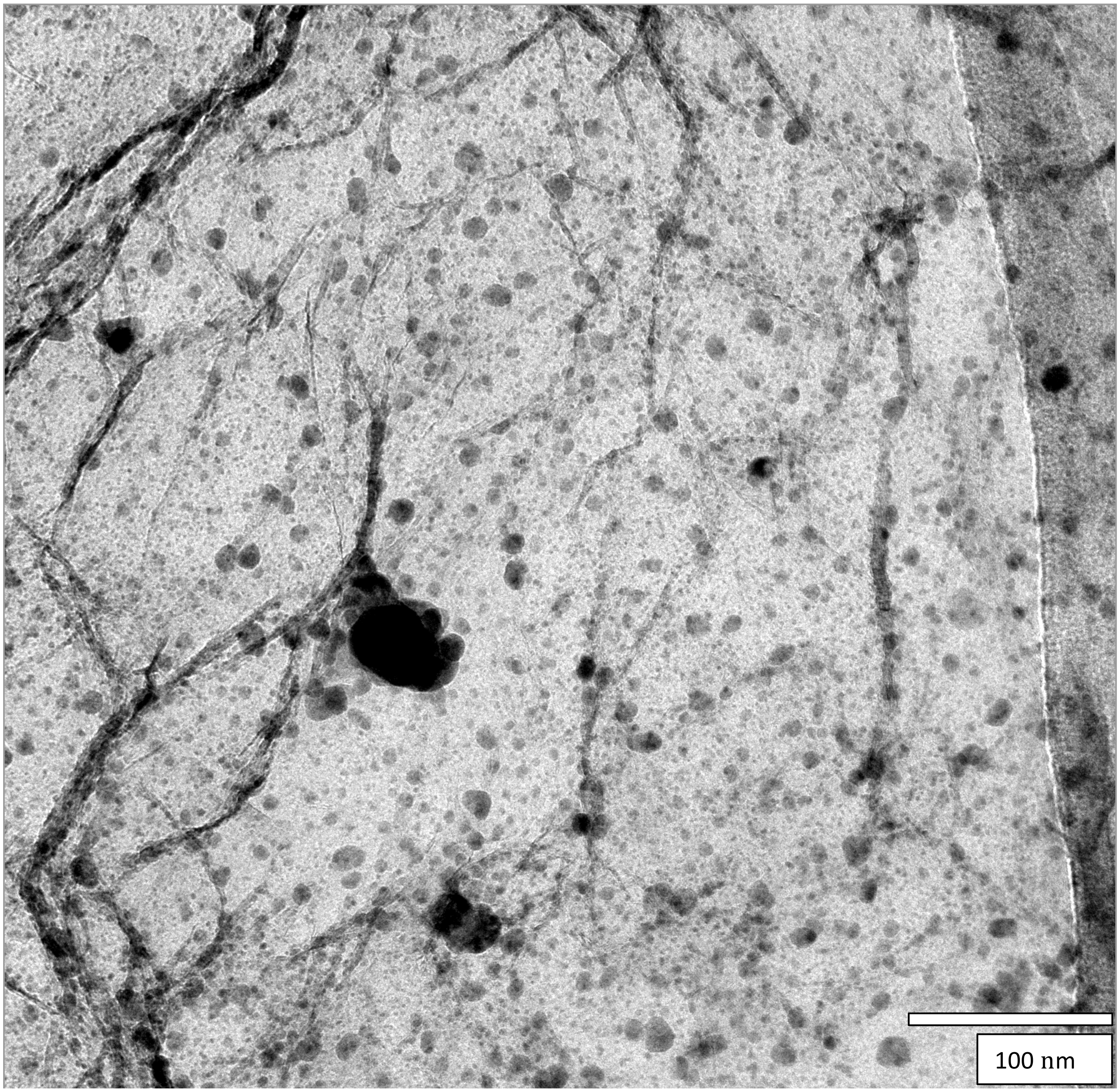

Figure 7.4 A transmission electron microscope (TEM) image of Ag(0) nanoparticles on LSG. The darker spots are agglomerates of smaller nanoparticles as seen in Figure 7.5.

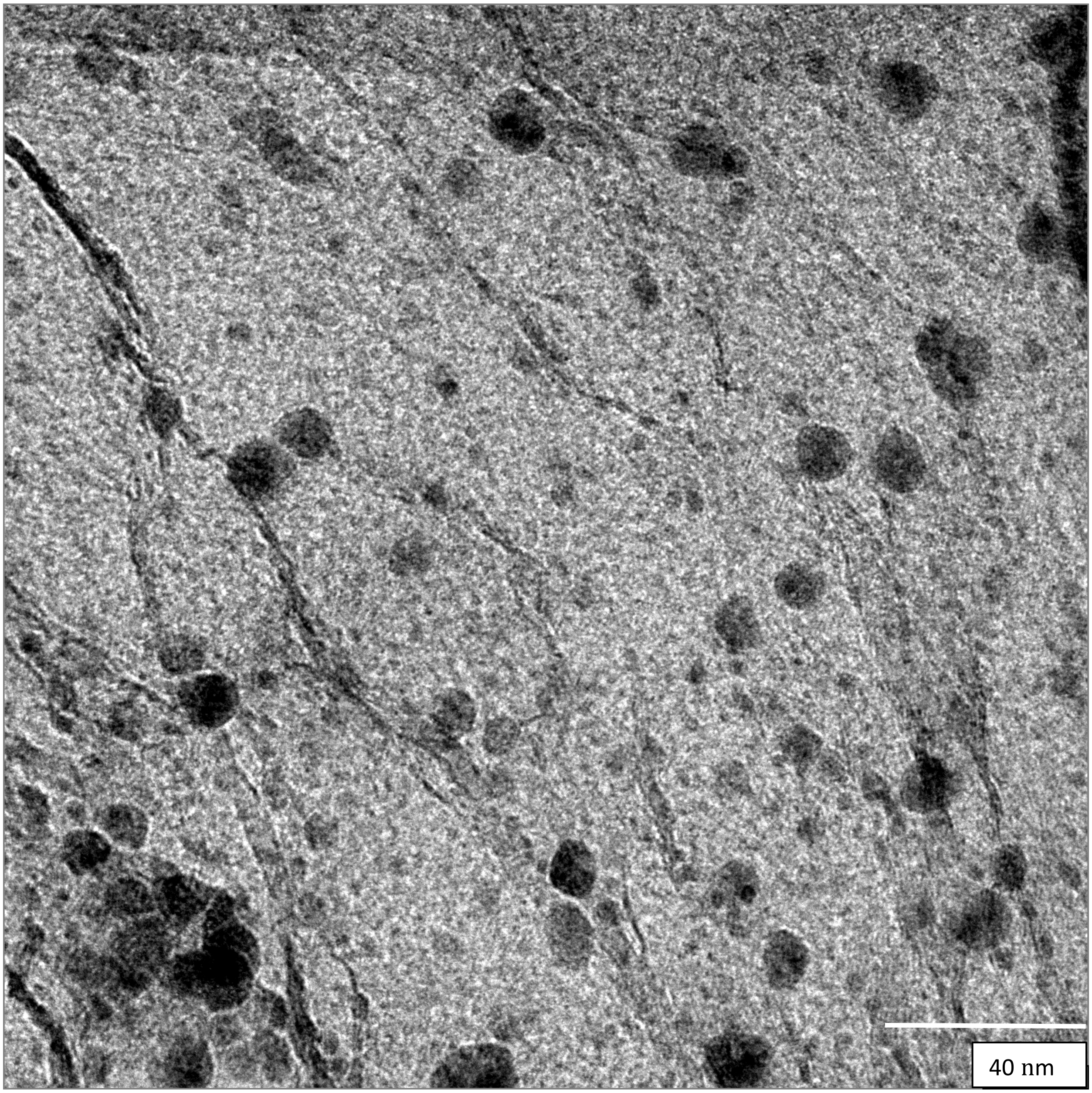

Figure 7.5 A transmission electron microscope (TEM) image of Ag(0) nanoparticles which illustrates a narrow distribution in size of nanoparticles with an average diameter of 10 nm.

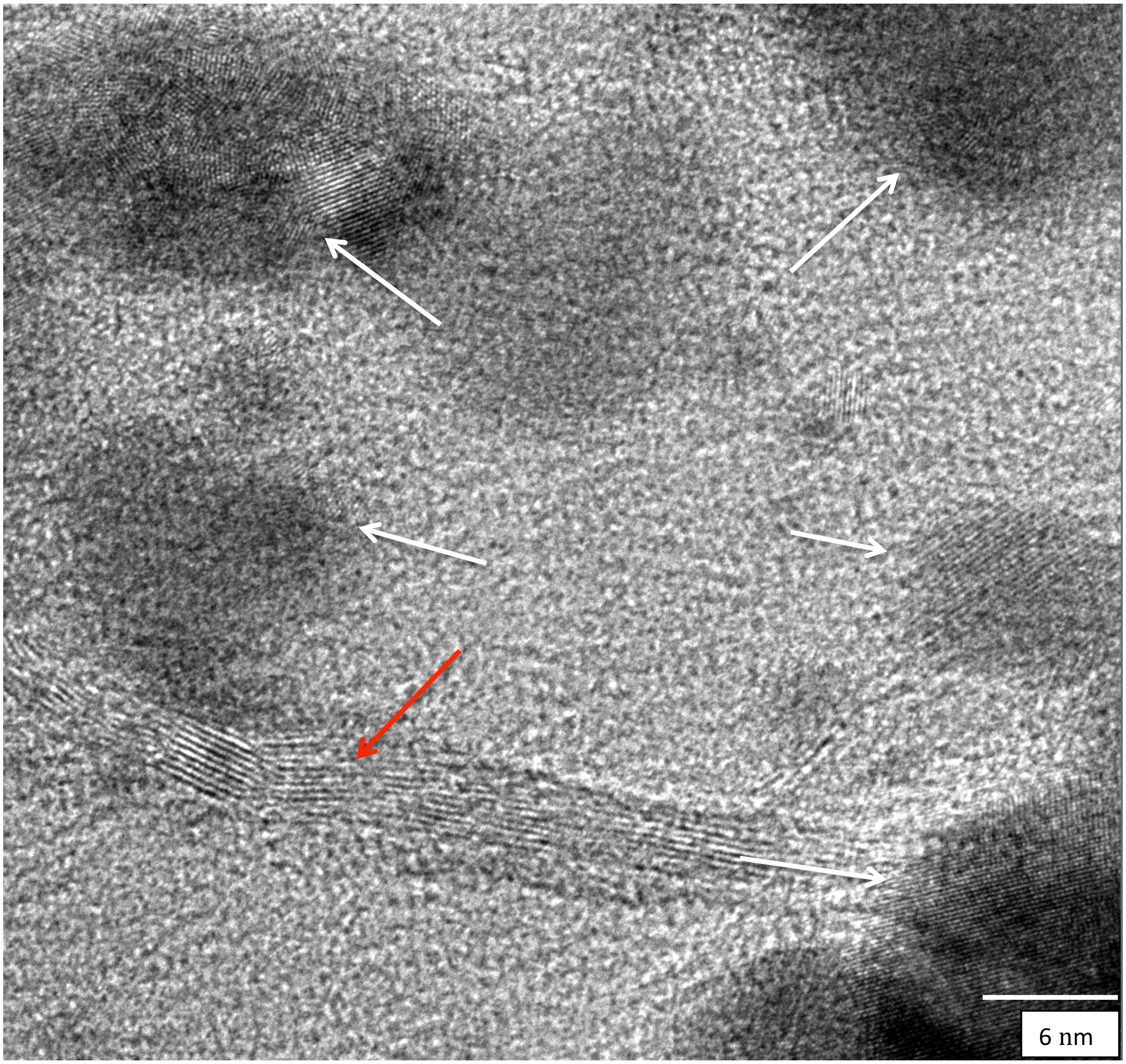

Figure 7.6 A transmission electron microscope (TEM) image of 6-8 nm silver nanoparticles (white arrows) next to few layer graphene sheet (red arrows).

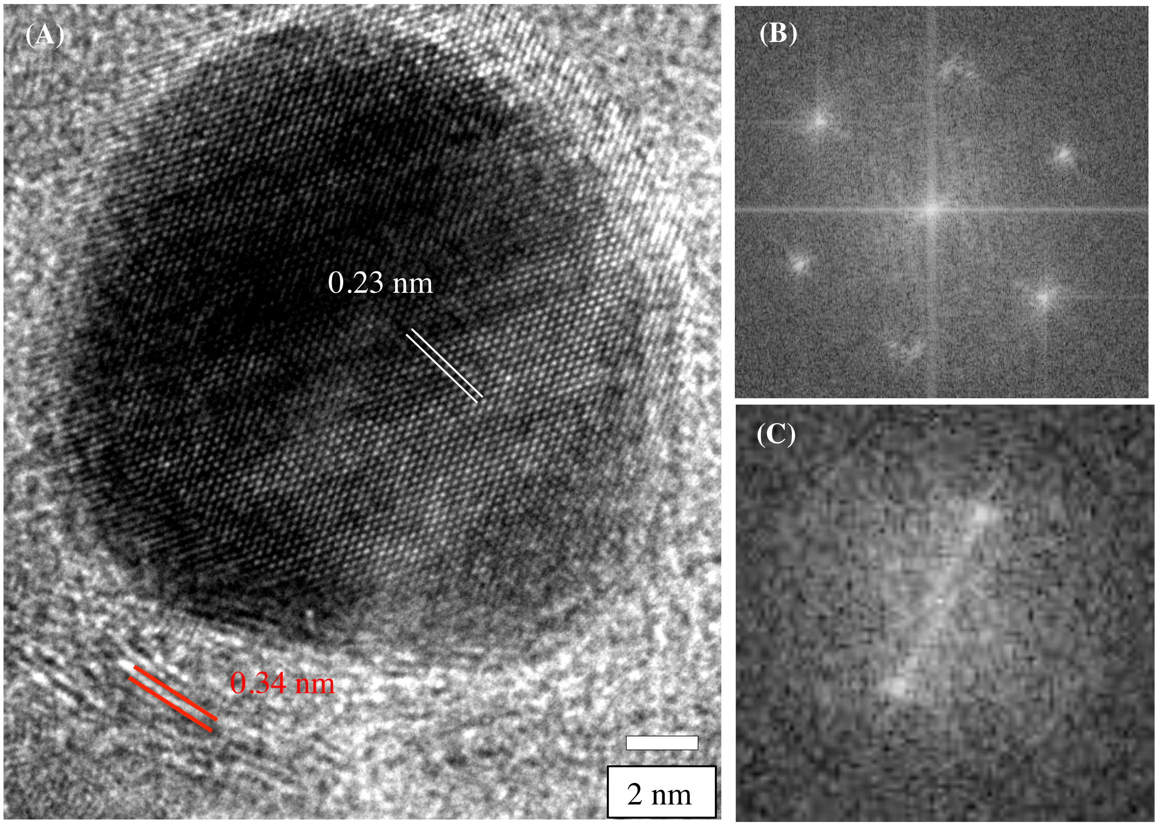

Figure 7.7 A) A TEM image of ~10 nm Ag nanoparticle in proximity to few layer graphene. Ag nanoparticles clearly exhibit lattice fringes with a lattice spacing of 0.23 nm, corresponding to a diffraction plane of (111) in Ag fcc lattice. Few layer graphene shows a 0.34 nm lattice spacing corresponding to the (002) plane in hcp lattice of graphite. B) The corresponding fast Fourier transform (FFT) of a Ag nanoparticle. C) FFT of few layer graphene next to the particle.

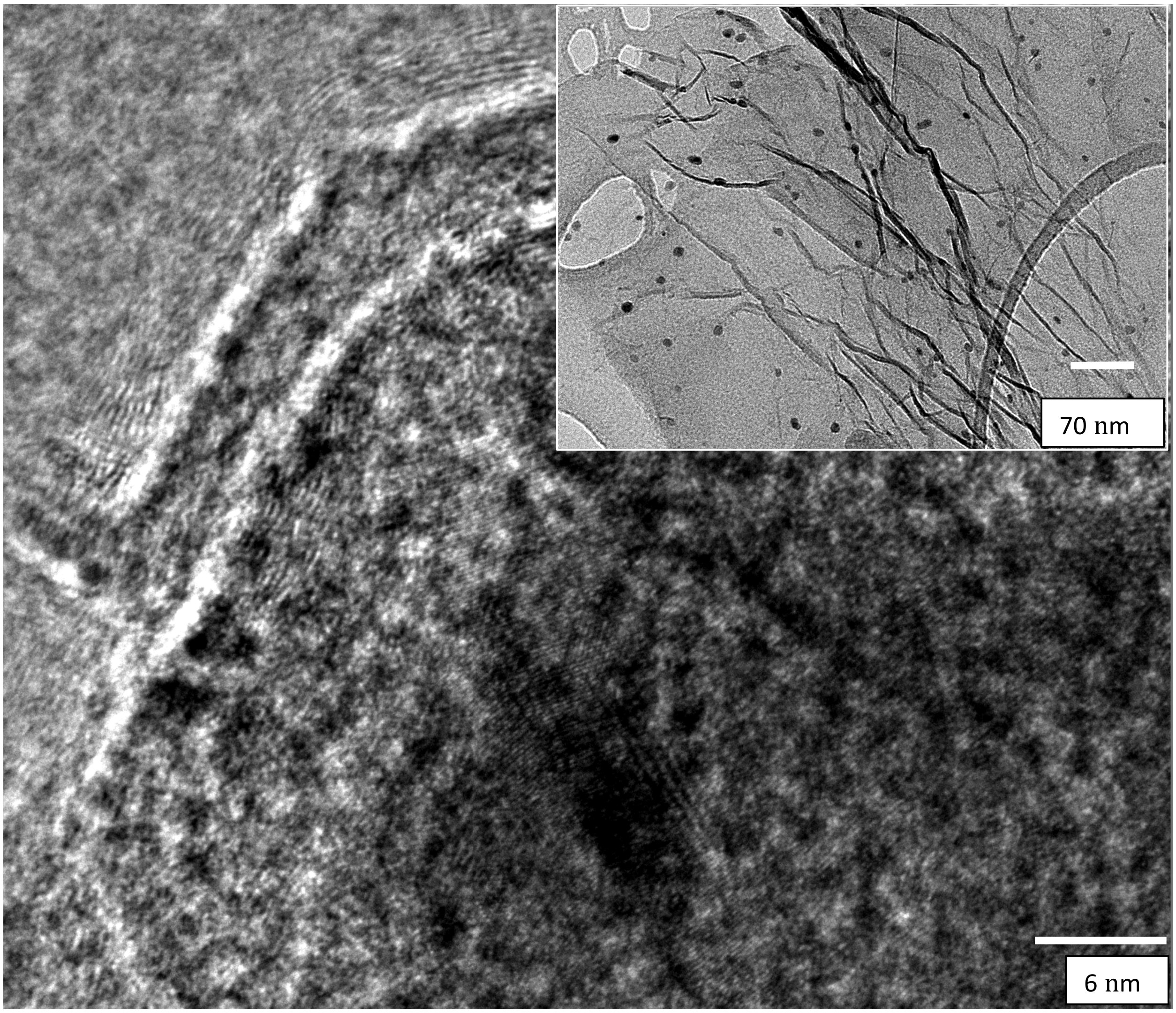

Figure 7.8 A) A TEM image of a Pd(0) nanoparticle (white arrow) on the surface of LSG (red arrow). The inset provides a TEM image of a Pd(0) nanoparticle with an average size distribution of 10 nm on few layer graphene.

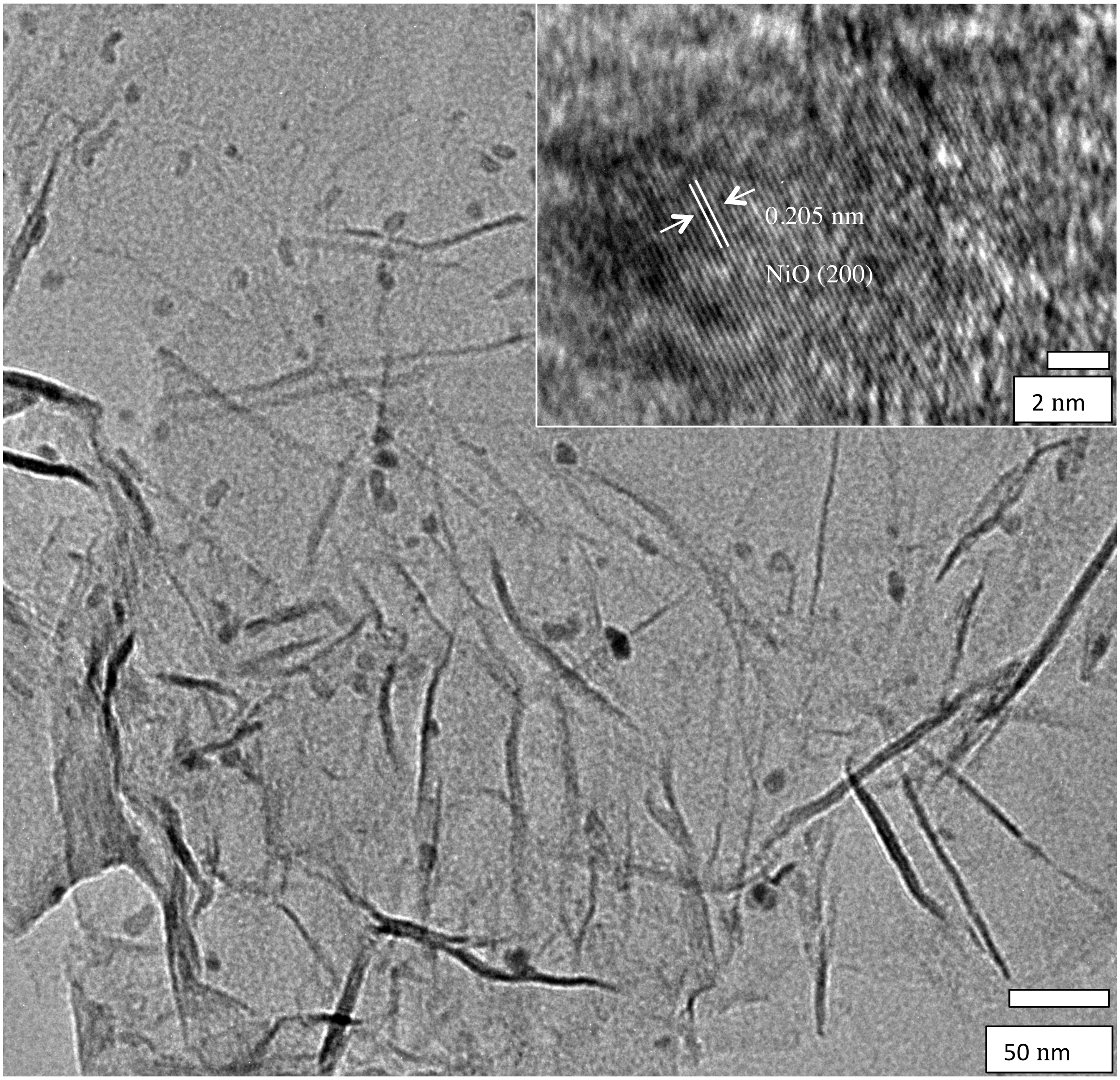

Figure 7.9 TEM image of NiO nanoparticles on LSG. Similarly to Pd(0), the NiO nanoparticles are sparsely populated on LSG, with an average distribution of 10 - 15 nm. The inset shows a single nanoparticle with an interfringe distance of 0.205 nm, corresponding to the (200) lattice planes in a NiO fcc lattice.

7.3.3 Surface analysis using XPS

X-ray photoelectron spectroscopy (XPS) was used to investigate the effects of nanoparticle formation on the quality of the LSG films and the oxidation states of the nanoparticles. Figure 7.10A shows an XPS survey spectrum of an LSG/Ag(0) nanocomposite, with three dominant peaks: C 1s at 284.8 eV, Ag 3d at 375 eV, and O 1s at 534 eV. Comparing the carbon to oxygen (C/O) ratios between graphite oxide (GO) and laser scribed graphene (LSG) provides an effective tool in asserting the degree of reduction that was achieved in the presence of metal acetate salts with a low power infrared laser. We have previously reported that LSG without metal nanoparticles has a C/O ratio of 27.6, with 96.5% C and 3.5% O. Additionally, GO without the metal nanoparticle precursor has a C/O ratio of 1.89, which corresponds to the atomic percent of C and O as 72% and 38%, respectively. Inspecting a C 1s spectrum in Figure 7.10B reveals a C/O oxygen ratio of 20.60, corresponding to 94.56% C and 4.59% O. This is an increase in the overall atomic percent oxygen by 1.09%. The reason for the increase in oxygen content is attributed to the addition of oxygen rich species, such as CO, CO_2, H_2O and CH_3COOH, due to decomposition of the acetate ligand, but further studies are necessary to confirm this hypothesis. Figure 7.10C presents an XPS spectra of the Ag 3d region with a 1.54 atomic percent of Ag. Unfortunately, it is well known that the identification of the valence states of silver from the their binding energy (BE) values is not easy because the states are so closely spaced together. However, the TEM FFT of several areas in the LSG/Ag(0) confirms that the only silver present is in the Ag(0) state.

An XPS survey of an LSG/Pd nanocomposite indicates three distinct peaks, assigned to C 1s, Pd 3d and O 1s. A closer inspection of the C 1s region indicates a higher prevalence of oxygen, 86.85% C and 12.50% O, which converts to 85.19% C and 5.51% O by weight. The remaining 9.30% by weight is assigned to the Pd peak. Compared to LSG/Ag(0), palladium nanocomposite contains 7.91% higher oxygen that is bound to carbon. The reason for the higher oxygen content is unknown and is currently being investigated.

Laser scribing of graphite oxide mixed with nickel acetate tetrahydrate produced LSG with a C/O ratio of 17.27, corresponding to the 93.1% C, and 5.39% O. The carbon to oxygen ratio of the LSG/NiO nanocomposite is slightly below the C/O ratio of 20.60. The reasons for all three metals having different C/O ratios could have to do with the catalytic ability of the metal or the reaction pathway that the nanoparticle precursor undergoes under thermal decomposition. The exact reason is currently being investigated.

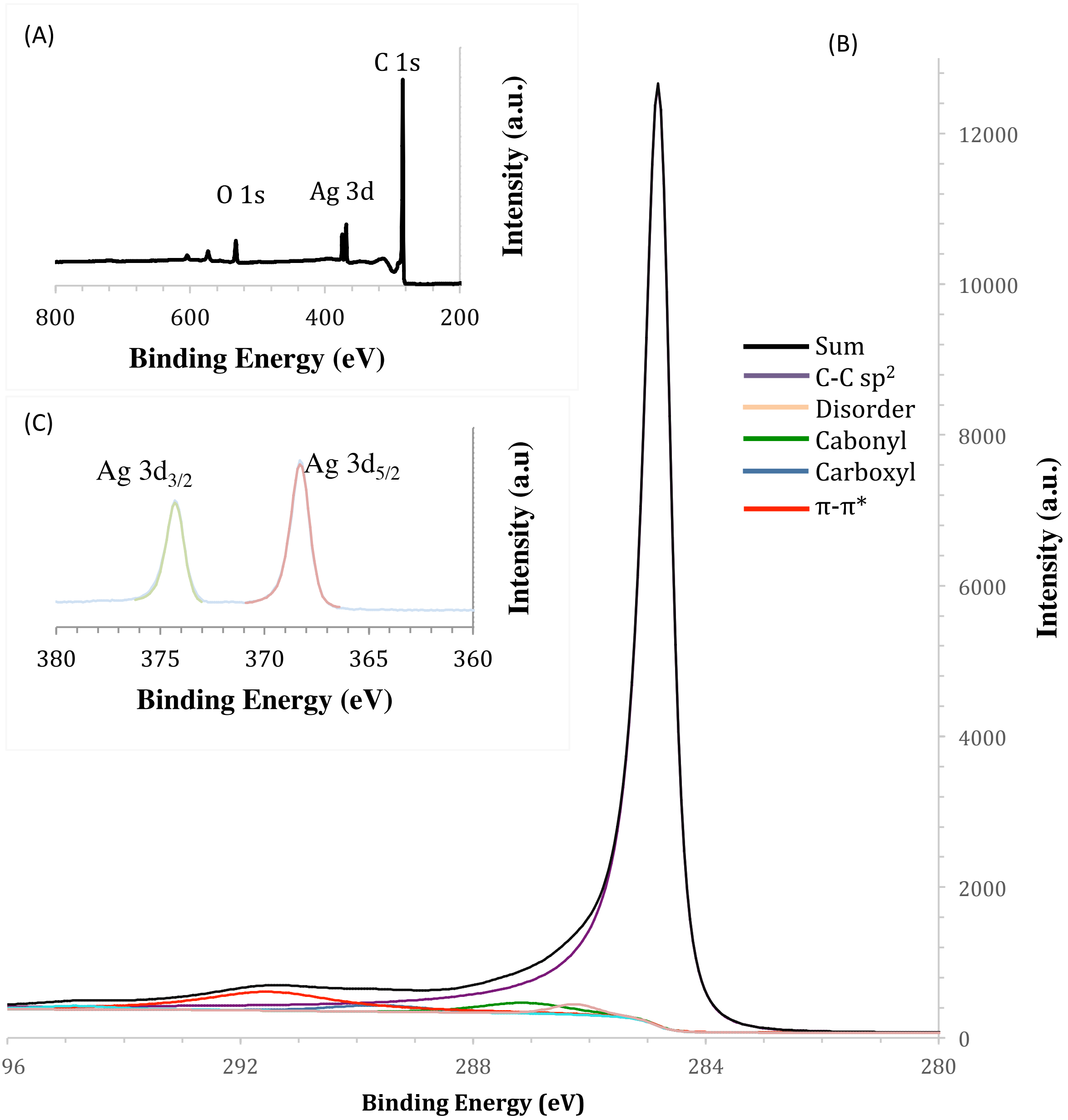

Figure 7.10 A) X-ray photoelectron spectroscopy (XPS) survey spectra of an LSG/Ag nanocomposite. The graph shows the dominant intensity of the C 1s peak followed by the Ag 3d and O 1s peak, which corresponds to 94.26% C, 1.15% Ag and 4.59% O respectively. B) A close up of the C 1s spectra indicating highly reduced graphene. C) A closer view of the Ag 3d XPS region.

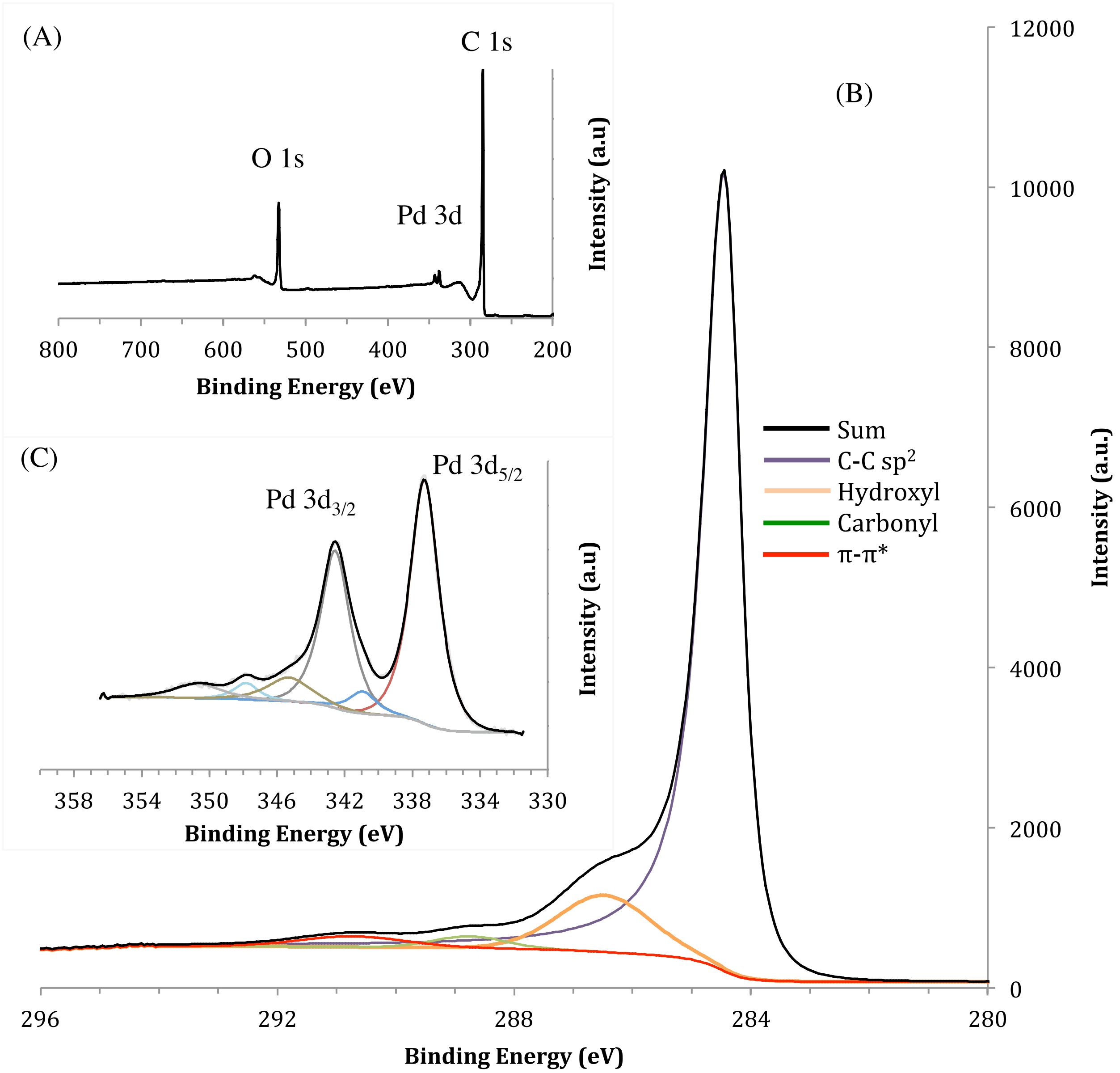

Figure 7.11 A) X-ray photoelectron spectroscopy (XPS) survey spectra of an LSG/Pd nanocomposite. The graph shows the dominant intensity of the C 1s peak followed by the Pd 3d and O 1s peaks, which correspond to 86.85% C, 0.64% Pd and 12.50% O, respectively. B) A close up of the C 1s spectra, which indicates the presence of hydroxyl groups (286.65 eV). C) A closer view of the Pd 3d XPS region, which shows the presence of Pd(0) and some PdO impurity.

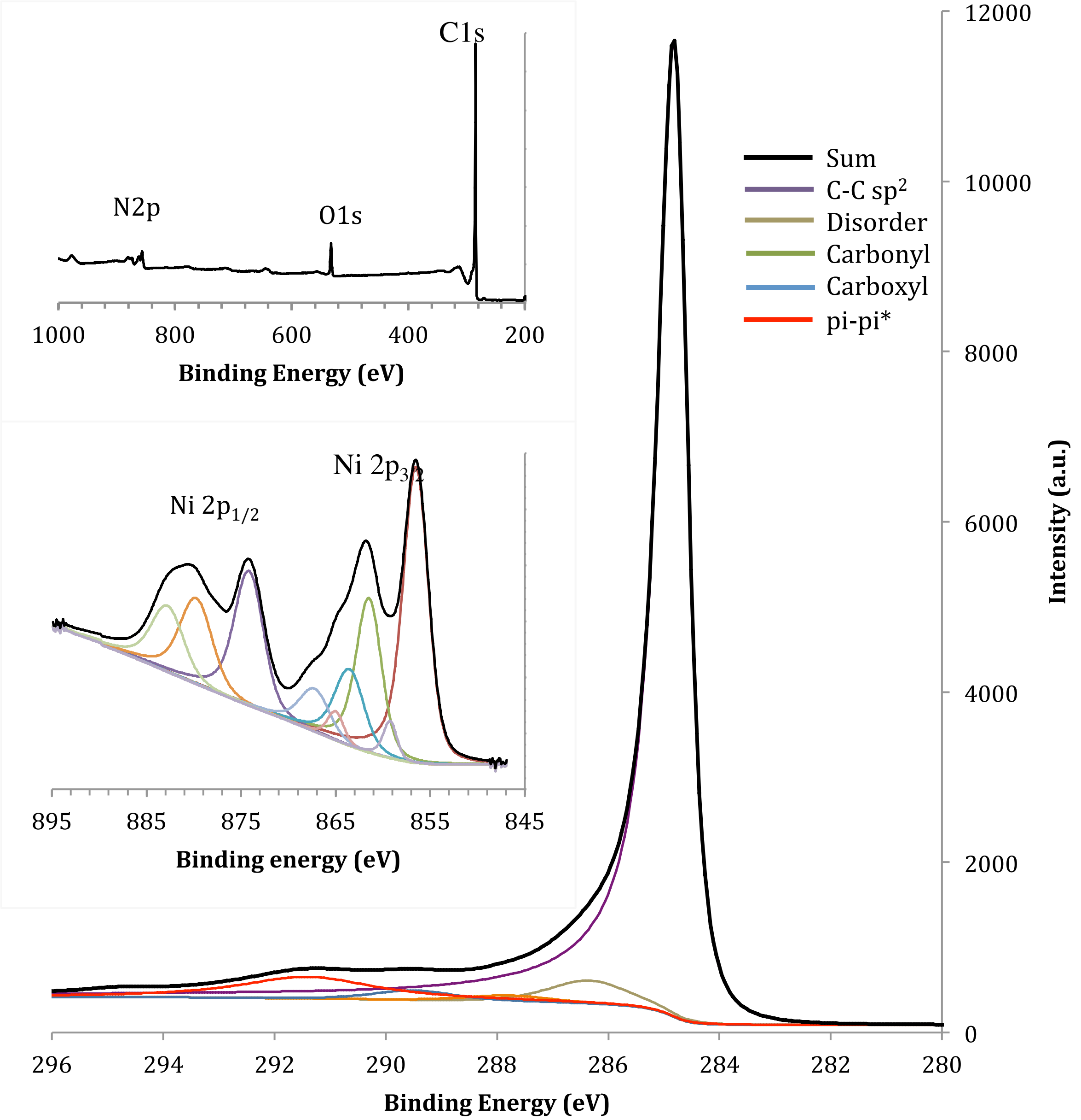

Figure 7.11 A) X-ray photoelectron spectroscopy (XPS) survey spectra of an LSG/NiO nanocomposite. The graph shows that the dominant peak is the C 1s followed by the O 1s and the Ni 2p peak, which corresponds to 93.51%, 5.39% and 1.51%, respectively. B) A close up of the C 1s spectra. C) A closer view of the Ni 2p XPS region, which shows the presence of NiO.

7.4 Applications

7.4.1 LSG/NiO Supercapacitors

One application where LSG/NiO could be utilized immediately is in supercapacitors. As previously shown by El-Kady et al. all-carbon LSG supercapacitors exhibit a gravimetric capacitance of 275 F/g with an H_2SO_4 electrolyte.[21] However, this value can be increased further through the addition of metal oxides that have high pseudocapacitance. This area of research is still ongoing, but preliminary findings indicate an aerial capacitance of 22 mF/cm^2 and a gravimetric capacitance of 35 F/g. Cyclic voltammetry measured at 5 mV/s shows the reduction and oxidation peaks of NiO in Figure 7.12. The reason for the lower capacitance is suspected to be an incompatible electrolyte that doesn't fully wet all the surfaces. Future experiments will be repeated with 1 M H_2SO_4 and other electrolytes, taking into account LSG without NPs as a baseline.

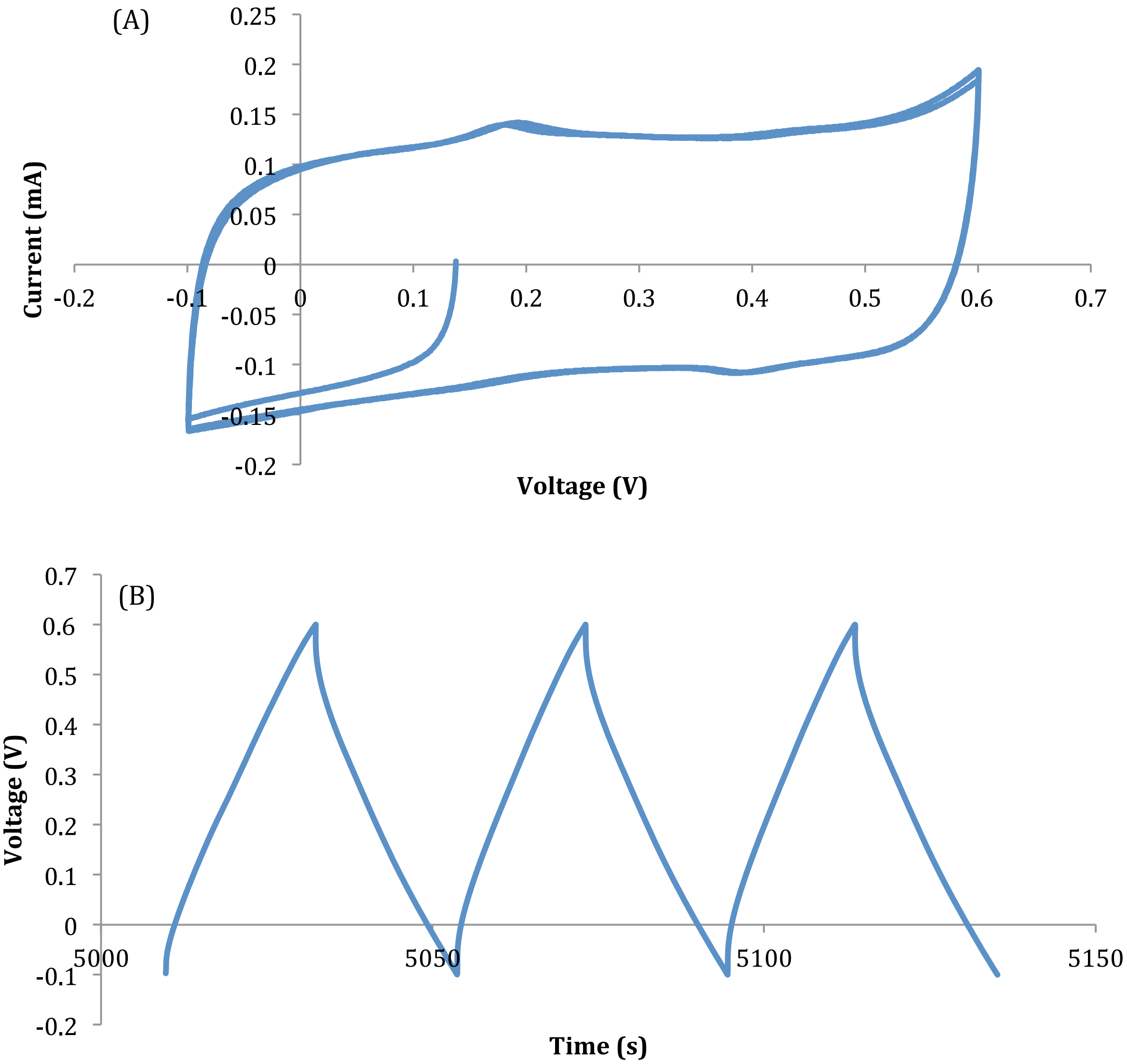

Figure 7.12 Evaluation of the performance of an LSG/NiO electrochemical capacitor in aqueous 6 M KOH solution. (A) Cyclic voltammetry of LSG/NiO at a scan rate of 5 mV/s. A semi-rectangular CV shape is observed for the LSG/NiO-EC, indicating an efficient double-layer formation. (B) Galvanostatic charge/discharge (CC) curves of an LSG/NiO-EC measured at a current density of 5 A/$g_{LSG/electrode}$.

7.4.2 LSG/Pd as a Suzuki-Coupling Catalyst

Another potential application for LSG/Pd(0) is catalysis. More specific, the Suzuki reaction has used palladium nanoparticles for coupling aryl halides with boronic acids[22] (Figure 7.13A). While a few authors have already reported use of Pd(0) for Suzuki coupling on graphene/graphene oxide supports, the surface area of their reported material is well below our LSG material.[23,24] Preliminary experiments have shown that upon reaction of boronic acid with bromobenzene on the surface of an LSG/Pd(0) nanocomposite made from palladium trifluoroacetate ($Pd(TFA)_2$), a 65% isolated yield of product was attained. By comparison when using palladium acetate ($Pd(OAc)_2$), an isolated yield of 45% was achieved. Using inductively coupled plasma optical emission spectroscopy (ICP-OES) we have measured Pd content as 0.7 wt.% in the LSG/Pd nanocomposites prepared from ($Pd(OAc)_2$) and 1.7 wt.% in the LSG/Pd prepared from $Pd(TFA)_2$. Both bromobenzene and biphenyl are soluble in the organic phase. NMR spectra of the bromobenzene precursor (Figure 7.13B) and biphenyl (Figure 7.13C and 7.14) show that the product is pure, with no trace of precursor. Therefore, we have concluded that the conversion is 100%; however, our isolated yield is only 45% for acetate ligands and 65% for trifluoroacetate palladium ligands. In order to investigate the loss of the biphenyl, we have run the reaction with biphenyl alone instead of the precursors and discovered that 10% of the biophenyl binds to the LSG support through $\pi - \pi$ stacking. We expect that recycling the catalyst would allow us to minimize the losses due to biphenyl $\pi - \pi$ stacking.

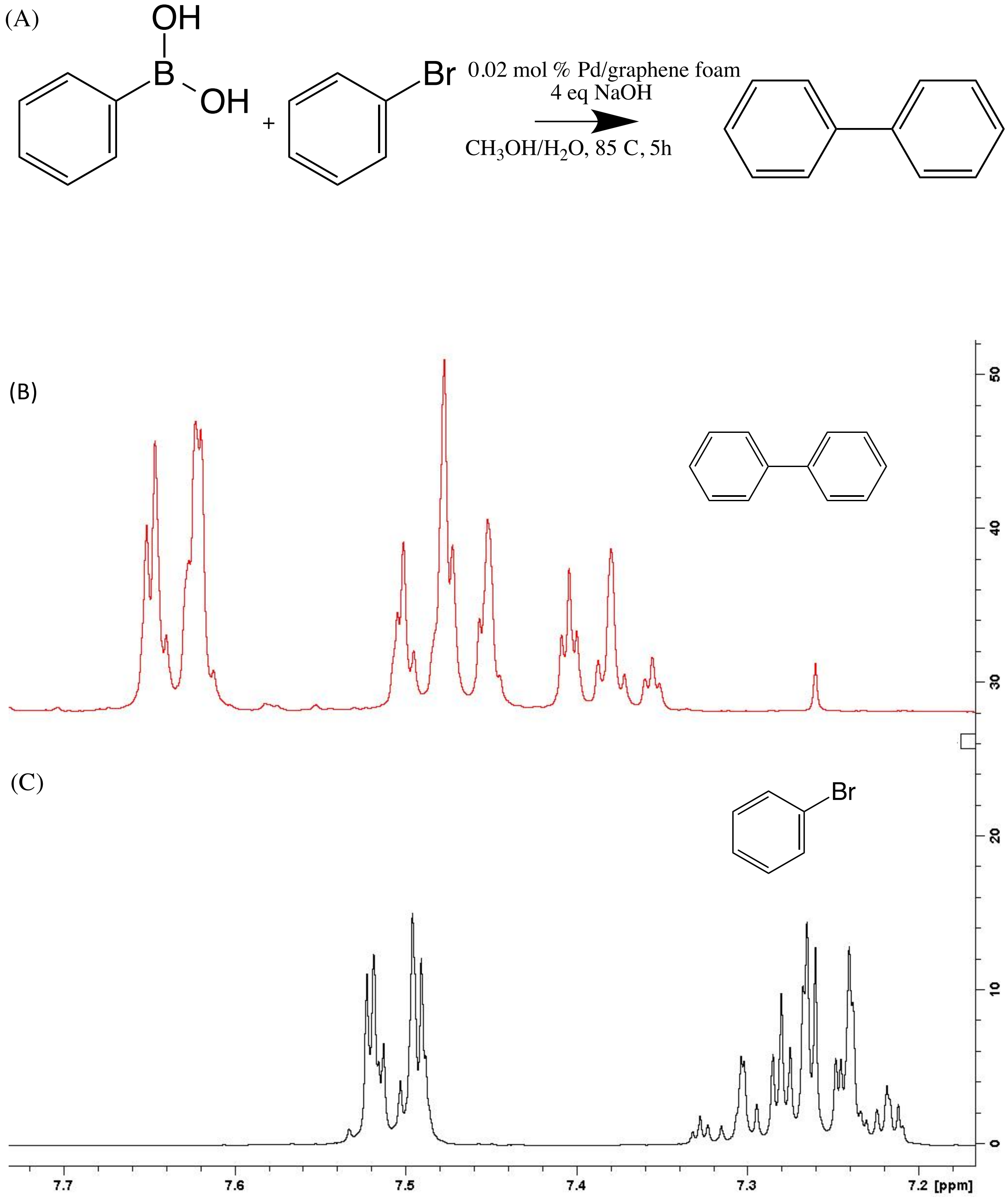

Figure 7.13 A) Reaction scheme for a Suzuki-Miayura coupling reaction. B) ^{1}H NMR spectra of the biphenyl reaction product showing no trace of reaction precursor (C).

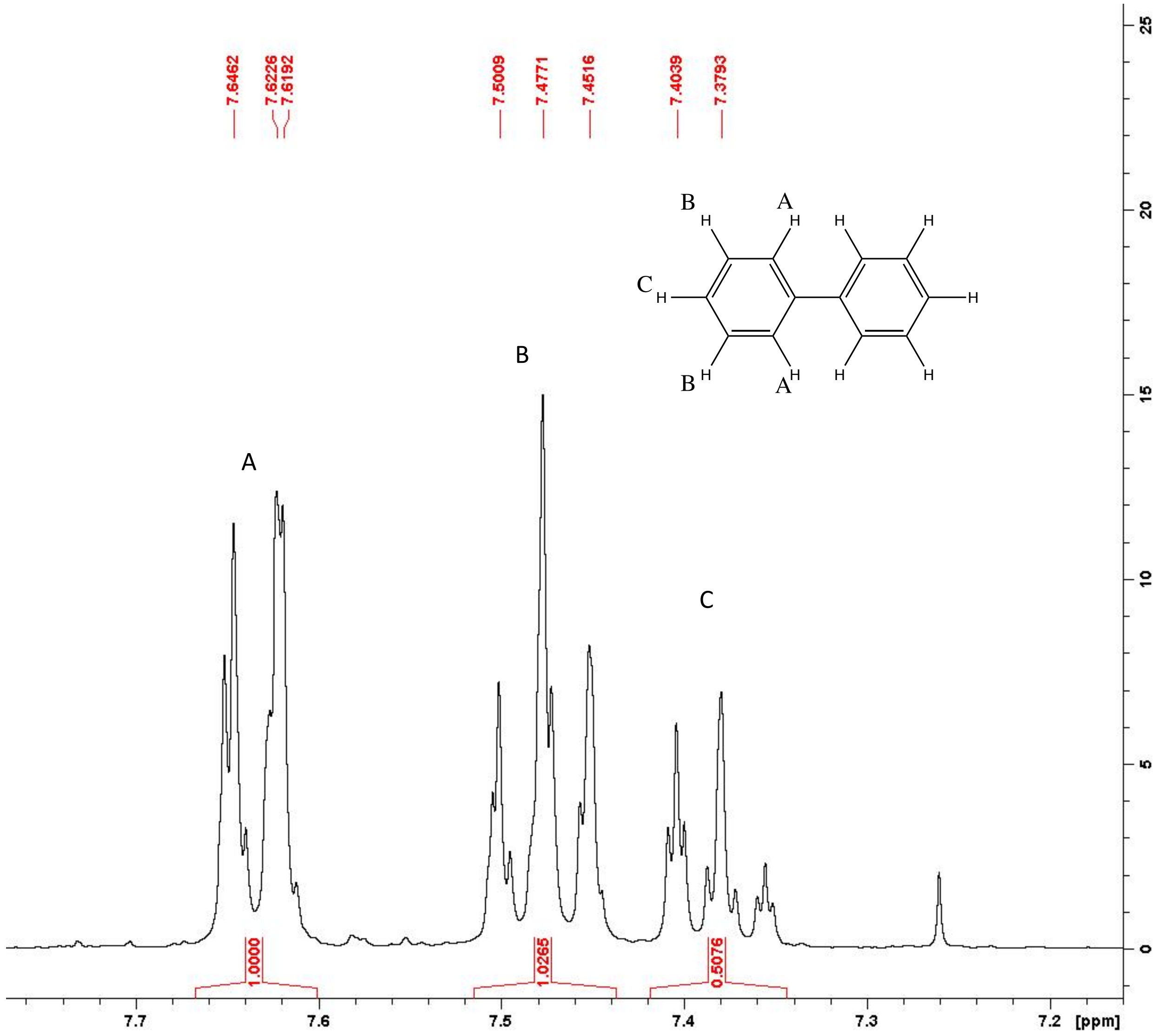

Figure 7.14 A) Integrated ^{1}H NMR spectra of the biphenyl reaction product. The inset shows a labeled biphenyl with labels corresponding to the labeled peaks in a ratio of 2A:2B:C.

7.5 Conclusions

In summary, we have been able to successfully use the process for making laser scribed graphene (LSG) to create LSG/nanoparticle nanocomposites. We have illustrated that nanocomposites can be tailored to the desired application by changing the precursor metal and the ligand. The nanocomposites are made in air using a simple and inexpensive LightScribe drive and now commercially available graphite oxide. Furthermore, we have illustrated that this technology can be both suited for electronic applications such as supercapacitors, as well as for pure chemical synthesis, such as Suzuki-Miyaura coupling reactions.

7.6 References

1. Geim, K.; *Science* **2009**, *324*, 1530 – 1534
2. Bolotin, K. I.; Sikes, K. J.; Jiang, Z.; Klima, M.; Fudenberg, G.; Hone, J.; Kim, P.; Stormer, H. L. *Solid State Comm*. **2008***, 146.9*, 351 – 355.
3. Seol, J. H.; Jo, I.; Moore, A. L.; Lindsay, L.; Aitken, Z. H.; Pettes, M. T.; Li, X.; Yao, Z.; Huang, R.; Broido, D.; Mingo, N.; Ruoff, R. S.; Shi, L. *Science* **2010**, *328*, 213 – 216.
4. Zhu, Y.; Murali, S.; Cai, W.; Li, X.; Suk, J. W.; Potts, J. R.; Ruoff, R. S. *Adv. Mater.* **2010**, *22*, 3906 – 3924
5. Du, X.; Skachko, I.; Barker, A.; Andrei, E. Y. *Nature Nanotech.* **2008**, *3*, 491 – 495
6. Huang, X.; Yin, Z. Y.; Wu, S. X.; Qi, X. Y.; He, Q. Y.; Zhang, Q. C.; Yan, Q. Y.; Boey, F.; Zhang, H. *Small* **2011**, *7*, 1876 – 190
7. Lin, Y. M.; Dimitrakopoulos, C.; Jenkins, K. A.; Farmer, D. B.; Chiu, H. Y.; Grill, A.; Avouris, P. *Science* **2010**, *327*, 662 – 662
8. Liao, L.; Lin, Y. C.; Bao, M.; Cheng, R.; Bai, J.; Liu, Y.; Qu, Y.; Wang, K. L.; Huang, Y.; Duan, X. *Nature* **2010**, *467*, 305 – 308
9. Chang, H. X.; Sun, Z.; Yuan, Q.; Ding, F.; Tao, X.; Yan, F.; Zheng, Z. *Adv. Mater.* **2010**, *22*, 4872 – 4876
10. Wang, X.; Zhi, L.; Müllen, K. *Nano Lett.* **2008**, *8*, 323 – 327
11. Chen, D.; Tang, L.; Li, J. *Chem. Soc. Rev.* **2010**, *39*, 3157 – 3180
12. Zhang, Z.; Xu, F.; Yang, W.; Guo, M.; Wang, X.; Zhang, B.; Tang, J. *Chem. Commun.* **2011**, *47*, 6440 – 6442

13. Li, Y.; Fan, X.; Qi, J.; Ji, J.; Wang, S.; Zhang, G.; Zhang, F. *Nano Research* **2010,** *3*(6), 429 – 437

14. Chen, S.; Zhu, J. W.; Wang, X. *J. Phys. Chem. C* **2010**, 114, 11829 – 11834

15. Xu, C.; Wang, X.; Zhu, J. W. *J. Phys. Chem. C* **2008**, 112, 19841 – 19845

16. Liu, S.; Tian, J. Q.; Wang, L.; Sun, X. P. *Carbon* **2011**, 49, 3158 – 3164

17. Zhang, S.; Shao, Y.; Liao, H.; Liu, J.; Aksay, I. A.; Yin, G.; Lin, Y. *Chem. Mater.* **2011**, *23*, 1079 – 1081

18. Li, H. Q.; Han, L. N.; Cooper-White, J. J.; Kim, I. *Nanoscale* **2012**, *4*, 1355 – 1361

19. Strong, V.; Dubin, S.; El-Kady, M. F.; Lech, A.; Wang, Y.; Weiller, B. H.; Kaner, R. B. *ACS Nano*, **2012**, *6* (2), 1395 – 1403

20. Kim, F.; Luo, J.; Cruz-Silva, R.; Cote, L. J.; Sohnand, K.; Huang, J.; *Adv. Funct. Mater.* **2010**, *20* (17), 2867 – 2873

21. El-Kady, M. F.; Strong, V.; Dubin, S.; Kaner, R. B. *Science*, **2012,** *335* (6074), 1326 – 1330

22. Kim, S. W.; Kim, M.; Lee, W.Y.; Hyeon, T. *J. Am. Chem. Soc.* **2002,** *124* (26), 7642 – 7643

23. Scheuermann, G. M.; Rumi, L.; Steurer, P.; Bannwarth, W.; Mülhaupt, R. *J. Am. Chem. Soc.* **2009,** *131* (23), 8262 – 8270

24. Siamaki, A. R.; Khder. A. E. S.; Abdelsayed, V.; El-Shall, M. S.; Gupton, B. F. *J. Catal.* **2011**, *279* (1), 1 – 11